

Single-source-precursor derived additive-free bulk SiHf(B)N ceramics with excellent mechanical properties and oxidation resistance

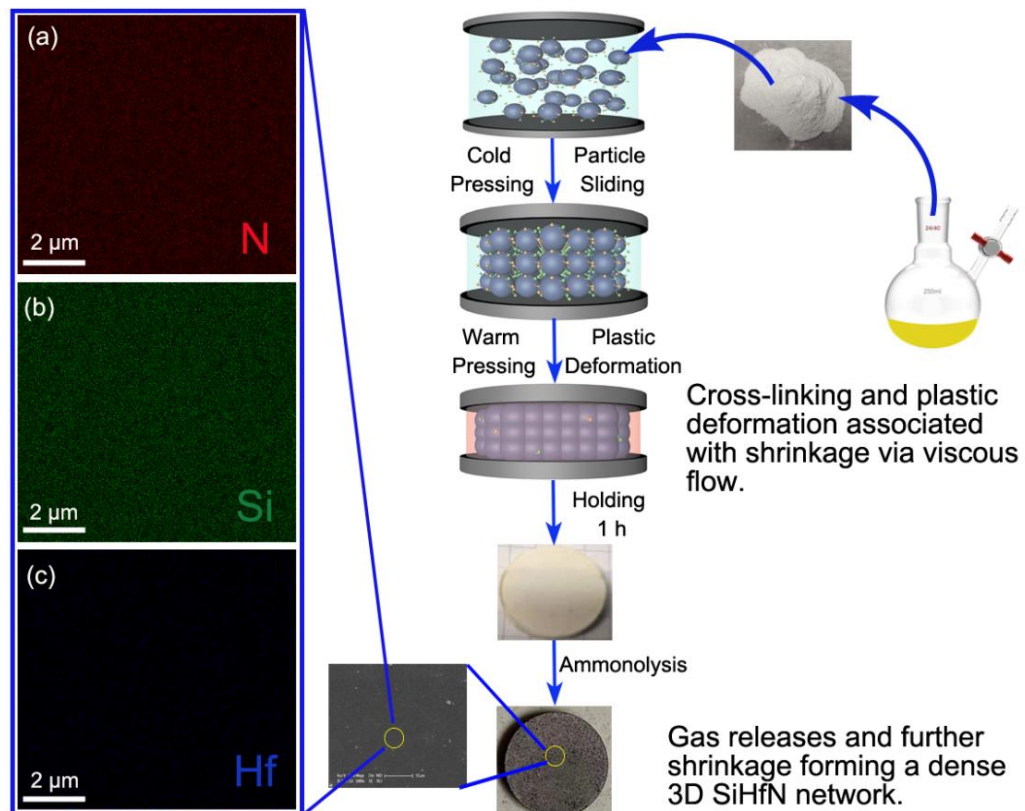
M. Eng. Wei Li

Prof. Dr. Ralf Riedel (Supervisor)

Dispersive Solids, Department of Materials and Earth Sciences



TECHNISCHE
UNIVERSITÄT
DARMSTADT



**A Cumulative Dissertation approved by the Department of Materials and Earth Sciences
in Fulfillment of the Requirements for the Degree of Rerum Naturalium (Dr. rer. nat.)**

**Single-source-precursor derived additive-free bulk
SiHf(B)N ceramic with excellent mechanical
properties and oxidation resistance**

M. Eng. Wei Li

From Anyang, Henan, China, Matrikel-Nr.: 2734138



TECHNISCHE
UNIVERSITÄT
DARMSTADT

Referee: Prof. Dr. Ralf Riedel

Co-referee: Prof. Dr. Anke Weidenkaff

Fachbereich Material- und Geowissenschaften

Technische Universität Darmstadt

Date of submission: 21.12.2022

Date of oral examination: 21.02.2023

Darmstadt 2023

Single-source-precursor derived additive-free bulk SiHf(B)N ceramic with excellent mechanical properties and oxidation resistance

Additivfreie Bulk-SiHf(B)N-Keramiken mit hervorragenden mechanischen Eigenschaften und Oxidationsbeständigkeit hergestellt aus Einkomponentenvorstufen

Genehmigte kumulative Dissertation von M. Eng. Wei Li aus Henan, China

Fachbereich Material- und Geowissenschaften

Darmstadt, Technische Universität Darmstadt

Jahr der Veröffentlichung der Dissertation auf TUpriints: 2023

URN: urn:nbn:de:tuda-tuprints-233027

Tag der Einreichung: 21.12.2022

Tag der mündlichen Prüfung: 21.02.2023

Veröffentlicht unter CC BY-NC 4.0 International

<https://creativecommons.org/licenses/>

Declaration

M. Eng. Wei Li

Otto-Berndt-Straße 3

64287 Darmstadt

Declaration

The main work of this thesis was carried out at the Department of Materials- and Earth Sciences, Technical University of Darmstadt during the period October 2019 to November 2022. This thesis represents the author's original work, except where otherwise stated, and no part of it has been submitted for a degree at any other university. Prior to the submission of this thesis, some work has been published as described in the relevant chapters herein.

Eidesstattliche Erklärung

Hiermit erkläre ich an Eides statt, dass ich die vorliegende Dissertation selbstständig und nur mit den angegebenen Hilfsmitteln angefertigt habe. Von mir wurde weder an der Technischen Universität Darmstadt noch einer anderen Hochschule ein Promotionsversuch unternommen.

Darmstadt, den 21.12.2022

M. Eng. Wei Li

Erklärungen laut Promotionsordnung

§8 Abs. 1 lit. c PromO

Ich versichere hiermit, dass die elektronische Version meiner Dissertation mit der schriftlichen Version übereinstimmt.

§8 Abs. 1 lit. d PromO

Ich versichere hiermit, dass zu einem vorherigen Zeitpunkt noch keine Promotion versucht wurde. In diesem Fall sind nähere Angaben über Zeitpunkt, Hochschule, Dissertationsthema und Ergebnis dieses Versuchs mitzuteilen.

§9 Abs. 1 PromO

Ich versichere hiermit, dass die vorliegende Dissertation selbstständig und nur unter Verwendung der angegebenen Quellen verfasst wurde.

§9 Abs. 2 PromO

Die Arbeit hat bisher noch nicht zu Prüfungszwecken gedient.

Darmstadt, den 21.12.2022

(Wei Li)

The presented cumulative dissertation summarizes the essential scientific findings, which were reported to the scientific community in the following peer-reviewed journals. Copies of the published studies below are enclosed in the Chapter Cumulative Publications of this thesis.

1. **Li W**, Li F, Yu Z, et al. Polymer-derived SiHfN ceramics: from amorphous bulk ceramics with excellent mechanical properties to high temperature resistant ceramic nanocomposites [J]. *Journal of the European Ceramic Society*, 2022, 42(11): 4493-4502.
2. **Li W**, Yu Z, Wiehl L, et al. Hard and Tough Novel High-Pressure γ -Si₃N₄/Hf₃N₄ Ceramic Nanocomposites [J]. *Journal of Advanced Ceramics*, Available online: 08 May 2023.
3. **Li W**, Du H, Tian C, et al. Single-source-precursor derived bulk Si₃N₄/HfB_xN_{1-x} ceramic nanocomposites with excellent oxidation resistance [J]. *Zeitschrift für anorganische und allgemeine Chemie.*, 2022.
4. Zhan Y, **Li W**, Jiang T, et al. Boron-modified perhydropolysilazane towards facile synthesis of amorphous SiBN ceramic with excellent thermal stability [J]. *Journal of Advanced Ceramics*, 2022: 11(7): 1104-1116.

Contents

List of figures	I
List of tables.....	VII
List of abbreviations.....	IX
Abstract.....	XI
Zusammenfassung.....	XIII
1. Introduction and motivation	- 1 -
2 Literature review.....	- 5 -
2.1 Polymer-derived ceramics (PDCs).....	- 5 -
2.1.1 PDC route: principle, history and recent developments.....	- 5 -
2.1.2 Synthesis of preceramic precursors.....	- 7 -
2.1.3 Processing and thermal conversion of PDCs	- 10 -
2.1.4 Polymer derived ceramic nanocomposites (PDC-NCs).....	- 14 -
2.1.5 Advantages and disadvantages of PDCs	- 15 -
2.2 Silicon nitride.....	- 16 -
2.2.1 Crystal structure of silicon nitride.....	- 16 -
2.2.1.1 α -Si ₃ N ₄ and β -Si ₃ N ₄	- 17 -
2.2.1.2 γ -Si ₃ N ₄	- 18 -
2.2.2 Fabrication and mechanical properties of Si ₃ N ₄	- 19 -
2.2.2.1 Sintering and densification of α - and β -Si ₃ N ₄	- 20 -
2.2.2.2 Synthesis of γ -Si ₃ N ₄	- 23 -
2.2.2.3 Mechanical properties of Si ₃ N ₄	- 23 -
2.2.3 Si ₃ N ₄ ceramics with reinforcement phase	- 25 -
2.2.4 Polymer-derived Si ₃ N ₄ -based ceramic nanocomposites	- 27 -
2.3 Scope of the work	- 30 -
3 Cumulative part of the thesis	- 31 -
3.1 Polymer-derived SiHfN ceramics: from amorphous bulk ceramics to high temperature resistant ceramic nanocomposites.....	- 32 -
3.1.1 Experimental procedures.....	- 32 -
3.1.1.1 Synthesis and ammonolysis of the SiHfN precursors	- 32 -
3.1.1.2 Characterization	- 33 -
3.1.1.3 Mechanical properties	- 33 -
3.1.2 Results and discussion	- 34 -
3.1.2.1 Fabrication of bulk SiHfN ceramic	- 34 -
3.1.2.2 Crystallization and thermal behavior	- 40 -
3.1.2.3 Mechanical properties	- 46 -
3.1.3 Conclusion	- 48 -
3.2 Hard and Tough Novel High-Pressure γ-Si₃N₄/Hf₃N₄ Ceramic Nanocomposites	- 50 -

3.2.1 Experimental methods.....	- 50 -
3.2.1.1 Single-source-precursor synthesis and ammonolysis.....	- 50 -
3.2.2 Results and discussion.....	- 52 -
3.2.2.1 Single-source precursor synthesis and pyrolysis.....	- 52 -
3.2.2.2 Structural evolution of the SiHfN ceramic at HP-HT	- 54 -
3.2.2.3 Characterization of the γ -Si ₃ N ₄ /Hf ₃ N ₄ composite	- 57 -
3.2.2.4 Mechanical properties	- 60 -
3.2.3 Conclusions	- 63 -
3.3 Single-source-precursor derived bulk Si₃N₄/HfB_xN_{1-x} ultra-high temperature ceramic nanocomposites.....	- 64 -
3.3.1 Experimental procedures.....	- 64 -
3.3.1.1 Synthesis and pyrolysis of the single-source precursors	- 64 -
3.3.1.2 Characterization	- 65 -
3.3.1.3 Oxidation tests.....	- 66 -
3.3.2 Results and Discussion.....	- 66 -
3.3.2.1 Synthesis of the single-source precursors	- 66 -
3.3.2.2 Polymer-to-ceramic conversion	- 70 -
3.3.2.3 Microstructural characterization	- 72 -
3.3.2.4 Oxidation resistance	- 76 -
3.3.3 Conclusion.....	- 79 -
4 Conclusions and outlook	- 81 -
4.1 Conclusions	- 81 -
4.2 Outlook.....	- 82 -
5 Reference	- 85 -
Acknowledgements.....	- 105 -
Curriculum vitae	- 107 -
Publications and patents (2016 ~ 2022)	- 109 -
Statement of Personal Contribution	- 111 -

List of figures

Figure 2. 1 Schematic diagram of general molecular structure of preceramic organosilicon compounds [28].	- 6 -
Figure 2. 2 Time line of the evolution of research in the PDC field from 1956 to present [54].	- 7 -
Figure 2. 3 General synthesis routes of various organosilicon polymers [28, 55].	- 8 -
Figure 2. 4 Chemical modification of PHPS with (a) titanium n-butoxide [65], (b) aluminum hydride (trimethylamine-alane) [70], (c) and (d) tetrakis(dimethylamido) hafnium(IV) [19], respectively.	- 10 -
Figure 2. 5 Schematic of the polymer-to-ceramic transformation and shaping process of polymer-derived ceramics [28].	- 13 -
Figure 2. 6 Crystal structures of (a) α - Si_3N_4 , (b) β - Si_3N_4 and (c) γ - Si_3N_4 and viewing (d) α - Si_3N_4 , (e) β - Si_3N_4 from (1120) direction. Blue and green spheres are Si and N atoms, respectively. In the unit cell of α - Si_3N_4 and β - Si_3N_4 , trigonal coordination of N-Si ₃ parallel to the basal plane is exhibited by red triangles. In the unit cell of γ - Si_3N_4 , tetrahedral coordination of Si atoms is shown by purple. Tetrahedral and octahedral coordination are shown by purple and blue polyhedra, respectively. Dashed lines in (d) and (e) represent stacking layers repetition in the direction of c axis [163].	- 18 -
Figure 2. 7 Schematic diagram of the densification mechanism of Si_3N_4 ceramics using Al_2O_3 and Y_2O_3 as sintering additives.	- 22 -
Figure 2. 9 Basic synthesis pathways of polysilazanes via ammonolysis and aminolysis.	- 27 -
Figure 2. 10 Schematic diagram for the preparation of TiN/ Si_3N_4 nanocomposite powder and bulk samples from polytitanosilazanes [232].	- 29 -
Figure 3. 1 TG (black lines), DTA (blue lines), and temperature (red lines) curves of (a) original PHPS and (b) SiHfN precursor under flowing ammonia/argon atmosphere (90 vol.% NH_3).	- 36 -
Figure 3. 2 Optical images of SiHfN green bodies prepared at 100 MPa, 110 °C, and 200 °C.	- 36 -
Figure 3. 3 Open porosity and skeletal density of SiHfN ceramics annealed at 1300 °C as a function of	

pressure applied during warm-pressing.....	- 37 -
Figure 3. 4 SEM micrographs taken with 15 kV accelerating voltage of SiHfN samples produced at 1300 °C warm-pressing at 110 °C and under different pressure loads as follows: (a, b) 80 MPa, (c, d) 100 MPa, (e, f) 120 MPa, (g, h) 160 MPa, (i, j) 180 MPa, and (k, l) 200 MPa.....	- 38 -
Figure 3. 5 (A) Elemental mappings of the SiHfN ceramic prepared via warm-pressing of the precursor at 120 MPa and subsequent annealing at 1300 °C. (B) Schematic diagram of the preparation principle of high-density SiHfN ceramic: The first step corresponds to the cold pressing of the polymer. The second step is the controlled warm-pressing of the SiHfN precursors into a green body, and the final step corresponds to the pressureless ammonolysis of a representative disk-shaped SiHfN specimen. (C) Basic suggested principles involved in the warm-pressing procedure from polymeric precursor to dense SiHfN ceramic [87].....	- 39 -
Figure 3. 6 Optical images of SiHfN ceramic specimens: (a) SiHfN-13, (b) SiHfN-15, and (c) SiHfN-17.....	- 40 -
Figure 3. 7 (a) XRD patterns of the SiHfN ceramics annealed at 1000 °C, 1300 °C, 1500 °C, and 1700 °C; Rietveld refinements of the XRD patterns of (b) SiHfN ceramic and (c) PHPS-derived Si ₃ N ₄ annealed at 1700 °C.....	- 41 -
Figure 3. 8 Weight loss of the SiHfN-13, SiHfN-15, and SiHfN-17 ceramic samples after annealing at different temperatures in 0.1 MPa N ₂	- 42 -
Figure 3. 9 TEM images of SiHfN annealed at 1000 °C (a and b) and at 1300 °C (c and d); (b) and (d) are high resolution micrographs magnified from (a) and (c), respectively; the inset in (a) and (b) is the SAED images; the inset in (d) is the FFT image from the selected area.....	- 43 -
Figure 3. 10 TEM micrographs of SiHfN-15 (a and b), b) is a high-resolution image enlarged from a) and SiHfN-17 (c and d), d) is a high-resolution image magnified from c); the inset in (a) and (b) is a SAED image; the insets in (b) and (d) are FFT images from the selected areas.	- 45 -
Figure 3. 11 Evolution of the nano hardness and Young's modulus obtained from 9 nanoindentation tests on SiHfN samples produced at 1300 °C after warm pressing at different loads.	- 47 -

Figure 3. 12 Effect of the pressure applied during warm-pressing on the Vickers hardness of SiHfN ceramics.....	- 48 -
Figure 3. 13 Comparison of the Vickers hardness and nano hardness of the amorphous SiHfN-13 ceramic prepared by warm-pressing at 120 MPa and reported silicon-based bulk ceramics.	- 48 -
Figure 3. 14 FTIR spectra of TDMAH, dried PHPS, SiHfN precursor, and SiHfN ceramic obtained after pyrolysis of the precursor at 1000 °C in ammonia.....	- 53 -
Figure 3. 15 (a) TG (black line) and DTA (blue line) curves of SiHfN precursor under flowing ammonia/argon atmosphere (90 vol.% NH ₃). (b) XRD patterns of the SiHfN sample pyrolyzed at 1000 °C under ammonia atmosphere.	- 54 -
Figure 3. 16 Sequence of ED-XRD patterns, showing the phase transformation of the SiHfN ceramic at 19.5 (±0.5) GPa: (a) on heating in the temperature range of 990 °C – 1920 (± 20) °C; (b) on holding the maximum temperature of 1920 °C during a time range between 200 and 1900 s.	- 55 -
Figure 3. 17 Rietveld refinement of the AD-XRD powder pattern of SiHfN sample recovered from the HP-HT experiment after completing the ED-XRD measurements (The final residual is wR = 7.3 %)...	- 56 -
Figure 3. 18 Thermodynamic guideline for the synthesis of high-pressure nitride nanocomposites in the ternary SiHfN system.....	- 57 -
Figure 3. 19 Rietveld refinement of the γ -Si ₃ N ₄ /Hf ₃ N ₄ composite, recovered from a HP-HT experiment at ~20 GPa and ~1500 °C.....	- 58 -
Figure 3. 20 TEM images of the γ -Si ₃ N ₄ /Hf ₃ N ₄ nanocomposite synthesized at ~20 GPa and ~1500 °C. (a) TEM image of a typical microstructure of the γ -Si ₃ N ₄ /Hf ₃ N ₄ nanocomposite. (b) TEM image acquired from a, the inset is a SAED image taken from the red box region. (c) TEM image and corresponding SAED image. (d) TEM image shows grain boundaries between Hf ₃ N ₄ and γ -Si ₃ N ₄ crystals. (e) HR-TEM micrograph magnified from the red box area in d, showing lattice fringes from an imperfect γ -Si ₃ N ₄ single crystal with some embedded nanospheres of Hf ₃ N ₄ . (f) Hf ₃ N ₄ nano particles embedded in γ -Si ₃ N ₄ . (g) TEM image obtained from the white circled area in image a, the white arrows	

represent nanopores. (h) HR-TEM image shows the interaction relationship between γ -Si ₃ N ₄ , Hf ₃ N ₄ nanograins and nanopores. (i) HR-TEM micrograph magnified from the interphase area.	59 -
Figure 3. 21 SEM graph and elemental mappings of the γ -Si ₃ N ₄ /Hf ₃ N ₄ ceramic nanocomposites, indicating homogeneous Si, Hf, and N elemental distributions.	60 -
Figure 3. 22 Hardness and fracture toughness of the γ -Si ₃ N ₄ /Hf ₃ N ₄ nanocomposite as a function of indentation loads in the range of 0.49 N–19.6 N. The inset is a representative SEM indentation image showing cracks under an indentation load of 19.6 N.	61 -
Figure 3. 23 SEM image of the indentation and cracks at 9.8 N, yellow arrows indicate transgranular cracks. Insets are the simulation path of crack propagation (The hexagons show the grain, and the red color represents the crack).....	62 -
Figure 3. 24 FTIR spectra of BMS, pristine PHPS, BPSZ5, BPSZ2 and BPSZ1.	67 -
Figure 3. 25 Proposed pathway of the reaction of PHPS with TDMAH and BMS.....	68 -
Figure 3. 26 FT-IR spectra of BMS, PHPS, TDMAH, and BHPSY precursors.....	69 -
Figure 3. 27 XPS spectra of BHPS5 precursor (a) B 1s; (b) C 1s; (c) N 1s; (d) Si2p.	69 -
Figure 3. 28 TG (a), DTA (b) and temperature vs time curves of the BHPSY precursor under flowing ammonia/argon atmosphere (90 vol.% NH ₃).....	70 -
Figure 3. 29 FT-IR spectra of BHPS5 annealed at different temperatures.	71 -
Figure 3. 30 XPS spectra of SiHfBN5 sample heat-treated at 400 °C (a) B 1s; (b) C 1s; (c) N 1s; (d) Si 2p.....	71 -
Figure 3. 31 XPS spectra of SiHfBN5 sample pyrolyzed at 1000 °C (a) B 1s; (b) C 1s; (c) N 1s; (d) Si 2p.....	72 -
Figure 3. 32 XRD patterns of SiHfBN ceramics upon heat treatment in the temperature range of 1000–1700 °C under different atmospheres: (a) 1000 °C (NH ₃), (b) 1300 °C (N ₂), (c) 1500 °C (N ₂), (d) 1700 °C (N ₂).....	73 -
Figure 3. 33 Rietveld refinement of SiHfBN2_1700 XRD pattern.	74 -

Figure 3. 34 TEM images of the SiHfBN_1000 (a and b) and SiHfBN_1300 (c and d) bulk ceramics; (b) and (d) are high resolution images magnified from (a) and (c), respectively; the inset in (b) and (d) is the SAED images. - 75 -

Figure 3. 35 TEM images of bulk SiHfBN_1500 (a and b, b is a high-resolution image enlarged from a) and SiHfBN_1700 (c and d, d is a high-resolution image magnified from c); the insets in (a) and (c) are SAED images; the insets in (b) and (d) are FFT images from the selected areas. - 76 -

Figure 3. 36 Weight changes with the variation of oxidation times for bulk SiHfBN_1700 samples at 1500 °C..... - 77 -

Figure 3. 37 XRD patterns of bulk SiHfBN_1700 samples oxidized at 1500 °C in static air. - 78 -

Figure 3. 38 Quaternary isothermal phase diagram SiHfBN with the two-phase subsystems, Si₃N₄, HfN, HfB and BN. The analyzed crystalline ternary HfBN phase is part of the three-phase field Hf, N and B with compositions located on the tie line marked in red between NaCl-type HfB and HfN. - 79 -

List of tables

Table 2. 1 Processing techniques applied in the PDC route and ceramic.....	- 11 -
Table 2. 2 Crystallographic data of Si ₃ N ₄ [1, 163, 168].	- 19 -
Table 2. 3 Typical properties of structural ceramics (HIP: Hot Isostatic Press; PS: Pressureless Sintering; RS: Reaction Sintering; HP: Hot Press) [3, 6, 172-174].	- 20 -
Table 2. 4 General stage during solid phase sintering.	- 21 -
Table 2. 5 Physical and mechanical properties of Si ₃ N ₄ [195-200].	- 24 -
Table 2. 6 Morphologies and mechanical properties of Si ₃ N ₄ -based ceramics [209, 210].	- 25 -
Table 3. 1 Elemental composition of the annealed SiHfN ceramics.	- 40 -
Table 3. 2 Results of the Rietveld refinements.	- 44 -
Table 3. 3 Refined structural parameters.	- 46 -
Table 3. 4 Composition, preparation temperatures and notation of the synthesized BPSZX, BHPSY precursors and SiHfBN-based bulk samples.	- 65 -

List of abbreviations

PDCs	Polymer-derived ceramics
SSPs	Single-source precursors
HPHT	High pressure high temperature
SPS	Spark plasma sintering
HP	Hot press
PLS	Pressureless sintering
HIP	High isostatic pressing
PHPS	Perhydropolysilazane
TDMAH	Tetrakis(dimethylamido) hafnium
BMS	Borane dimethyl sulfide complex
CCVD	Chemical catalytic vapor deposition
CVI	Chemical vapor infiltration
CMCs	Ceramic matrix composites
SSPs	Single-source precursors
PDC-NCs	Polymer-derived ceramic nanocomposites
CMC	Ceramic–matrix composites
FT-IR	Fourier transformed infrared spectroscopy
ATR	Attenuated-total-reflectance
TGA	Thermogravimetric analysis
TG/MS	Thermogravimetric analysis coupled with mass spectrometry
NMR	Nuclear magnetic resonance

MAS NMR	Magic-angle spinning nuclear magnetic resonance
XRD	X-ray diffraction
TEM	Transmission electron microscopy
HRTEM	High-resolution transmission electron microscopy
SEAD	Selected Area Electron Diffraction
SEM	Scanning electron microscopy
XPS	X-ray photoelectron spectroscopy
<i>wt% / vol% / mol%</i>	Weight percent/Volume percent/Mol percent

Abstract

In the last few years, numerous efforts have been explored to add metal-based (nano)powders into Si_3N_4 to prepare particle reinforced Si_3N_4 -based composites using hot pressed sintering, pressureless sintering or hot isostatic pressing. However, all of these methods generally require sintering temperature up to 2000 °C, long hold times and/or high applied loads as well as sintering aids due to its high melting point and low self-diffusion coefficient. Until now, most of the Si_3N_4 -based composites are fabricated by using traditional powder techniques, but the grain sizes of the composites are limited to the micrometer range, and the dispersion of metal-compound particles is not homogeneous. In recent years, it has been proven that polymer-derived ceramic (PDC) approach can prepare ceramic composites to reach nano scale, showing outstanding behavior at (ultra)high temperatures. Moreover, single-source precursors (SSPs) can be easily tailored by the design of the molecular precursor, which provides the possibility of designing ceramic nanocomposites with unique phase compositions, microstructures, properties. Therefore, the PDC route is considered to be the most promising approach in fabrication of homogeneous ceramic nanocomposites with unique nanostructures by pyrolysis of suitable SSPs at low sintering temperatures. The motivation of this thesis is to further develop the concept for fabrication of SiHf(B)N ceramic nanocomposites with versatile properties by molecular design of their SSPs and to gain a better understanding of the manyfold “composition-structure-property” interrelationship.

With this motivation, additive-free amorphous bulk SiHfN ceramic was fabricated using SSP synthesis plus warm pressing. The densification mechanism of warm-pressing *in-situ* consolidation of preceramic polymer powders was identified based on cross-linking reactions monitored by TGA/DTA and FT-IR measurements. The critical problems concerning gas evolution and crystallization inducing bloating and cracking are addressed through controlled thermolysis and pressure. Then the microstructural evolution of the polymer-to-ceramic transformation was characterized using XRD, TGA, elemental analysis, SEM and TEM. The results indicate that the incorporation of Hf in perhydropolysilazane (PHPS) not only increases the ceramic yield (97.4 wt%) and crystallization resistance (1300 °C), but also suppresses the transformation from $\alpha\text{-Si}_3\text{N}_4$ to $\beta\text{-Si}_3\text{N}_4$ at high temperatures (1700 °C). The high-temperature microstructural evolution of the amorphous SiHfN ceramic demonstrates that α - and $\beta\text{-Si}_3\text{N}_4$ were obtained during the high-temperature treatment (1500 °C, 1700 °C) and form a matrix, in which nano-sized HfN crystallites were homogeneously dispersed. Furthermore, the nanohardness and microhardness of the obtained additive-free amorphous bulk SiHfN ceramic are up to 17 GPa and 19.6 GPa, respectively, which shows a significant improvement in comparison to most of the reported amorphous and polycrystalline Si_3N_4 -based ceramics.

The second focus of this Ph.D. work is the synthesis of $\gamma\text{-Si}_3\text{N}_4/\text{Hf}_3\text{N}_4$ ceramic nanocomposites as well as the investigation of the relationship between mechanical properties and nanostructures. The phase evolution of single-phase amorphous SiHfN ceramic was studied *in-situ* at HP-HT conditions with

energy-dispersive X-ray diffraction (ED-XRD) using synchrotron radiation. The results show that the amorphous SiHfN phase starts to separate into γ -Si₃N₄ and Hf₃N₄ from 1090 °C under 19.5 GPa. There are no further structural changes in the XRD patterns up to ~1570 °C, while rock salt-type HfN was observed at temperature far beyond 1570 °C, indicating that Hf₃N₄ decomposes into rock salt-type HfN and N₂ at that temperature. Therefore, the optimal HP-HT conditions for the formation and stability of the γ -Si₃N₄/Hf₃N₄ ceramic nanocomposites was determined as 20 GPa and 1500 °C. Furthermore, the investigation of mechanical properties reveals that the fracture toughness of the resultant γ -Si₃N₄/Hf₃N₄ (6.98 MPa m^{1/2}) ceramic nanocomposite exhibits a significant improvement over pure γ -Si₃N₄ (3.5 MPa m^{1/2}) without sacrificing the hardness of the material, making it a competitive ceramic candidate for technological applications in harsh conditions.

The third focus of this Ph.D. work is placed on the synthesis of novel polymer-derived SiHfBN ceramics. They were prepared *via* the heat treatment of a series of B/Hf-containing SSPs which were synthesized by the modification reaction of PHPS with borane dimethyl sulfide complex (BMS) and tetrakis(dimethylamido) hafnium(IV) (TDMAH). The chemical reaction to synthesize the SSPs was confirmed by FT-IR and XPS, in which both Si–H and N–H groups of PHPS react with BMS and TDMAH. The polymer-to-ceramic conversion was characterized using TGA/TDA, FT-IR as well as XPS. The SiHfBN precursors synthesized using BMS and TDMAH lead to high ceramic yield (\approx 100 wt.%) upon pyrolysis at 1000 °C under ammonia atmosphere, which is higher than those of the pristine PHPS (78 wt%), boron-modified PHPS (92 wt%) and hafnium-modified PHPS (97 wt%). The resultant SiHfBN ceramic exhibits high-temperature resistance against crystallization up to 1500 °C. The conversion of the amorphous SiHfBN ceramics into Si₃N₄/HfB_xN_{1-x} ceramic nanocomposites was observed by XRD after annealing at 1700 °C in N₂ atmosphere, and extensive TEM characterizations reveal the homogeneous dispersion of HfB_xN_{1-x} in the Si₃N₄ matrix. Furthermore, the oxidation behavior of warm-pressed bulk Si₃N₄/HfB_xN_{1-x} ceramic nanocomposites was investigated at 1500 °C, indicating that the SiO₂-B₂O₃ glass (i.e., borosilicate) formed between low-viscous B₂O₃ and high-viscous SiO₂ glass leads to a dense and continuous protective barrier against inward diffusion of O₂.

In summary, the present Ph.D. work deeply investigated the single-source-precursor synthesis, polymer-to-ceramic conversion, the microstructural evolution of final SiHf(B)N ceramics as well as densification of SiHf(B)N ceramic nanocomposites without sintering additives. The main findings are as follows: (1) Novel single-source precursors are successfully synthesized via chemical reactions; (2) Additive-free bulk SiHf(B)N ceramics could be fabricated using the PDC route plus warm pressing; (3) Si₃N₄/X (X = HfN, Hf₃N₄) ceramic nanocomposites with a homogeneous microstructure can be obtained by further annealing at higher temperatures. Moreover, the correlations between molecular design, compositions, microstructure and properties of the SiHf(B)N ceramic nanocomposites were carefully discussed, which provides new insights into the design and synthesis of metal-compound-modified Si-based ceramic nanocomposites via the PDC approach.

Zusammenfassung

In den letzten Jahren wurden zahlreiche Versuche unternommen, Metall-basierte (Nano-)Pulver in Si_3N_4 einzubringen, um partikelverstärkte Verbundwerkstoffe auf Si_3N_4 -Basis durch Heißpressen, druckloses Sintern oder heißostatisches Pressen herzustellen. All diese Verfahren erfordern jedoch Sintertemperaturen von bis zu $2000\text{ }^\circ\text{C}$, lange Haltezeiten und/oder hohe Drücke sowie die Zugabe von Sinteradditiven aufgrund des hohen Schmelzpunkts und niedriger Selbstdiffusionskoeffizienten. Bislang werden die meisten Verbundwerkstoffe auf Si_3N_4 -Basis mit Hilfe traditioneller Pulvertechniken hergestellt, doch sind die Korngrößen der Verbundwerkstoffe auf den Mikrometerbereich beschränkt, und die Metallverbindungspartikel sind nicht homogen verteilt. In den letzten Jahren hat sich gezeigt, dass mit dem PDC-Verfahren (Polymer-Derived) keramische Verbundwerkstoffe im Nanometerbereich hergestellt werden können, die ein hervorragendes Verhalten bei (ultra)hohen Temperaturen zeigen. Darüber hinaus können sogenannte Einkomponentenvorstufen (Single-Source-Precursor (SSP)) mit auf molekularer Ebene gezielt eingestellter Zusammensetzung synthetisiert werden, was die Möglichkeit bietet, daraus keramische Nanoverbundwerkstoffe mit einzigartiger Phasenzusammensetzung, Mikrostruktur und Eigenschaften herzustellen. Daher gilt die PDC-Route als der vielversprechendste Ansatz zur Herstellung homogener keramischer Nanokomposite durch Pyrolyse geeigneter SSP bei niedrigen Temperaturen. Ziel dieser Arbeit ist, SiHf(B)N -Nanokomposite mit vielseitigen Eigenschaften durch molekulares Design geeigneter Einkomponentenvorstufen herzustellen und die Zusammenhänge zwischen Zusammensetzung, Mikrostruktur und Eigenschaften zu analysieren.

Aus diesem Grund wurde eine additivfreie amorphe SiHfN -Keramik durch SSP-Synthese und Warmpressen hergestellt. Die Verdichtung der präkeramischen Polymerpulver erfolgte durch Warmpressen, begleitet durch TGA/DTA- und FT-IR-Messungen. Die kritischen Faktoren bei der Polymer-Keramik-Transformation sind Gasentwicklung und Kristallisation, die zu Aufblähung und Rissbildung der Proben führen können und die durch kontrollierte Thermolyse und Druck beeinflusst werden können. Nach der Polymer-Keramik-Umwandlung wurde die Entwicklung der Mikrostruktur mit Hilfe von XRD, TGA, Elementaranalyse, SEM und TEM charakterisiert. Die Ergebnisse zeigen, dass der Einbau von Hf in Perhydropolysilazan (PHPS) nicht nur die Keramikausbeute ($97.4\text{ wt}\%$) und die Kristallisationsbeständigkeit ($1300\text{ }^\circ\text{C}$) erhöht, sondern auch die Umwandlung von $\alpha\text{-Si}_3\text{N}_4$ in $\beta\text{-Si}_3\text{N}_4$ bei hohen Temperaturen ($1700\text{ }^\circ\text{C}$) unterdrückt. Die mikrostrukturelle Entwicklung der amorphen SiHfN -Keramik bei hohen Temperaturen zeigt, dass $\alpha\text{-}$ und $\beta\text{-Si}_3\text{N}_4$ während der Hochtemperaturbehandlung ($1500\text{ }^\circ\text{C}$, $1700\text{ }^\circ\text{C}$) gebildet wurden und eine Matrix bilden, in der HfN-Nanokristalle homogen verteilt sind. Darüber hinaus betragen die Nanohärte und die Mikrohärtigkeit der erhaltenen additivfreien amorphen SiHfN -Keramik bis zu 17 GPa bzw. 19.6 GPa , was eine deutliche Verbesserung im Vergleich zu den literaturbekannten amorphen und polykristallinen Si_3N_4 -basierten Keramiken darstellt.

Der zweite Schwerpunkt dieser Doktorarbeit ist die Hochdrucksynthese keramischer γ - $\text{Si}_3\text{N}_4/\text{Hf}_3\text{N}_4$ -Nanokomposite sowie die Untersuchung der Zusammenhänge zwischen mechanischen Eigenschaften und Nanogefüge. Die Phasenentwicklung der einphasigen amorphen SiHfN-Keramik wurde in-situ unter HP-HT-Bedingungen mit energiedispersiver Röntgenbeugung (ED-XRD) unter Verwendung von Synchrotronstrahlung untersucht. Die Ergebnisse zeigen, dass die amorphe SiHfN-Phase ab 1090 °C bei 19.5 GPa beginnt, sich in γ - Si_3N_4 und Hf_3N_4 umzuwandeln. In den Röntgendiffraktogrammen sind bis \sim 1570 °C keine weiteren strukturellen Veränderungen zu erkennen, während bei Temperaturen weit über 1570 °C HfN mit Kochsalzstruktur vorliegt, was darauf hindeutet, dass sich Hf_3N_4 bei dieser Temperatur zu HfN und N_2 zersetzt. Daher wurden die optimalen HP-HT-Bedingungen zur Bildung stabiler keramischer γ - $\text{Si}_3\text{N}_4/\text{Hf}_3\text{N}_4$ -Nanokomposite auf 20 GPa und 1500 °C festgelegt. Darüber hinaus zeigt die Untersuchung der mechanischen Eigenschaften, dass die Bruchzähigkeit des entstandenen keramischen Nanokomposits aus γ - $\text{Si}_3\text{N}_4/\text{Hf}_3\text{N}_4$ ($6.98 \text{ MPa m}^{1/2}$) eine deutliche Verbesserung gegenüber reinem γ - Si_3N_4 ($3.5 \text{ MPa m}^{1/2}$) aufweist, ohne dass die Härte des Materials darunter leidet. Dies macht den Nanokomposit zu einer wettbewerbsfähigen Keramik für technologische Anwendungen unter harschen Bedingungen.

Der dritte Schwerpunkt vorliegender Doktorarbeit liegt auf der Synthese neuartiger SiHfBN-Keramiken auf Polymerbasis. Die Keramiken wurden durch die Wärmebehandlung einer Reihe von B/Hf-haltigen SSPs hergestellt, die durch Modifikation von PHPS mit Boran-Dimethylsulfid-Komplex (BMS) und Tetrakis(dimethylamido)-Hafnium(IV) (TDMAH) synthetisiert wurden. Die chemische Reaktion, bei der sowohl die Si-H- als auch die N-H-Gruppen von PHPS mit BMS und TDMAH reagieren, wurde durch FT-IR und XPS bestätigt. Die Umwandlung des Polymers in die Keramik wurde mit TGA/TDA, FT-IR und XPS charakterisiert. Die unter Verwendung von BMS und TDMAH synthetisierten SiHfBN-Vorstufen führen bei der Pyrolyse bei 1000 °C unter Ammoniakatmosphäre zu einer hohen Keramikausbeute (\approx 100 wt%). Diese ist höher als die des reinen PHPS (78 wt%), des mit Bor modifizierten PHPS (92 wt%) und des mit Hafnium modifizierten PHPS (97 wt%). Die resultierende SiHfBN-Keramik weist eine hohe Temperaturbeständigkeit gegen Kristallisation bis zu 1500 °C auf. Die Umwandlung der amorphen SiHfBN-Keramik in keramische $\text{Si}_3\text{N}_4/\text{HfB}_x\text{N}_{1-x}$ -Nanokomposite wurde mittels XRD ab 1700 °C in N_2 -Atmosphäre analysiert, und umfangreiche TEM-Charakterisierungen zeigen die homogene Verteilung von $\text{HfB}_x\text{N}_{1-x}$ in der Si_3N_4 -Matrix. Darüber hinaus wurde das Oxidationsverhalten warmgepresster $\text{Si}_3\text{N}_4/\text{HfB}_x\text{N}_{1-x}$ -Nanokomposite bei 1500 °C untersucht, was darauf hindeutet, dass das zwischen niedrigviskosem B_2O_3 und hochviskosem SiO_2 -Glas gebildete SiO_2 - B_2O_3 -Glas (Borsilicatglas) zu einer dichten und kontinuierlichen Schutzschicht gegen Diffusion von O_2 in das Materialinnere führt.

Zusammenfassend kann gesagt werden, dass in der vorliegenden Doktorarbeit die Single-Source-Precursor-Synthese, die Polymer-zu-Keramik-Umwandlung, die mikrostrukturelle Entwicklung der SiHf(B)N-Keramik sowie die Verdichtung von SiHf(B)N-Keramik-Nanokompositen ohne

Sinteradditive eingehend untersucht wurden. Die wichtigsten Ergebnisse sind wie folgt: (1) Synthese neuartiger Single-Source-Präkursoren; (2) Herstellung additivfreier SiHf(B)N-Keramik über die PDC-Route via Warmpressen; (3) Bildung keramischer $\text{Si}_3\text{N}_4/\text{X}$ ($\text{X} = \text{HfN}, \text{Hf}_3\text{N}_4$) Nanokomposite mit homogener Mikrostruktur durch weiteres Erhitzen bei höheren Temperaturen. Darüber hinaus wurde die Korrelation zwischen molekularem Design, Zusammensetzung, Mikrostruktur und Eigenschaften der SiHf(B)N-Nanokomposite untersucht, die neue Erkenntnisse zum Design und zur Synthese metallverbindungsmodifizierter keramischer Nanokomposite auf Si-Basis über den PDC-Ansatz ermöglicht.

1. Introduction and motivation

Silicon nitride (Si_3N_4) exists in three modifications, the well-known α - and β - Si_3N_4 , and a newly high-pressure synthesized γ - Si_3N_4 . The practical application of γ - Si_3N_4 has been rarely reported, but it has potential to be used as a super hard material due to its high hardness (ca. 43 GPa) and shear modulus (ca. 148 GPa) [1, 2]. α/β - Si_3N_4 are advanced ceramic materials that meet the requirements of mechanical, electronic, decorative and microwave-transparent applications because of its excellent properties, such as chemical stability, high mechanical strength, fracture toughness, wear resistance, high modulus of elasticity, dielectric properties and low thermal expansion. Moreover, the density of α/β - Si_3N_4 is ca. $3.2 \text{ g}\cdot\text{cm}^{-3}$, which is only about 40% that of high-temperature superalloys. This combination of properties makes it an attractive candidate to replace metallic components that are conventionally used as structural materials [3-5]. However, it is very difficult to produce fully dense Si_3N_4 -based ceramics due to its high melting point and low self-diffusion coefficient. As a consequence, numerous efforts have been explored to assist the densification, such as by introducing sintering additives and/or using pressure-assisted techniques (e.g., hot-pressing, spark plasma sintering and gas pressure sintering) [5-8]. The sintering additive leads to the formation of intergranular glassy phases located at the Si_3N_4 grains boundary and unavoidably impair the high temperature behavior such as oxidation/corrosion, creep resistance and strength. Although pressure-assisted sintering promotes the densification of the sample, this method is quite complicated and costly, and has serious limitations when it comes to preparation of products with complex shapes. Therefore, introducing new preparation method to fabricate fully dense Si_3N_4 -based ceramics without sintering aids becomes of technological interest for the application of Si_3N_4 at elevated temperatures and under harsh conditions.

Recently, it has been discovered that ceramic composites with nano-reinforcing phases show outstanding behavior at (ultra)high temperatures, which leads to a “Ceramic Nanocomposites Concept” [9, 10]. Therefore, ceramic nanocomposites have become a hot research topic and achieved some progress recently [10-12]. For example, TiN/ Si_3N_4 nanocomposites were prepared by nano-sized amorphous Si_3N_4 (20 nm), α - Si_3N_4 (100 nm) and TiN (40 nm) powders using hot pressing. The flexural strength and fracture toughness of the obtained nanocomposites were found to be ca. 675 MPa and $7.0 \text{ MPa}\cdot\text{m}^{1/2}$, respectively, which were higher than that of Si_3N_4 without the incorporation of TiN nanophase (500 MPa for flexural strength and $6.0 \text{ MPa}\cdot\text{m}^{1/2}$ for fracture toughness) [13]. However, there are difficulties in the preparation of ceramic nanocomposites by conventional powder techniques. The major challenge is the restriction of grain growth during preparation. Another difficulty is the inability to ensure final products with homogeneous and stable structures because of agglomeration of starting nanopowders. In the context of this issue, the development and adoption of advanced processing techniques have been the subject of extensive research over the last few decades.

The polymer-derived ceramic (PDC) route is considered to be the most promising method for the preparation of amorphous and/or multielement ceramic nanocomposites by pyrolysis of suitable single-source precursors at low sintering temperature. On the one hand, the polymeric single-source precursors (SSPs) can be tailored at the molecular level, final products with tunable chemical composition and homogeneous elemental distribution can be consequently achieved. On the other hand, pyrolysis of the SSPs can be controlled to obtain amorphous and/or nanocrystalline materials at different temperatures, which provides access to metastable compounds compared to other synthesis approaches. Another advantage is that polymer shaping techniques can be applied for PDCs due to the polymer properties of preceramic polymers. This provides the possibility to prepare complex shapes and shapes which are difficult to achieve by traditional powder-based route, such as layers, fibers and ceramic matrix composites. In consequence, the PDC route opens up a great opportunity to prepare novel ceramic nanocomposites with various compositions, states and complex shapes. Over the past few decades, series of single-phase amorphous SiMN/SiMC/SiMBCN (M= transition metal) ceramics [14-16], carbide as well as nitride ceramic nanocomposites (e.g., SiC/HfC [17], SiC/TaC [18], Si₃N₄/HfN [19]) were prepared starting from suitable metal-modified precursors which were ceramized and subsequently annealed at high temperatures.

As aforementioned, Si₃N₄-based ceramic is a covalent compound and self-diffusion coefficient is too low to be fully consolidate. Thus, it is necessary to develop alternative processing techniques that can avoid the use of sintering aids to allow the production of Si₃N₄-based ceramic with a compositional homogeneity. In a recent study, a new strategy based on the PDC route in combination with a warm-pressing process has been developed and has attracted increasing attention due to avoiding the use of sintering additives while maintaining a high density. The innovative idea behind this procedure is that the density of the final product is designed by the atomic composition and the structure of the preceramic polymer as well as low-temperature (< 300 °C) warm pressing conditions. Moreover, amorphous ceramic monoliths and their composites can be obtained by adjusting the pyrolysis temperature, which is difficult to achieve by the traditional powder-based route. Amorphous SiHfBCN ceramic monoliths with low-rate parabolic oxidation behavior were first reported by Yuan et al. using the PDC route and uniaxial warm pressing [20]. In the same period, Bechelany et al. reported the investigation of TiN@a-Si₃N₄ (a=amorphous) bulk ceramic nanocomposites fabricated by the PDC route and warm-pressing method, in which TiN nanocrystallites are homogeneously embedded in an amorphous Si₃N₄ matrix [21]. The nanohardness of the obtained nc-TiN@a-Si₃N₄ is comparable to that of Si₃N₄ obtained at 1850 °C (24.9 GPa) [22] and the microhardness is higher than that of TiN@Si₃N₄ composites prepared by SPS [23]. The above methods open a new strategy to fabricate additive-free amorphous Si₃N₄- and polycrystalline Si₃N₄-based (nano)composites. Parts of this Ph.D work are carried out based on the above approaches.

High pressure high temperature (HPHT) synthesis is another attractive method to prepare dense Si₃N₄

ceramic without sintering aids. Moreover, High pressure condition prevents the recrystallization process and limits the grain growth owing to the reduced diffusion of atoms and short holding times at the final synthesis temperature. Dense and submicron-sized (263 nm) β - Si_3N_4 monolithic samples were synthesized using micron-sized α - Si_3N_4 powders (2 μm) as the starting material under HPHT conditions [24]. The measured Vickers hardness of the as-obtained β - Si_3N_4 could reach up to 20 GPa, approaching the limit value of the single crystal β - Si_3N_4 . This study indicates that HPHT technique is an efficient pathway to synthesize dense and micron/nano-sized ceramics without sintering aids. Furthermore, γ - Si_3N_4 possessing a spinel-type structure was discovered under HPHT in 1999 [1]. The studies show that γ - Si_3N_4 is one of the hardest material after diamond and cubic boron nitride (cBN), and has higher thermal stability than diamond and cBN, making it a competitive candidate for technological applications in harsh conditions (e.g. drill head, abrasive and cutting tools) [25, 26]. Therefore, the synthesis of γ - Si_3N_4 has attracted great attention and made some progress in the recent years [1, 25-27]. However, the research on the synthesis of γ - Si_3N_4 -based ceramic nanocomposites as well as the investigation of their mechanical properties has not been reported yet and it is still a challenging work for the preparation of γ - Si_3N_4 -based nanocomposites due to the limitations of suitable starting materials and HPHT techniques. In the present Ph.D. work, the successful synthesis of γ - $\text{Si}_3\text{N}_4/\text{Hf}_3\text{N}_4$ ceramic nanocomposites will be explored based on the PDC route in combination with HPHT technology.

2 Literature review

In this chapter, the fundamentals and basic principles underlying the scientific findings of the present thesis are introduced and discussed with respect to the latest research developments. Therefore, the main objective of this chapter is to provide a literature review of polymer-derived ceramics (PDCs), Si_3N_4 ceramics and ceramic composites from various sources, prioritizing fundamentals and results associated with the main topic.

2.1 Polymer-derived ceramics (PDCs)

In the following subchapters, the basic background of PDCs will be given, focusing on an overview in the PDC field, and the synthesis of preceramic precursors as well as the processing and thermal conversion of PDCs. Additionally, a short introduction in polymer-derived ceramic nanocomposites (PDC-NCs) will be given.

2.1.1 PDC route: principle, history and recent developments

The PDC route is a relatively young technology for ceramic manufacturing compared with ceramic powder technology, which brings a significant technological breakthrough for the development of ceramic science and technology. The principle of PDCs is to prepare ceramics with desired properties by the thermolysis of inorganic/organometallic polymers (denoted as preceramic precursors) in a controlled atmosphere. There are several types of preceramic precursors for the synthesis of PDCs: precursors to oxides, carbides and nitrides, are used to prepare such ceramics as SiOC , SiC , Si_3N_4 , SiCN , BCN and TiC . The research of PDC precursors have been predominantly focused on silicon-based systems because they are developed based on silicon chemistry. A general formula of an organosilicon polymer is presented in Figure 2. 1. The backbone X defines the class of the polymer, such as poly(organosilanes) with $\text{X}=\text{Si}$, poly(organosiloxanes) with $\text{X}=\text{O}$, poly(organocarbosilanes) with $\text{X}=\text{CH}_2$, poly(organosilazanes) with $\text{X}=\text{NH}$, and poly(organosilylcarbodiimides) with $\text{X}=[\text{N}=\text{C}=\text{N}]$. The functional groups R^1 and R^2 attached at the silicon atoms are usually hydrogen, aliphatic or aromatic groups, which provides opportunities to design polymer precursors at the nanoscale level. Therefore, the chemical composition and microstructure of the synthesized ceramics can be tuned by appropriate control of organic side groups (R^1 and R^2) and process parameters to tailor products to suit the specific requirements of specific applications, which will give more details in the next section.

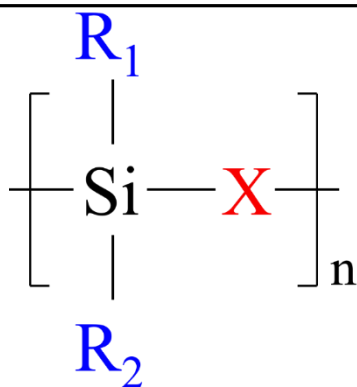


Figure 2. 1 Schematic diagram of general molecular structure of preceramic organosilicon compounds [28].

The timeline in the research field of PDCs is shown in Figure 2. 2. The conversion of polymer precursors to ceramics was first reported by Fritz and Raabe in 1956 [29], in which the thermal decomposition of $\text{Si}(\text{CH}_3)_4$ and $\text{Si}(\text{C}_2\text{H}_5)_4$ to form Si–C bonds was investigated, despite the original purpose of this pioneering work was not to synthesize SiC precursors. In the early 1960s, a series of molecular precursors have been gradually reported for the preparation of non-oxide ceramics via polymer-to-ceramic transformation process [30, 31]. However, as shown in the Figure 2. 2, the studies during this period were focused on the synthesis of binary PDCs. Since the works reported by Veerbeek [32, 33], Winter [34], and Yajima [35-39] in 1970s, numerous studies has been conducted and developed to better understand chemical synthesis of precursors, polymer-to-ceramic conversion process, and their microstructural evolution at high temperatures. Furthermore, they demonstrated the possibility of producing small-diameter SiC-based and SiC/Si₃N₄-based ceramic fibers with excellent mechanical properties by thermolysis of polymeric precursors for applications at high temperatures, leading to a further explosion in the preparation of different types of PDCs from various polymeric precursors. Chemical modifications of the polymeric precursors were also developed on similar lines to tailor the compositions of polymeric precursors and thereby produce ternary ceramics (Figure 2. 1). Until then, significant improvements have been made in the development of preceramic polymers with controlled microstructures and processing behaviors, which eventually resulted in the development of non-oxide binary and ternary PDCs, such as SiC, Si₃N₄ and SiCN. Quaternary SiBCN ceramics with exceptional thermal-mechanical properties, such as stability against creep, oxidation, crystallization and phase separation, were reported at around 20st century [40-42]. For example, Riedel et al. reported outstanding thermal stability of polymer-derived SiBCN ceramics which were able to withstand decomposition and creep up to 2200 °C [42]. Recently, the research of PDCs were expanded pentanary (e.g., SiHfBCN [43] and SiHfTaCN [44]) and even higher systems (e.g., SiHfBCNO [45]). Recent advancements in the manufacturing processes, such as spark plasma sintering (SPS) [17], photocrosslinking and pyrolysis [46], precursor infiltration and pyrolysis [47], hot pressing [48] and hot isostatic pressing [49], also have paved the way for the preparation of PDCs with superior mechanical properties. In addition, the focus

in PDC research also expanded towards synthesizing porous ceramics with controllable pore sizes and morphologies for specific functional applications such as energy storage [50, 51], catalysis [52] and anode materials for lithium-ion batteries [53].

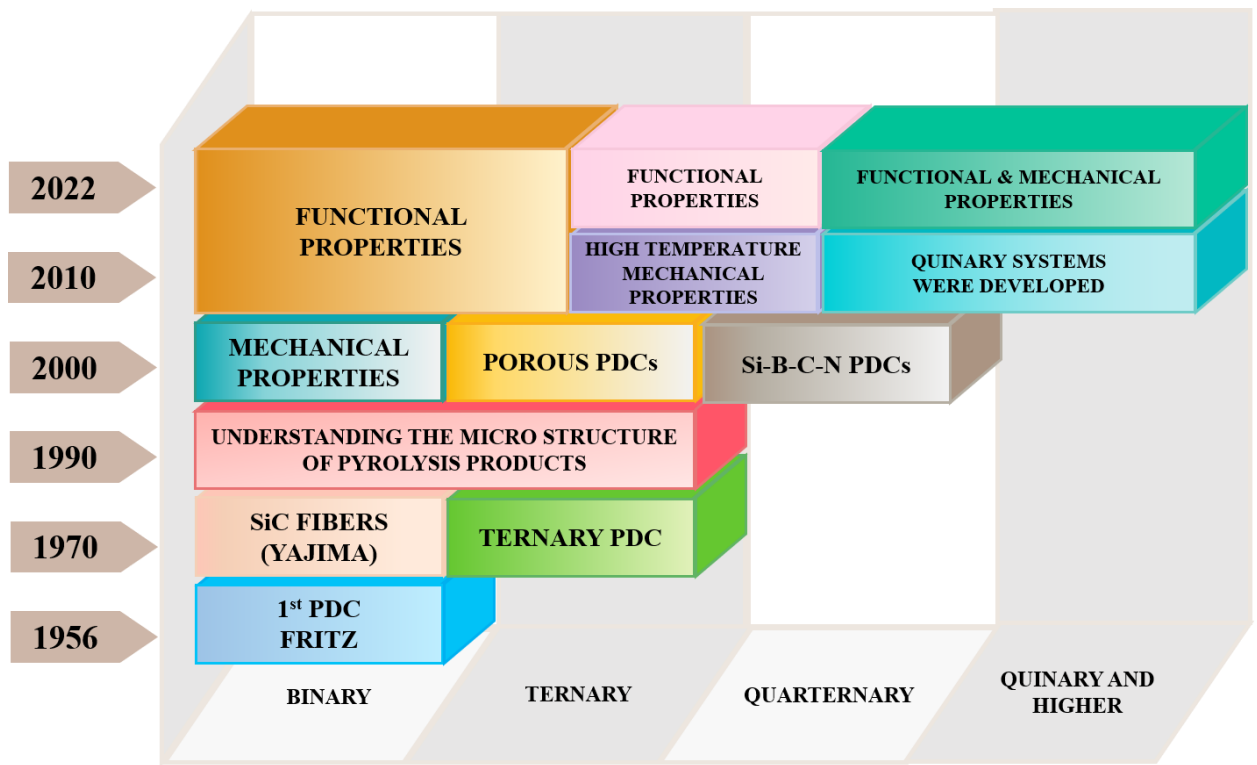


Figure 2. 2 Time line of the evolution of research in the PDC field from 1956 to present [54].

2.1.2 Synthesis of preceramic precursors

Synthesis of the preceramic precursors is a critical step in preparation of PDCs, since not only the phase composition and distribution but also the microstructure of the finally obtained ceramics are strongly influenced by the molecular structure of the preceramic precursors. In order to prepare the PDCs with expected chemical and physical properties, several types of organosilicon precursors for advanced ceramics have been synthesized by design of the precursors at the molecular level. A general oversimplified formula of Si-based precursors was shown as Figure 2. 3, it can be basically categorized according to X groups located in the backbone of the polymer molecular. The chlorosilanes (R_xSiCl_{4-x} , $x = 0 - 3$, R = organic group) are the most frequently used raw materials for the synthesis of Si-based precursors because of their high reactivity, commercial availability and low cost. As shown in Figure 2. 3, the synthetic route of Si-based precursors is usually achieved through the reaction of organic chlorosilanes with alkali metal such as lithium/sodium/potassium or ammonia/amines or water to yield polysilanes, polycarbosilanes, polysilazanes and polysiloxanes, respectively [28].

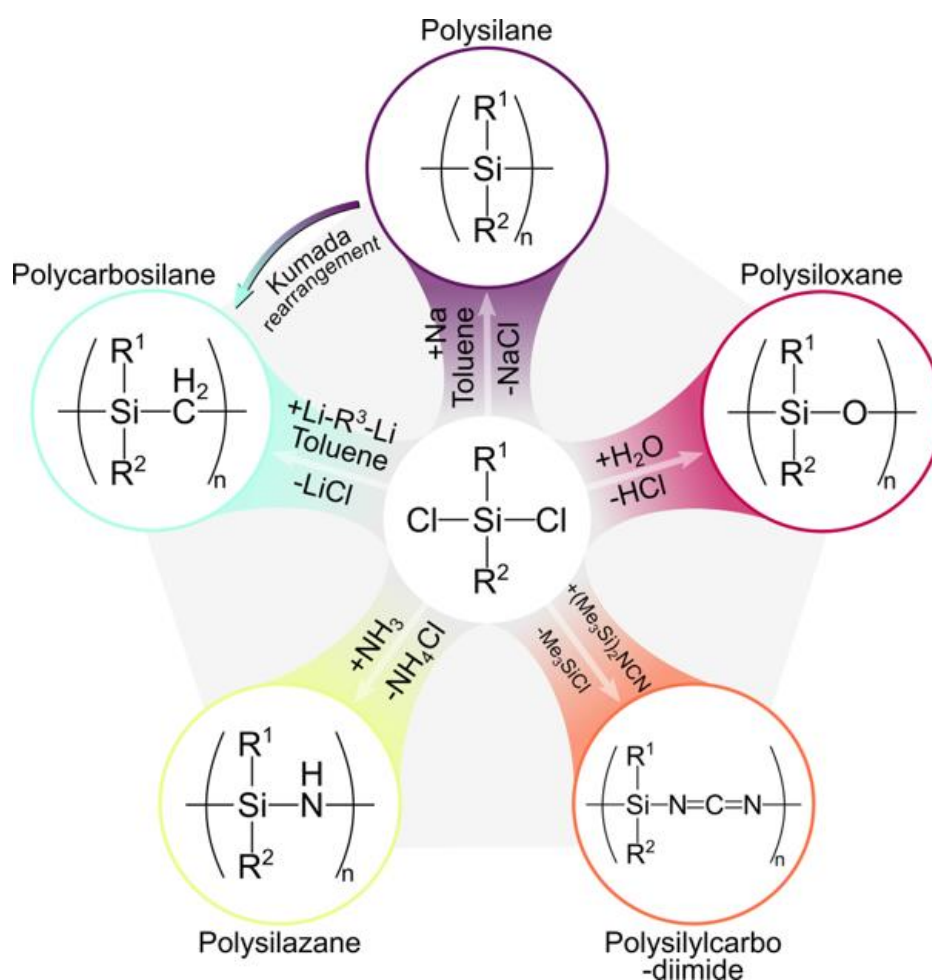


Figure 2. 3 General synthesis routes of various organosilicon polymers [28, 55].

It is worth mentioning that the side groups R_1 and R_2 also have an important effect on the properties of precursors. They can be easily substituted or modified by many different kinds of functional groups or organic compounds, leading to tailored solubility, rheological property, chemical reactivity and thermal stability and they influence the ceramic yield and structural and functional properties of the finally fabricated ceramics. In this Ph.D. work, single-source precursor route is used for the synthesis of hafnium/boron-modified PHPS-based preceramic precursors. Thus, the introduction focuses on the synthesis of metal-modified PHPS-based single-source precursor. There are three reaction pathways of Si-based precursors with metal organics, as follows: (1) Organosilicon polymer precursors can be chemically modified with oxygen-containing metallic compounds such as metal acetylacetonates [56, 57], metal alkoxides [58-61] and metal carbonyls [62-64]. The chemical modification reactions of PHPS with titanium n-butoxide (Figure 2. 4a) are reported by Iwamoto et al. [65], but only some N-Ti bonds were observed in the synthesized polymeric precursors by chemical structure analyses using FTIR and ^1H NMR. For other Si-based precursors (e.g. Polysiloxanes, Polysilazane, PCS and HTT 1800), Si-O-M, N-M or Si-M bonds could be formed with the release of alkanes or acetyl acetonates by-products.

However, oxygen is inevitably introduced into the finally produced ceramics, and oxide phases formed in the system have a detrimental effect on the high temperature properties of ceramic. Therefore, the oxygen-free metal compounds have attracted great attention in recent years. (2) The reaction between organosilicon polymer precursors and traditional oxygen-free metal compounds such as metallocene [66, 67] and metal halides [68, 69] as well as metal hydrides [70, 71]. Figure 2. 4b shows a typical synthesis process of poly(aluminasilazane)s precursor via the modification of PHPS with trimethylamine-alane adduct, $\text{AlH}_3 \cdot \text{NMe}_3$ [70]. The chemical reaction was found to occur at the N-H groups and the Si-N backbone of PHPS, but the reaction of Si-H bond was not observed, indicating the Si-H chemically inert in the PHPS. Metal-modified other Si-based precursors such as polyvinylsilazane, SMP10 and HTT 1800) can be obtained with the formation of Si-M or N-M bonds. (3) Oxygen-free metal-modified precursors can be synthesized by Si-based precursors and metal amido complexes. Compared with the previous two methods, this is a more advanced and convenient chemical approach for the fabrication of non-oxide ceramic composites by PDCs. Ti-containing single-source precursor was synthesized by the chemical reaction of PHPS with tetrakis(dimethylamino)titanium (TDMATi) [21, 72], the resultant polytitanosilazanes exhibited the proper requirements for facile processing whether in solution, melt or solid. This approach offers the possibility to design new controllable nanostructured hybrid composites and shows potential applications in ceramic coatings and fibers by tuning the viscosity of the precursors. Later, Zhou et al. reported that PHPS can be chemically modified by tetrakis(dimethylamido) hafnium(IV) (TDMAH) [19]. It is worth mentioning that the chemical modification took place at both Si-H and N-H groups in those two metal-modified PHPS precursors (Figure 2. 4c,d). Furthermore, the introduction of metal compounds results in improving in the cross-linking degree and ceramic yield of the precursor via dehydrocoupling.

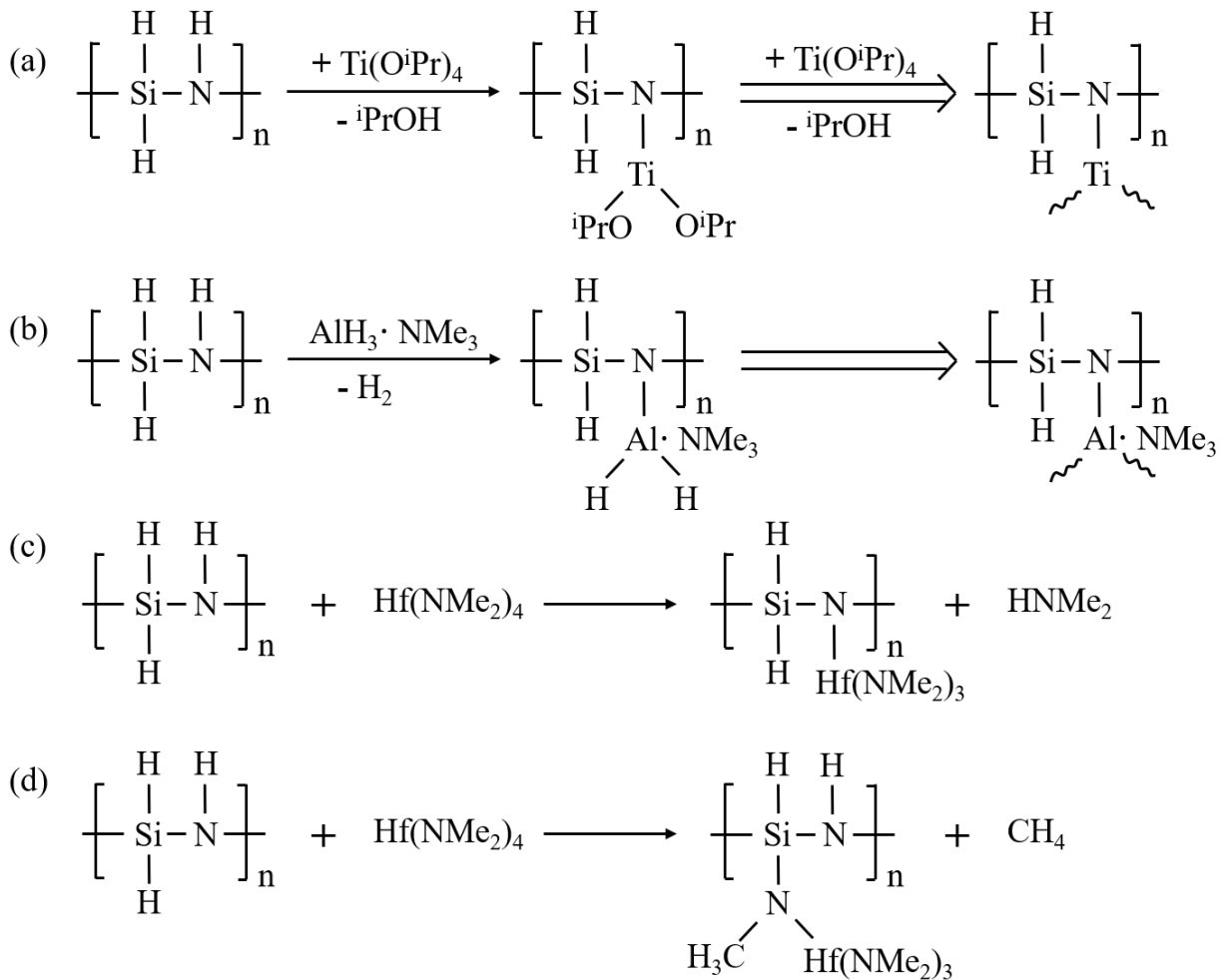


Figure 2. 4 Chemical modification of PHPS with (a) titanium n-butoxide [65], (b) aluminum hydride (trimethylamine-alane) [70], (c) and (d) tetrakis(dimethylamido) hafnium(IV) [19], respectively.

2.1.3 Processing and thermal conversion of PDCs

The polymeric nature of the preceramic precursors before heat treatment provides possibility to use plastic-forming technologies for the processing of several novel advanced ceramics with complex shapes that cannot be obtained by powder technology, such as continuous ceramic fibers, coatings, films, ceramic matrix composites, unique porous structures as well as dense monoliths prepared at relatively low temperatures [28, 73]. Unlike traditional powder technology, PDC method does not require any binder, thus simplifying the process and avoiding possible residues. Table 2. 1 and Figure 2. 5 list (shaping of the precursors) recently reported processing techniques applied in the PDC route and interested readers will find more useful information in cited literatures.

Table 2. 1 Processing techniques applied in the PDC route and ceramic part derived therefrom.

Processing Technique	Polymer derived ceramics
Coatings	SiOC coatings by spraying [74], CVD [75]
	SiBCN films via spin-coating [76], direct writing [77]
Extrusion	Polysiloxane-derived porous SiC ceramics [78]
	SiO _{1.34} C _{1.25} S _{0.15} parts [79]
Additive manufacturing	Si ₃ N ₄ ceramic based 3D printing [80]
	SiCN cellular structures from 3D printed lattices [81]
Melt spinning	SiBCN ceramic fibers by melt spinning [82]
	SiBN ceramic fibers [83]
Impregnation/infiltration	SiOC and SiCN-based ceramic [84]
	Porous Si ₃ N ₄ -SiC (BN) ceramic [85]
Cold/warm-pressing	Polyborazylene-derived bulk BN [86]
	Dense SiCN ceramics [87]
Injection molding	SiC [88]
	SiOC composites [89]
<i>In situ</i> synthesis of nanowires	<i>In-situ</i> growth of SiC nanowires in SiC aerogel [90]
Rapid prototyping	SiC coating by laser pyrolysis [91]
	Metal-doped SiOC ceramic lattices [92]
Emulsion processing	Porous Si/C/(O) bodies by emulsion processing [93]
	SiOC ceramic foam by emulsion processing [94]
Casting	Preceramic polymers by tape casting [95]
	Hierarchical porous SiOC via freeze casting [96]
Plastic forming	SiOC ceramic membranes by liquid casting [97]
	SiCN by pressure casting process [98]
Self-assembly	Si/C/N-ceramics by plastic forming [99]
	SiBCN ceramics by plastic forming [40]
Self-assembly	Self-assembled homogeneous SiOC@C/graphene [100]

A key stage of polymer-derived ceramics is their conversion from polymers to ceramics, which is achieved by cross-linking followed by pyrolysis of the preceramic polymers. Figure 2. 5 schematically illustrates the polymer-derived ceramic thermal conversion. As shown by the thermal gravimetric analysis (TGA) in Figure 2. 5, the microstructural changes of common preceramic polymers can be divided in four main stages:

(1) Release of oligomers to form thermoset polymeric network at temperatures around 400 °C, namely crosslinking. There are generally involved in four reactions in crosslinking: hydrosilylation, dehydrocoupling, transamination and vinyl polymerization. Hydrosilylation occurs in polysilazanes with Si–H and vinyl groups at 100 – 200 °C, resulting in the formation of Si–C linkages. Dehydrocoupling starts at ca. 300 °C and leads to the formation of Si–N and Si–Si bonds. The transamination process takes place in the temperature range of 200 to 400 °C, which is associated with a mass loss such as the evolution of amines, ammonia or oligomeric silazanes, leading to a decrease of the nitrogen content in the ceramic products during pyrolysis. The vinyl polymerization process starts at higher temperatures (>300 °C), which usually do not involve mass loss.

(2) Polymer decomposition and release of hydrocarbons to form amorphous materials in the temperature range of 400 – ca. 1100 °C, namely pyrolysis. Pyrolysis of the crosslinked polymer precursors occurs through rearrangement of chemical bonds and radical reactions, and is accompanied with release of hydrogen, low weight oligomers and hydrocarbons. However, the release of gas results in the formation of porosity and the weight loss (10 – 30 %). Furthermore, large volume shrinkage inevitably occurs with the progress of the ceramization process according to a densification mechanism based on surface reaction and pyrolysis of viscous flow, the linear shrinkage up to 30 % [28]. The pyrolysis process of the crosslinked materials usually completes between 800 – 1100 °C, and an amorphous material (e.g. $\text{Si}_x\text{O}_y\text{C}_z$, $\text{Si}_x\text{C}_y\text{N}_z$ and Si_xC_y ceramics produced respectively from polysiloxanes, polysilazanes and polycarbosilanes) is obtained at this temperature as illustrated in Figure 2. 5. Heat treatment at high temperature (> 1300 °C) will eventually lead to crystallization and/or decomposition (e.g. by carbothermal reactions).

(3) Dehydrogenation and phase separation to form amorphous materials with nanocrystals in the temperature range of 1000 – ca. 1500 °C. The amorphous ceramics undergo a phase separation when exposed to these elevated temperatures, in which SiO_2 , SiC, Si_3N_4 nanodomains are formed and carbon is segregated from $\text{Si}_x\text{O}_y\text{C}_z$, Si_xC_y and $\text{Si}_x\text{C}_y\text{N}_z$ amorphous ceramic matrix [101-103]. The stability of the amorphous phase is mainly influenced by the addition of other chemical elements such as carbon/boron/ aluminum [73, 104, 105] and transition metals (e.g. Hf, Zr, Ta) [44, 106, 107]. With the addition of other elements, the percolation network will form in the amorphous matrix, which acts as diffusion barriers to prevent local crystallization and keep the size of the nuclei below the critical radius [108]. Furthermore, the ability to control the nucleation of nanodomains/crystals from amorphous to crystalline states will result in a significantly different nanostructure and hence different

mechanical/functional properties [28, 51, 109].

(4) Crystallization and decomposition of the amorphous phase to form multiphase crystalline in the temperature range of 1300 °C to 2000 °C. The nucleation and growth of the crystalline grains from the amorphous matrix occur at higher temperature (> 1500 °C) due to the increase in atomic mobility and the lower energy state of the crystalline phase compared to the amorphous phase [28, 110, 111]. In addition, carbothermal reduction of SiO_2 and Si_3N_4 takes place at temperature >1500 °C due to the existence of carbon in SiCO and SiCN ceramics, which leads to the formation of SiC and a further weight loss [112, 113].

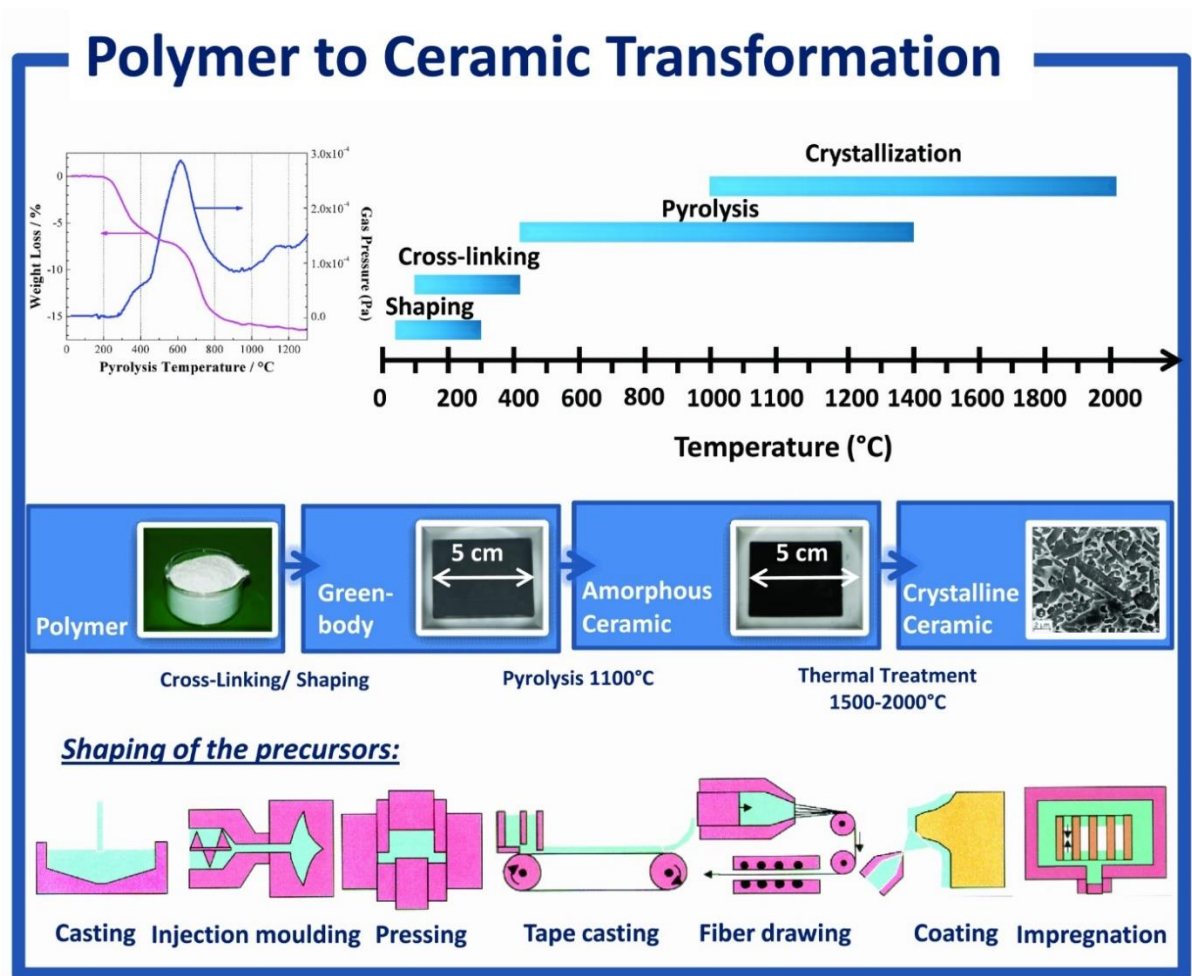


Figure 2. 5 Schematic of the polymer-to-ceramic transformation and shaping process of polymer-derived ceramics [28].

In order to ensure low weight loss and minimal shrinkage of the preceramic polymer upon pyrolysis, a high ceramic yield (α_c) is desired for the polymer-to-ceramic conversion process in PDCs, which is beneficial for the densification of ceramic products and leads to a lower tendency to form residual stresses. Typically, ceramic yield of preceramic polymers is in the range of 70 – 90 % [114]. Ceramic yield up to 90 % in PDCs has been achieved in the recent reports [115, 116]. The ceramic yield of a

preceramic polymer is defined by the following equation (2. 1):

$$\alpha_c = \frac{mass_{pyrolyzed\ ceramic}}{mass_{preceramic\ polymer}} \quad (2. 1)$$

where $mass_{pyrolyzed\ ceramic}$ is the mass of the pyrolyzed ceramic and $mass_{preceramic\ polymer}$ is the initial mass of the preceramic polymer. There are several ways to consider when designing polymer precursors with higher ceramic yield, such as elemental composition [115, 117] and thermal stability [118, 119] of the preceramic polymer, crosslinking [120-122], filler [123, 124] and structures (branched, ring and liner) [86, 125, 126] in the backbone, detailed information can be found in the cited literatures.

2.1.4 Polymer derived ceramic nanocomposites (PDC-NCs)

In recent years, ceramic nanocomposites, consisting of more than one Gibbsian phase and one of them being nanoscaled (less than 100 nm) [127-129], have attracted great attention due to the enhancement in their properties, such as mechanical, electrical and optical properties [9, 106, 130, 131]. Various methods have been developed to prepare ceramic nanocomposites, which can be classified into three categories according to the state of the raw materials: (1) Gas-phase (e.g., sputtering methods [132] and chemical vapor deposition [133]); (2) liquid-state method is the most widely used, mainly including sol-gel processes [134], polymer-derived ceramic route [127], intercalation techniques [135], spray conversion [136], combustion synthesis [137]; (3) solid-state process (e.g., mechanical alloying [138]). The present work will focus on polymer-derived ceramic nanocomposites.

PDC route relying on the pyrolytic conversion of polymeric precursors has been proven to be the most suitable route for the preparation of ceramic nanocomposites [127]. Different methods have been used to synthesize the PDC-NCs, including the chemical modification of the polymer with the metal-containing complex (namely single-source-precursor method), modification of a suitable monomer or blending of polymer with the metal/metal complex [139]. Single-source-precursor route is one of the most attractive methods for the synthesis of PDC-NCs due to its ability to design preceramic polymer at the molecular level. The amorphous single-phase ceramics can be prepared by preliminary pyrolysis at relatively low temperatures (ca. 1200 °C). Subsequently, ceramic nanocomposites with desired phase compositions, microstructures and extraordinary properties could be obtained by heat-treatment at higher temperatures (> 1300 °C). Therefore, PDC-NCs synthesized by single-source-precursor route have been extensively studied and reported for structural and functional applications in the last decades [51, 127].

One example for structural application is the SiC/HfC_xN_{1-x}/C ceramic nanocomposite, which is prepared upon pyrolysis and subsequent SPS sintering of the single-source precursor (SSP) synthesized by chemical reaction between a commercially available allylhydridopolycarbosilane (SMP10, Starfire System Inc, USA) and a tetrakis(diethylamido)hafnium(IV) (TDEAH, Sigma-Aldrich, Germany) [140].

The results show that the hardness (29 ± 4 GPa), Young's modulus (381 ± 29 GPa) and flexural strength (320 ± 25 MPa) of the SiC/HfC_xN_{1-x}/C monolith are remarkably increased due to the incorporation of HfC_xN_{1-x} into the SiC matrix. Another example is the SiHf(B)CN-based ceramic nanocomposites prepared by SiHfCN-/SiHfBCN-SSP and SPS [43]. Besides improving the hardness and elastic modulus of SiHfCN (26.8 and 367 GPa) and SiHfBCN (24.6 GP and 284 GPa), the investigation of the oxidation revealed that the parabolic oxidation rates of SiHfCN ceramic nanocomposite were comparable to those of ultra-high temperature ceramics (e.g. HfC-20 vol% SiC). Moreover, Al-contained Si₃N₄-SiC ceramic nanocomposites fabricated through single-source-precursor route and subsequent spark plasma sintering technique exhibit an excellent high-temperature stability (1350 °C) in both oxidative and corrosive environment [141]. These investigations indicate the enormous potential of the ceramic nanocomposite for high-temperature structural applications in harsh environments.

The functional applications of the polymer-derived ceramic nanocomposites are involved in numerous fields, including but not limited to batteries, electrochemistry, electromagnetic and other emerging areas. For example, a SiOC/Sn ceramic nanocomposite anode synthesized by chemical modification of polysiloxane (RD-684a) with tin(II)acetate and subsequent pyrolysis at 1000 °C exhibits outstanding cycling stability for Lithium-ion batteries [142]. A novel SiC/C/Mo_{3+2x}Si₃C_{0.6} ($x = 0.9 - 0.764$) ceramic nanocomposite used for hydrogen evolution reaction (HER) with excellent electrocatalytic performance is developed upon pyrolysis and subsequent annealing of the single-source precursors synthesized by the chemical reaction of allylhydridopolycarbosilane with MoO₂(acac)₂ [143]. MWCNTs/SiC nanocrystals/amorphous SiOC ceramic nanocomposites with excellent microwave-absorbing property was prepared by pyrolysis of iron acetylacetonate (Fe(acac)₃) modified polymethylsilsesquioxane (PMS) [144]. Moreover, the functional applications of the PDC-NCs used for sensors [145], biomedical applications [146], photocatalysts [147] as well as supercapacitors [148] have been reported as well.

2.1.5 Advantages and disadvantages of PDCs

The PDC route involves the transformation of an inorganic/organic polymer → an amorphous solid → a crystalline ceramic, therefore, there are several advantages in comparison to the powder-based route:

- Polymer shaping techniques (e.g. coating, injection molding, melt spinning, extrusion and polymer infiltration and pyrolysis) can be applied for PDCs due to the polymer properties of preceramic precursor. This provides the possibility to prepare complex shapes and shapes which are difficult to achieve by traditional powder-based route, such as layers, fibers and ceramic matrix composites [139, 149].
- The ability to fine-tune surface characteristics, pore structure/size and density of the ceramic system are arguably the most distinctive advantages compared to traditional ceramic processing technologies, which can be controlled by degree of crosslinking and pyrolysis (crosslinking

agents, thermal, UV etc.), foaming agents (for porous materials), mixing of polymeric precursors, dopants (for multicomponent ceramic materials) [28, 113, 139].

- Ceramic products combining ceramic-like properties with polymer-like nanostructure can be prepared by adjusting the degree of decomposition during polymer-to-ceramic conversion [28, 149, 150].
- Ternary or quaternary ceramics such as SiCN, SiOC, SiBCN and SiHfBCN can only be produced by polymer-derived ceramic route. The reason is that carbon and nitrogen/oxygen cannot dissolve in binary Si₃N₄ and SiC ceramics. Moreover, the diffusion coefficient of boron and metal in SiC and Si₃N₄ are low, therefore, even well-mixed nanopowders cannot achieve the ideal result due to the aggregation of nanoparticles.
- Polymer-derived covalent ceramics generally exhibit improved thermo-mechanical properties with respect to crystallization, phase separation, creep and oxidation up to 1500 °C [104, 151, 152].
- Additive-free sintering. Sintering additives which are usually used to increase the density of sintered ceramics in the conventional powder-based route may limit their technical applications due to the contamination by decomposition products of additives.
- The low synthesis temperature of 1100 °C to 1300 °C for PDCs is of economic interest [112].

There are many other advantages that can be found in the following literature [53, 54, 95, 113, 127, 149, 153-160].

In spite of the such attractive advantages of PDC route, there are also some difficulties in the preparation process. The main disadvantage of PDC route is related to the pore formation and the large volumetric shrinkage (10 – 35%) due to the off-gassing of organic side groups that occurs between polymer precursors and final ceramic products during crosslinking and pyrolysis [161, 162], which leads to large density change and makes production of near-net-shape components difficult. Another disadvantage is the high costs of polymer precursors and more complicated handling environments because most of them are temperature and moisture sensitive [28]. Therefore, PDCs are often used in special fields, in which the conventional powder route cannot achieve satisfactory results.

2.2 Silicon nitride

2.2.1 Crystal structure of silicon nitride

Si₃N₄ exists in three different crystallographic structures including α , β and γ . α -Si₃N₄ and β -Si₃N₄ can be prepared by conventional sintering techniques under ordinary pressure condition, which play a great role in the practical applications of advanced structural ceramics. γ -Si₃N₄ synthesized under extremely

high pressure has no practical use yet, but it has potential to be used as a super hard material due to its high hardness (ca. 43 GPa) [1].

2.2.1.1 α -Si₃N₄ and β -Si₃N₄

The well-known α - and β -Si₃N₄ have hexagonal lattice with the same chemical compositions (3:4 stoichiometry of Si:N) and similar densities (ca. 3.2 g·cm⁻³). The corner-sharing SiN₄ tetrahedron (Figure 2. 6a and b) is the basic unit of α - and β -Si₃N₄, in which each N atom is shared by a further three tetrahedra and the Si atom is located at the center of the tetrahedron. The different arrangement of the Si–N layers results in the structural difference between α - and β -Si₃N₄. As shown in Figures 6d and 6e, the α -Si₃N₄ structure is composed of the basal planes in the order of ABCDABCD..., while β -Si₃N₄ is constructed of a periodic stacking structure of ABAB. The AB layer is the same in the α - and β -Si₃N₄, and the CD layer in α -Si₃N₄ correlates with the AB layer of β -Si₃N₄ through the c-glide plane. The unit cell of β -Si₃N₄ is consisted of Si₆N₈, which belongs to space group P63/m. While the unit cell of α -Si₃N₄ has a composition of Si₁₂N₁₆ due to occupying the double c-axis dimension (space group P31c). The detailed crystallographic data of Si₃N₄ is listed in Table 2. 2 [1].

The calculation from first principles shows that β -Si₃N₄ is more stable than α -Si₃N₄ in the temperature range from 0 to 1800 °C [163]. This indicates that α -Si₃N₄ is a metastable phase under ordinary pressure, rather than a simple low-temperature phase. Usually, α -Si₃N₄ will be transformed to β -Si₃N₄ at around 1500 °C, the transformation is reconstructive process via either volatilisation/condensation or solution/reprecipitation processes, but it is irreversible. Interestingly, the transformation of α -Si₃N₄ to β -Si₃N₄ cannot be achieved simply by prolonged annealing at 1800 °C [164], its transformation is impurity controlled, such as oxygen. The entire process of the α - to β -Si₃N₄ phase transformation is usually divided into nucleation of β -Si₃N₄ in an α -rich matrix, transformation from α to β phase, and rod-like grain growth of β -Si₃N₄. The dissolution of α -Si₃N₄ into boundary liquid and reprecipitation on β -Si₃N₄ grains is the critical step in the process of reconstructive transformation. The intertwined structure of the fibrous β -Si₃N₄ grains plays a great role in the high strength and toughness of Si₃N₄-based materials.

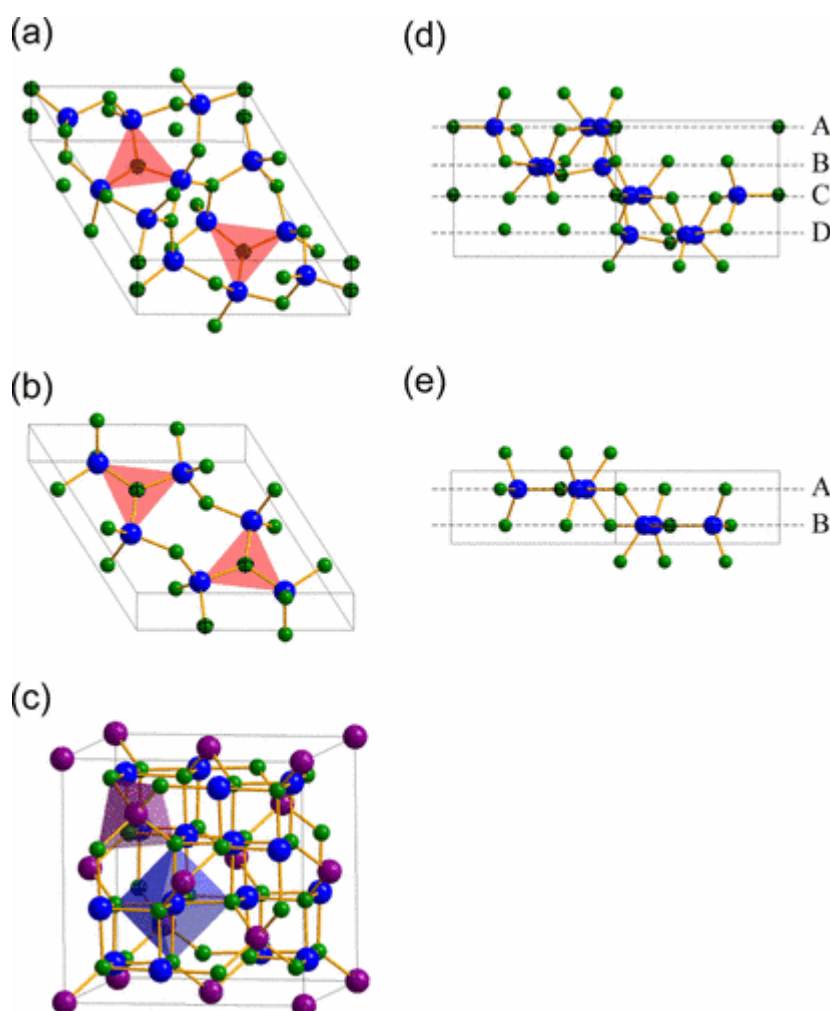


Figure 2. 6 Crystal structures of (a) α - Si_3N_4 , (b) β - Si_3N_4 and (c) γ - Si_3N_4 and viewing (d) α - Si_3N_4 , (e) β - Si_3N_4 from (1120) direction. Blue and green spheres are Si and N atoms, respectively. In the unit cell of α - Si_3N_4 and β - Si_3N_4 , trigonal coordination of N–Si₃ parallel to the basal plane is exhibited by red triangles. In the unit cell of γ - Si_3N_4 , tetrahedral coordination of Si atoms is shown by purple. Tetrahedral and octahedral coordination are shown by purple and blue polyhedra, respectively. Dashed lines in (d) and (e) represent stacking layers repetition in the direction of c axis [163].

2.2.1.2 γ - Si_3N_4

γ - Si_3N_4 was first synthesized under high pressure and high temperature (HPHT) by Zerr and Riedel in 1999, which is a third polymorph of Si_3N_4 with a cubic crystallographic structure [1]. As shown in Figure 6c, nitrogen atoms are arranged in a face-centered cubic crystal structure, while silicon atoms have two sub lattice arrangements in the nitrogen cubic lattice. One third of the silicon atoms are fourfold coordinated by nitrogen atoms and two thirds are sixfold coordinated by nitrogen atoms. The increase in the coordination number of Si in γ - Si_3N_4 ($3.93 \pm 0.12 \text{ g}\cdot\text{cm}^{-3}$) results in a significantly tighter atomic packing and a 26 % increase in density as compared to that of α - Si_3N_4 ($3.18 \text{ g}\cdot\text{cm}^{-3}$) and β - Si_3N_4 (3.20

$\text{g}\cdot\text{cm}^{-3}$), which consequently results in higher elastic modulus and hardness compared to the low-pressure hexagonal phases [1, 2, 165-167]. $\gamma\text{-Si}_3\text{N}_4$ is often referred to as a superhard candidate (43 GPa) after diamond and cubic boron nitride (c-BN) [25]. In addition, the high-temperature stability of $\gamma\text{-Si}_3\text{N}_4$ is better than that of the diamond and c-BN, and therefore is a potential candidate for technological application under very harsh conditions (e.g. drill head, abrasive and cutting tools).

Table 2. 2 Crystallographic data of Si_3N_4 [1, 163, 168].

Polymorph		$\alpha\text{-Si}_3\text{N}_4$	$\beta\text{-Si}_3\text{N}_4$	$\gamma\text{-Si}_3\text{N}_4$
Space group		P31c	P6 ₃ /m	Fd3m
Lattice parameter	$a\approx b$ (nm)	0.776	0.761	
	c (nm)	0.562	0.291	0.774
Theoretical density ($\text{g}\cdot\text{cm}^{-3}$)		3.18	3.20	3.93

2.2.2 Fabrication and mechanical properties of Si_3N_4

Since the middle of 20th century, silicon nitride (Si_3N_4) as one of the most promising advanced ceramics has attracted ever-increasingly attention due to its potential application in high-temperature structural components. The widespread interest stems from its desirable physical and mechanical properties, such as low density (approximately 40% of the density of high temperature super alloys), low coefficient of thermal and friction expansion, high strength and wear resistance, good resistance to oxidation and corrosive environments [5, 7, 8, 169, 170]. This combination of properties (Table 2. 3) makes it a great candidate over other high-temperature materials for potential engineering applications in gas turbines, engine parts, bearings, dental drills and cutting tools. However, the preparation of dense Si_3N_4 ceramic is very difficult because Si_3N_4 is a highly covalent compound and its bulk diffusion is too low to be consolidated [7, 171]. In order to manufacture Si_3N_4 ceramics for practical applications in harsh environments, shaping and densification of Si_3N_4 ceramics is critical. In this chapter, the fabrication and properties of Si_3N_4 ceramics are introduced and the issues in shaping and densification of Si_3N_4 ceramic are also discussed with respect to the latest research developments.

Table 2. 3 Typical properties of structural ceramics (HIP: Hot Isostatic Press; PS: Pressureless Sintering; RS: Reaction Sintering; HP: Hot Press) [3, 6, 172-174].

Materials	Sintering methods	Density (g cm ⁻³)	Flexural strength (MPa)		Thermal Expansion (10 ⁻⁶ °C ⁻¹)
			RT	HT (°C)	
Si ₃ N ₄	HPS	3.1 – 3.4	450 – 1200	~600 (1400)	3.0 – 3.9
Si ₃ N ₄	PS	2.8 – 3.4	275 – 1000	~800 (1400)	~3.5
Si ₃ N ₄	RS	2.0 – 2.8	~	~400 (1400)	~3.2
β-SiAlON	PS	2.8 – 3.3	485	~275 (1375)	2.5 – 3.1
SiC	HP	3.2 – 3.3	655	~520 (1375)	4.5
SiC	PS	3.1 – 3.2	700	~700 (600)	4.8
SiC	RB	2.7 – 2.8	300	~300 (600)	4.4
Al ₄ SiC ₄	PS	2.89	297.1	449.7 (1300)	6.2
C/SiC-SiBC	PS	2.2	276	440 (1200)	4.5 – 4.8
ZrB ₂ /SiC	HP	5.24	546	460 (1600)	4.5 – 6.8

2.2.2.1 Sintering and densification of α- and β-Si₃N₄

Sintering is a very important step in the ceramic manufacturing and densification process, which is a process governed by atomic diffusion. Atomic bonds are activated by thermal energy and allow particles to rearrange at high temperatures, leading to consolidation in loosely packed bodies through mass transport mechanisms. In general, mass transport occurs by a variety of mechanism, such as diffusion mechanism and viscous flow. The supplement of thermal energy, diffusion or viscous flow are the primary mechanisms, depending on the material to be densified. The sintering process and physical changes are shown in Table 2. 4.

Si₃N₄ is a highly covalently bonded compound with very low diffusivity. The diffusion coefficients of nitrogen atoms and silicon atoms in the volume or at the grain boundaries of Si₃N₄ are extremely low, which are $D_N \approx 6.8 \times 10^{-10} \text{ m}^2 \cdot \text{S}^{-1}$ and $D_{Si} \approx 0.45 \times 10^{-9} \text{ m}^2 \cdot \text{S}^{-1}$, respectively [5]. As aforementioned sintering mechanisms, the sintering densification is a mass transport process via volume or grain boundary diffusion. The higher sintering temperature is required to prepare a highly dense material because diffusion is a thermally activated process. Densification of Si₃N₄ by self-diffusivity

starts at extremely high temperatures ($>1850\text{ }^{\circ}\text{C}$), however, decomposition of Si_3N_4 already starts at around $1650\text{ }^{\circ}\text{C}$ [5, 171]. Therefore, the preparation of fully dense Si_3N_4 is very difficult by classical solid-state sintering method. To date, liquid phase sintering using sintering additives and many different sintering techniques have been developed to fabricate dense Si_3N_4 .

Table 2. 4 General stage during solid phase sintering.

Initial stage	Intermediate stage	Final stage
Rearrangement of particles	Neck growth	Grain growth
	Grain growth	Discontinuous pore phase
Neck formation	Shrinkage	Grain boundary
	Continuous pore phase	Pores elimination

The densification mechanism of liquid phase sintering of Si_3N_4 ceramics has been reported in detail by the Kingery [175, 176], German [177], Petzow [178] and Ziegler [4]. which can be explained in three steps. As can be seen from Fig. 2. 7, the first stage is particle rearrangement, which starts immediately after the formation of liquid phase by the reaction of the sintering additive and the phases containing oxygen, SiO_2 or oxynitride layers present on the particle surface of Si_3N_4 powder. The rapid densification takes place due to the capillary force of the wetting liquid on the Si_3N_4 particles, and ca. 65% relative density can be achieved by at this stage. The extent of the densification is influenced by many factors, such as the morphologies (sizes and shape) of the particles, the level of external pressure and the amount and viscosity of the liquid phase. The particle rearrangement process ceases because of the formation of the particle bridges, and the second stage (solution-precipitation) begins to dominate the densification process.

The driving forces of the solution-precipitation process are the higher solubility at the points of the particle contact and the difference in the chemical potentials between small and large particles, resulting in dissolution of small particles and precipitation on the surface of large particles [179]. The small α - Si_3N_4 particles are dissolved into the liquid phase during the solution-precipitation process, in which the diffusion of silicon and nitrogen atoms and the breaking and reforming of Si-N bonds occur. This instability of the α - Si_3N_4 leads to an improvement of the solution and thus an increase in densification. This process also involves the phase transformation of α - and β - Si_3N_4 due to the thermodynamically unstable at this condition (e.g. $1400 \sim 1600\text{ }^{\circ}\text{C}$ at $10 \sim 101\text{ kPa N}_2$ pressure). Moreover, the precipitation and phase transformation are affected by the phase composition of the starting material. If the starting material contains a large number of β - Si_3N_4 grains, the fine β - Si_3N_4 particles will start to dissolve accompanied by the presence of solution, resulting in continuous precipitation on the surface of β - Si_3N_4

nuclei and the formation of the equiaxial β - Si_3N_4 grains. If there is a low concentration of β - Si_3N_4 nuclei in the starting material, the supersaturated liquid phase is created locally, which lead to a homogeneous nucleation and the formation of idiomorphic rod-like β - Si_3N_4 . In addition, β - Si_3N_4 grains can also be formed in situ under the supersaturation of nitrogen and silicon atoms in the liquid phase. However, due to the different diffusion rates of Si and N atoms in liquids of different viscosities, therefore, the different sintering additives will lead to the formation of various morphologies of β - Si_3N_4 , hexagonal equiaxed β - Si_3N_4 grains by Al_2O_3 and elongated β -grain by Y_2O_3 . The above process can be accelerated by applying external pressure, such as hot-pressing, hot-isostatic pressing or spark plasma sintering, which is helpful for the densification of Si_3N_4 and the enhancement of the mechanical properties.

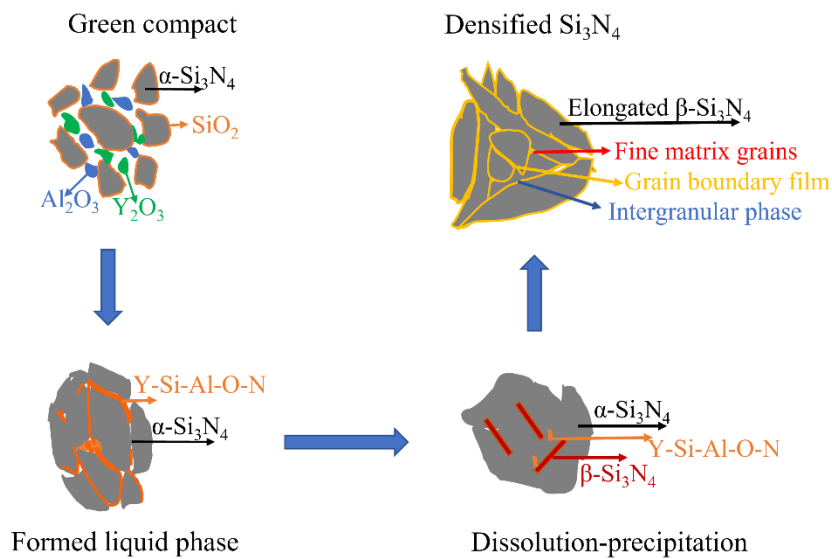


Figure 2. 7 Schematic diagram of the densification mechanism of Si_3N_4 ceramics using Al_2O_3 and Y_2O_3 as sintering additives.

The final stage of liquid phase sintering is termed coalescence, which is dominated by solid state sintering. In this stage, although the microstructural coarsening continues through diffusion, the further rearrangement and densification are hindered because of the rigid Si_3N_4 solid skeleton. In this case, the residual pores will expand suddenly if there is some entrained gas, resulting in swelling and a decrease in densification. During cooling, the liquid silicate glass solidifies to amorphous or partially crystalline phases, which are situated either at the grain boundaries in thin layers or at triple junctions. The thickness of the grain boundary layer depends on the types of sintering additives rather than on the amount of liquid phase, the increase in the amount of sintering additive leads only to an increase in the triple point volume [180]. However, their high temperature applications are hindered because their intergranular glassy phase softens at high temperatures causing grain boundary sliding leading to poor creep and strength properties [7, 169, 181]. Therefore, the fabrication of dense bulk Si_3N_4 ceramics without sintering additives becomes of technological interest for the application of Si_3N_4 at elevated temperatures and under harsh conditions.

2.2.2.2 Synthesis of γ - Si_3N_4

γ - Si_3N_4 first reported by Zerr and Riedel in 1999 [1], was synthesized using laser heating techniques in diamond anvil cells (LH-DACs) at pressures above 15 GPa and temperatures over 1873 K. HPHT conditions are essential for the preparation of γ - Si_3N_4 , and three methods have been developed so far: i) The first method is LH-DACs as first reported for the synthesis of γ - Si_3N_4 [1, 182], but the size of synthesized samples is usually in the order of 20 – 50 nm, which limits their characterizations and applications. In order to investigate their properties, e.g. magnetic properties, electrical conductivity, thermal and mechanical properties, the synthesis of large samples is required. ii) Therefore, the second method, the multi-anvil press, was developed by Bridgman [183, 184], this method enables the synthesis of samples with dimensions up to millimeters [25, 185]. iii) γ - Si_3N_4 can also be prepared by shock wave synthesis (above 20 GPa) using α - or β - Si_3N_4 powder and catalyst (copper powder) [27, 186-188], which inevitably leads to the presence of impurities due to the use of the catalyst, and the yield is also limited to ca. 80%. Therefore, a multi-anvil device is used to synthesize γ - Si_3N_4 -based material in this work.

2.2.2.3 Mechanical properties of Si_3N_4

2.2.2.3.1 Mechanical properties of α/β - Si_3N_4

The mechanical properties of Si_3N_4 ceramics are affected by various factors such as the compositions, presence of pores, cracks and inclusions. Among these factors, porosity has a significant effect on mechanical properties. As aforementioned, dense Si_3N_4 ceramics can only be obtained by indirect methods, such as sintering additives and external pressures, because of its low self-diffusivity and decomposition temperature. Therefore, there are four typical types of Si_3N_4 ceramics according to preparation methods: i) Reaction bonded Si_3N_4 (RBSN); ii) Hot pressed Si_3N_4 (HPSN); iii) Sintered Si_3N_4 (SSN); iv) Sintered reaction-bonded Si_3N_4 (SRBSN), which affects their resultant properties and applications. RBSN is produced by direct nitridation of compacted silicon powder at about 1450 °C, and the obtained product always contains porosity (ca. $\geq 10\%$) [4, 189, 190]. Besides, RBSN ceramics inevitably exist structural defects because of unreacted Si or melting Si or silicides in Si_3N_4 matrix. Therefore, the mechanical properties of the RBSN are inferior to those of the other types of Si_3N_4 , as shown in the Table 2. 5. The advantage of RBSN is that it can produce complex shapes using various forming methods with low cost, such as injection molding, slip casting, isostatic pressing, die pressing. In order to prepare dense Si_3N_4 to utilize some of its outstanding properties, HPSN was developed in the 1960s and the first HPSN was prepared in 1961 using a small amount of MgO as an additive [191]. The hot-pressed Si_3N_4 pellet is almost fully dense with excellent mechanical properties (Table 2. 5). SSN is one of methods to prepare dense Si_3N_4 ceramics, in which Si_3N_4 is densified by pressureless sintering under N_2 atmosphere at around 1750 °C with the help of various sintering additives (Y_2O_3 , Al_2O_3 , MgO, Li_2O et al.) [192, 193]. The mechanical properties of SSN are between those of HPSN and RBSN. SRBSN is developed on the basis of RBSN to reduce the porosity of the Si_3N_4 ceramic, thereby

improving their mechanical properties. This is achieved by the addition of sintering additives, which allows the RBSN to be further sintered after the reaction-bonding stage [194].

Table 2. 5 Physical and mechanical properties of Si₃N₄ [195-200].

Properties	RBSN	HPSN (YF ₃ /MgO)	SSN (Y ₂ O ₃)	SRBSN (Y ₂ O ₃ /Al ₂ O ₃)
Density (g/cm ³)	2.8	3.2	3.2	3.26
Porosity (%)	77	1.5	2.93	2.0
Hardness (GPa)	~8	~14.8	~13	~14
Fracture toughness (MPa m ^{1/2})	2.8	6.3	~6.7	~7.0
Flexural Strength (MPa)	288	760	665~1000	~800
Young's modulus, E(GPa)	210	300	275	~

2.2.2.3.2 Mechanical properties of γ -Si₃N₄

First-principle calculations have shown that the shear and bulk modulus of γ -Si₃N₄ are as high as 261 GPa and 312 GPa, respectively [201]. A shear modulus of 148 GPa and bulk modulus of 290 GPa were obtained by experiments later [202]. The hardness of γ -Si₃N₄ was estimated to be between 30 and 43 GPa at the same time [202]. These mechanical properties are much higher than those of α - and β -Si₃N₄, and comparable to those of the hardest known HPHT SiO₂-stishovite, making it become the third hardest material besides diamond and cubic BN. In addition, γ -Si₃N₄ shows the dominant direct electronic band gap values that can span the whole visible wavelength region, and the value of the electronic band gap and exciton binding energy are up to 4.8 ± 0.2 eV and 333 meV, respectively, indicating that γ -Si₃N₄ is a prospective candidate for optoelectronic devices with chemical and mechanical stabilities, such as lighting applications [203].

2.2.2.3.3 Factors affecting mechanical properties

The hardness of Si₃N₄-based ceramics is mainly related to the phase composition because hardness is an intrinsic property of the material. As shown in Table 2. 6, the hardness of γ -Si₃N₄ is up to 30 GPa, and the hardness of α -Si₃N₄ and α -sialon is ca. 40% higher than those of β -Si₃N₄ and β -sialon [204]. In addition, nanostructuring of Si₃N₄-based ceramics is a crucial way to keep its hardness by means of the Hall-Petch effect: the hardness increases with decreasing grain size [205, 206].

The fracture toughness of Si₃N₄-based ceramics depends not only on the composition of grain

boundary/amorphous phase, but also on morphologies and grain sizes. There are also two fracture models for Si₃N₄ ceramic system, transgranular and intergranular. In general, transgranular fracture and intergranular fracture coexist, and which one dominates depends on the strength of the intergranular phase and Si₃N₄ grains. High fracture toughness is associated with the interlocking bimodal microstructures of fine-grained matrix and large elongated β-Si₃N₄, which is similar to the toughening mechanisms in whisker-reinforced composites, such as grain bridging, crack deflection, crack branching and pull-out [169, 207]. However, these toughening mechanisms are only effective when the fracture mode is intergranular. In addition, the weaker grain boundary can increase the fracture toughness of the material. The strength of the grain-boundary phase is related to the local residual stresses [208]. Therefore, the ratio of intergranular fracture can be adjusted on basis of the residual stresses. The grain-boundary phase is under tensile stress when the thermal expansion coefficient of the Si₃N₄ grains is lower than that of the grain-boundary phase [208], which lead to a higher fracture toughness.

Table 2. 6 Morphologies and mechanical properties of Si₃N₄-based ceramics [25, 209].

Materials	Morphology	Mechanical properties	
		Hardness (GPa)	K _{IC} (MPa·m ^{1/2})
α-Si ₃ N ₄	Equiaxed	20 ± 5	2.0 ± 0.51
β-Si ₃ N ₄	Elongated	15 ± 1	~6.0
α-sialon	Equiaxed	18 – 21	3.0 – 5.5
β-sialon	Elongated	15 – 17	5.0 – 7.0
γ-Si ₃ N ₄	Elongated	36 ± 8	3.0 – 4.5

2.2.3 Si₃N₄ ceramics with reinforcement phase

Si₃N₄ ceramic is undoubtedly one of the most important nonoxide structural ceramic materials that meets the requirements of mechanical, electronic and microwave-transparent applications because of its excellent properties, such as chemical stability, high mechanical strength and fracture toughness, wear resistance, high modulus of elasticity, dielectric properties, and low thermal expansion [5-7]. However, long-term structural and functional properties of Si₃N₄ are limited by its inherent brittleness, creep and oxidation resistance. In order to improve the long-term reliability of Si₃N₄ ceramics under extreme conditions, various Si₃N₄-based ceramic composite systems, such as whisker-, fibre- or particulate-reinforced Si₃N₄, have been developed in the past decades [5, 169, 210-212]. In this Ph.D. work, boron and transition metal (hafnium) as well as in situ formed compounds are used for the reinforcement phase of Si₃N₄-based ceramics. Thus, the introduction here focuses only on the particulate-reinforced Si₃N₄-

based ceramic composites.

Particulate reinforcements have attracted much attention due to their relatively easy processing, and the reinforcement phase not only improves toughness but also other mechanical properties such as hardness, strength and wear resistance [210]. Moreover, the introduction of the conductive phase in Si_3N_4 matrix can decrease the electrical resistivity, which can not only expand the functional applications of Si_3N_4 -based composites but also enable the materials to be manufactured to complex shapes by electrical discharge machining. Many nitrides/carbides of transition metals such as Group IV (Ti, Zr and Hf), Group V (V, Nb and Ta) and Group VI (Cr, Mo, and W), known as ‘metallic ceramics’, were used as reinforcement phase to modify the microstructure of Si_3N_4 [210]. Although they have covalent, ionic and metallic bonds, their conductance is through electrons rather than ions, leading to similar or even higher conductivity than those of the corresponding metals. The chemical compatibility of reinforcements with the Si_3N_4 matrix is to be considered when selecting a compound to prepare particulate-reinforced Si_3N_4 -based ceramics. In general, nitrides have better compatibility with Si_3N_4 than carbides. Furthermore, chemical reactions always occur between Si_3N_4 matrix and most of carbides during the sintering process, which inevitably introduces impurities. For example, Peni et al. reported that a gradient of reaction products, composed of $\text{TiC}_{0.5}\text{N}_{0.5}$ and SiC crystals, were detected in reaction product regions around TiC grains [213]. In contrast, TiN is stable at that temperature, which is also confirmed by the thermal dynamic calculations [214] and other experimental research [215, 216]. Therefore, among these various reinforcement systems, nitrides-reinforced Si_3N_4 have been widely investigated and reported in the last decades.

One example is the investigation of the microstructure and mechanical properties of $\text{TiN}/\text{Si}_3\text{N}_4$ composites. The fracture toughness of the Si_3N_4 matrix improved by 30% with the addition of TiN . This result revealed that TiN particles played an important role in the toughening effects of $\text{TiN}/\text{Si}_3\text{N}_4$ composites, most of the microcracks exhibited transgranular modes and cleaved along preferred directions with large deflection angles [216]. The investigation emphasizes the enormous potential of the nitrides-reinforced Si_3N_4 for structural applications. Another example is the $\text{ZrN}/\text{Si}_3\text{N}_4$ composites prepared by SPS, and the tribological and mechanical properties of the as-obtained materials were investigated [217]. When the ZrN content increased to 84%, the tribological properties of the consolidated $\text{ZrN}/\text{Si}_3\text{N}_4$ composites increased substantially with increasing the ZrN content due to the lubricating capability of ZrN , and the hardness was up to 17 GPa. These results showed that $\text{ZrN}/\text{Si}_3\text{N}_4$ composites can be recommended for use in friction applications under dynamic loads. Moreover, Guo et al. reported the studies of the microstructure and electrical properties of $\text{TiN}/\text{Si}_3\text{N}_4$ composites fabricated by powder processing routes (HP and SPS) [218]. The electrical resistivity of the dense $\text{TiN}/\text{Si}_3\text{N}_4$ materials is significantly lower than that of the pure Si_3N_4 ceramics due to the presence of TiN grain size and crystallized grain boundary phases. Although nitrides-reinforced Si_3N_4 systems have been studied systematically to date, most of them were prepared by the conventional powder-based route.

As aforementioned, advanced ceramics with nanostructures and complex shapes cannot be produced by powder technology, which limits their technical applications. Therefore, it is necessary to explore and develop new methods to prepare Si₃N₄-based ceramic nanocomposites for their structural and functional applications.

2.2.4 Polymer-derived Si₃N₄-based ceramic nanocomposites

Polysilazane and its various derivatives, an organosilicon-based polymer with the general formula [SiR₁R₂-N]_n, are prominent precursors for the fabrication of SiCN or Si₃N₄ ceramics. The synthesis of polysilazane precursors is mostly performed by aminolysis with different primary amines or by ammonolysis reactions of chlorosilanes [219]. The synthesis route reported by Krüger and Rochow in 1964 [220] laid the foundation for the synthesis and application of high-performance polysilazane precursors. Since then, a series of pioneering works have been devoted to the synthesis and optimization of high molecular weight polysilazane, and a number of different synthetic routes for polysilazanes have been developed and reported. Among the most classic and commonly used methods are aminolysis [221, 222], ammonolysis [223, 224], dehydrocoupling [225, 226], hydrazinolysis [227, 228] and ring-opening polymerization [229-231]. Ammonolysis and aminolysis are the major approaches for producing commercially available polysilazanes due to the positive reactivity of chlorosilanes and the low cost of ammonia (amine). The basic synthesis pathway of polysilazanes is shown in Figure 2. 8, Si-N bonds are formed by the reaction of N-H bond with Si-Cl bond. Furthermore, the Si-H/N-H groups of polysilazanes could further react with each other (N-H/Si-H) to enhance the degree of condensation reaction and crosslinking. Furthermore, these Si-H/N-H groups can be used as functional groups for further chemical modification with different organometallic compounds to produce Si₃N₄-based or SiCN-based ceramic composites.

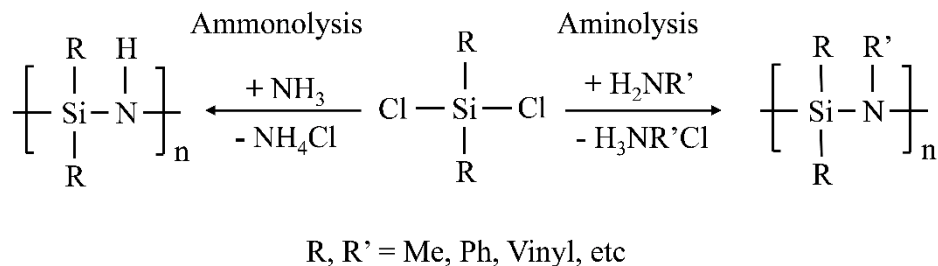


Figure 2. 8 Basic synthesis pathways of polysilazanes via ammonolysis and aminolysis.

Perhydropolysilazane (PHPS) is an ideal precursor for the synthesis of polymer-derived Si₃N₄-based ceramics due to its reactivity, carbon-free Si-N chain and high yield. Nowadays, various Si₃N₄-based ceramic nanocomposites based on the modification of PHPS have been discovered and reported. Iwamoto et al. investigated the crystallization and microstructure evolution of titanium-modified PHPS

precursors [60], where tetrakisdimethylaminotitanium and titanium tetra-isopropoxide TiX_4 [$X=N(CH_3)_2$, $OCH(CH_3)_2$] were used as Ti sources. Ti-modified polymers presented amorphous structure at temperature up to 1400 °C, while the pure PHPS started to crystallize α - Si_3N_4 at 1200 °C. Additionally, TiN particles smaller than 100 nm were observed in the polytitanosilazane-derived Si_3N_4/TiN ceramics made of PHPS and $Ti(N(CH_3)_2)_4$, indicating that this route is suitable to produce TiN nanoparticle-dispersed Si_3N_4 ceramics. Based on this work, in situ controlled growth of TiN in amorphous Si_3N_4 was reported by Bechelany et al [21], in which the final ceramic consisted of 3 – 5 nm TiN nanocrystals dispersed in an amorphous Si_3N_4 matrix and exhibited compositional and nanostructural homogeneity. The resultant TiN ceramic refinement and microstructural uniformity were attributed to the modification of PHPS with $Ti(N(CH_3)_2)_4$ at the atomic level. Furthermore, additive- and crack-free monoliths was prepared by warmpressing attributing to the high degree of crosslinking and low weight loss of the precursors, and the resultant ceramic nanocomposite exhibited hardness value as high as 25.1 GPa. In further work of this research group, the influence of volume fraction of TiN on the high temperature crystallization behavior of polytitanosilazane-derived amorphous SiTiN ceramics was investigated in the temperature range from 1000 to 1700 °C under N_2 atmosphere (Figure 2. 9) [232, 233]. The results revealed that TiN firstly nucleated in amorphous SiTiN ceramics at 1400 °C for all the resultant SiTiN ceramics. However, the onset of the Si_3N_4 crystallization temperature and TiN crystallite growth are strongly dependent on the molar Si:Ti ratio fixed in the polytitanosilazane level, which are shifted to higher temperatures (> 1400 °C) with increasing the volume fraction of TiN in the amorphous Si_3N_4 matrix.

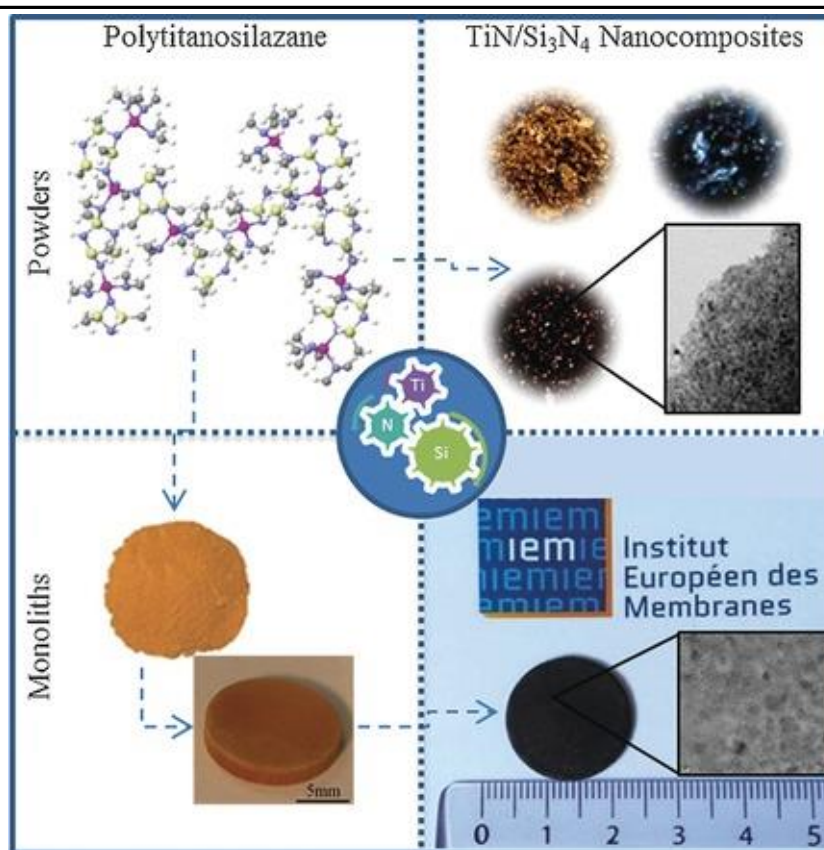


Figure 2. 9 Schematic diagram for the preparation of TiN/Si₃N₄ nanocomposite powder and bulk samples from polytitanosilazanes [232].

A series of pioneering work for the fabrication of Si₃N₄-based ceramic nanocomposites using another transition metal to chemically modify PHPS is carried out in Prof. Riedel's group. A novel SiHfN ceramic was prepared via ammonolysis of a single-source precursor which was synthesized by the chemical reaction of PHPS with tetrakis(dimethylamido) hafnium(IV) (TDMAH) [19, 234]. The investigation of its high-temperature behavior concerning crystallization and phase separation revealed that the incorporation of hafnium in silicon nitride suppresses the crystallization of pure PHPS and phase transformation of α -Si₃N₄ to β -Si₃N₄. In further work, amorphous bulk SiHfN ceramic with prospective mechanical properties was prepared via a resource-efficient low-temperature molding method (warm-pressing). Hardness and Young's modulus show a significant improvement compared to most of the reported amorphous and polycrystalline Si₃N₄-based ceramics. Furthermore, a C/SiFeN(O)-based ceramic paper decorated with in situ generated hierarchical 1D nanostructures was fabricated upon heat treatment of a cellulose-base paper modified with a Fe-containing precursor synthesized from PHPS and iron(II) acetylacetonate (Fe(acac)₂) [235]. The SiFeN(O) ceramic with a PHPS: Fe(acac)₂ weight ratio of 95:5 exhibits outstanding resistance against crystallization up to 1400 °C. Additionally, vanadium-containing PHPS-based single-source precursors were prepared upon chemical modification of PHPS with various amounts of vanadium(IV) oxide acetylacetonate (VO(acac)₂) [236]. The SiVN(O) ceramic obtained by single-source precursor pyrolysis under ammonia at 1000 °C showed ceramic

nanocomposites consisting of VN nanograins (ca. 1 – 5 nm) embedded in an amorphous SiN(O)-based matrix. The comparison between SiVN(O) and the aforementioned similar SiHfN/SiTiN shows that the type of metal introduced into amorphous Si₃N₄ strongly affects its crystallization kinetics. These investigations provide a guideline for the future design and fabrication of further complex amorphous/ternary/multinary Si₃N₄-based ceramic composites based on the system SiMN with M = metal or transition metal (i.e., Fe, V, Hf, Zr, Ta).

2.3 Scope of the work

The above introduction and literature review indicate the possibility for the preparation of Si₃N₄-based ceramic composites without sintering aids by the PDCs route in combination with warm-pressing and the HPHT method. In addition, these methods also show obvious advantages in the fabrication of ceramic nanocomposites with intriguing mechanical and functional properties. Therefore, the main objective of this Ph.D. work is to synthesize Hf/B-containing Si₃N₄-based ceramic nanocomposites, and to explore the effects of preparation conditions (e.g. temperatures, pressures etc.), crystallization process and nanostructures on the mechanical properties and oxidation resistance. Based on the above motivation, the whole Ph.D. thesis is divided into three parts.

- (1) Bulk amorphous SiHfN ceramics were prepared by in situ consolidation of preceramic polymer powders via warm-pressing followed by densification via pressureless ammonolysis and annealing. The critical issues concerning gas evolution and crystallization inducing bloating and cracking were addressed by TGA and SEM. Furthermore, the mechanical properties of the resultant amorphous SiHfN ceramics were evaluated via nanoindentation and Vickers hardness measurements.
- (2) γ -Si₃N₄/Hf₃N₄ ceramic nanocomposite was prepared by single-source-precursor route and HPHT method as well as in-situ energy-dispersive X-ray diffraction (ED-XRD) using synchrotron radiation. The phase evolution of the single-phase amorphous Si-Hf-N precursor under high pressure was assessed by in situ ED-XRD. Moreover, the hardness and fracture toughness of the γ -Si₃N₄/Hf₃N₄ ceramic nanocomposite were also investigated for future industrial applications.
- (3) The single-source-precursor synthesis and polymer-to-ceramic conversion of the B/Hf modified PHPS were characterized by FTIR, XPS and TGA. The influence of boron and hafnium incorporation on the crystallization of SiHfBN ceramics was investigated via XRD and TEM. Finally, the oxidation behavior of bulk Si₃N₄/HfB_xN_{1-x} ceramic nanocomposites was analyzed.

3 Cumulative part of the thesis

Within the cumulative part of this Ph.D. thesis, the major research work reported in publications 1 – 3 are summarized and discussed. The first part (Chapter 3.1) focuses on the preparation and mechanical properties of additive-free amorphous bulk SiHfN ceramics fabricated by *in-situ* consolidation of preceramic polymer powders via warm-pressing. This work provides a new and advanced strategy for the preparation of monolithic amorphous SiHfN ceramics using polymer precursors, which is a major step forward from powder to monolith in practical applications, especially for Si₃N₄-based materials. In Chapter 3.2, a novel high-pressure γ -Si₃N₄/Hf₃N₄ ceramic nanocomposites was prepared by the PDC route and HPHT method as well as *in-situ* ED-XRD using synchrotron radiation. The resultant γ -Si₃N₄/Hf₃N₄ ceramic nanocomposites exhibited a comparable hardness and higher fracture toughness than that of γ -Si₃N₄, which provides a reliable and feasible route for the synthesis of superhard γ -Si₃N₄-based composites for practical applications. Finally, the characterization of single-source-precursor synthesis, polymer-to-ceramic transformation of the B/Hf-modified PHPS as well as crystallization resistance and microstructure of the as-prepared ceramics is conducted carefully in Chapter 3.3. Furthermore, high temperature oxidation behavior of the resultant Si₃N₄/HfB_xN_{1-x} ceramic monoliths was assessed. The works in Chapter 3.1, 3.2 and 3.3 open a new strategy to prepare additive-free polycrystalline Si₃N₄- and amorphous Si₃N₄-based ceramic (nano)composites, which is also a guideline for the future fabrication of further complex ternary and multinary ceramics based on the SiMN system (M = metal or transition metal).

1. **Li W**, Li F, Yu Z, et al. Polymer-derived SiHfN ceramics: from amorphous bulk ceramics with excellent mechanical properties to high temperature resistant ceramic nanocomposites [J]. *Journal of the European Ceramic Society*, 2022, 42(11): 4493-4502.
2. **Li W**, Yu Z, Wiehl L, et al. Hard and Tough Novel High-Pressure γ -Si₃N₄/Hf₃N₄ Ceramic Nanocomposites [J]. *Journal of Advanced Ceramics*, Available online: 08 May 2023.s
3. **Li W**, Du H, Tian C, et al. Single-source-precursor derived bulk Si₃N₄/HfB_xN_{1-x} ceramic nanocomposites with excellent oxidation resistance [J]. *Zeitschrift für anorganische und allgemeine Chemie.*, 2022.
4. Zhan Y, **Li W**, Jiang T, et al. Boron-modified perhydropolysilazane towards facile synthesis of amorphous SiBN ceramic with excellent thermal stability [J]. *Journal of Advanced Ceramics*, 2022: 11(7): 1104-1116.

3.1 Polymer-derived SiHfN ceramics: from amorphous bulk ceramics to high temperature resistant ceramic nanocomposites

The content of this Chapter is published in:

1. **Li W**, Li F, Yu Z, et al. Polymer-derived SiHfN ceramics: From amorphous bulk ceramics with excellent mechanical properties to high temperature resistant ceramic nanocomposites[J]. *Journal of the European Ceramic Society*, 2022, 42(11): 4493-4502.

This chapter presents an advanced and resource-efficient low-temperature molding strategy for preparing bulk amorphous SiHfN ceramic with excellent mechanical properties, i.e., *in-situ* consolidation of preceramic polymer powders via warm-pressing. The obtained sample exhibits open porosity as low as 2.35% via subsequent pressureless ammonolysis and annealing of green body. However, additional closed pores are present according to the ratio of skeletal density and true density. The critical reasons concerning the formation of closed pores were carefully discussed based on cross-linking reaction and springback mechanism. Furthermore, the mechanical properties of the resultant bulk amorphous SiHfN ceramic show a significant improvement in comparison to most of the reported amorphous and polycrystalline Si₃N₄-based ceramics. In addition, the high-temperature microstructural evolution reveals that the introduction of hafnium into Si₃N₄ suppresses the transformation from α -Si₃N₄ to β -Si₃N₄ at high temperatures (1700 °C) and improves their high-temperature stability.

3.1.1 Experimental procedures

3.1.1.1 Synthesis and ammonolysis of the SiHfN precursors

The single-source precursor for the preparation of the SiHfN ceramics was synthesized using commercially available perhydropolysilazane (PHPS, 20 wt.% solution in di-n-butyl ether, AZ Electronic Materials GmbH, Germany) and tetrakis(dimethylamido) hafnium(IV) (TDMAH, $\geq 99.99\%$, Sigma-Aldrich, Germany). Anhydrous toluene (Merck, Germany) was used as reaction solvent. All manipulations of the chemical synthesis were performed under argon atmosphere (argon-filled Glovebox and Schlenk technique) to keep inert conditions. The chemical modification of PHPS with different hafnium contents was reported in our previous work [19], in which the synthesis process was carried out through the following steps: 1 g TDMAH was dissolved in 5 mL anhydrous toluene, and then the resulting brown and transparent solution was added dropwise into a solution of 11.25 g PHPS (2.3 g pure PHPS) under stirring at room temperature. The reaction mixture was constantly stirred with flowing argon for 6 h at ambient temperature, and a milky white gel-like product was obtained. Subsequently, the solvent and low molecular weight by-products were removed in a vacuum (10^{-2} mbar) at 50 °C for 5 h. The as-obtained SiHfN precursor was ground and sieved in an Ar-filled glovebox to avoid contact with air or moisture. The sieved fine powders were introduced (ca. 1.0 g) into the pressing

mold and then heated to 110 °C for 1 h in the warm press at a pressure range of 80 – 200 MPa. Pellets with the typical dimension of approximately \varnothing 20 mm were prepared after slowly deloading during cooling to RT. Afterwards, the green bodies were transferred into a horizontal Schlenk tube under the protection of inert atmosphere in a glovebox. The tube was pumped three times under vacuum and refilled with high-purity ammonia (NH_3 >99.98 %, Air Liquide, $\text{H}_2\text{O} \leq 200$ wt. ppm) before heating. The as-obtained pieces were ammonolyzed at 1000 °C for 2 h at a heating rate of 30 °C/h under a constant flow of ammonia (1.5 L/h), and then cooled down to RT at 60 °C/h. In order to increase the density, ammonolyzed samples were subsequently annealed at 1300 °C, 1500 °C, and 1700 °C for 2 h at a heating rate of 60 °C/h under a constant flow of N_2 in a high-temperature graphite furnace (GT&AT, Advanced Technology, USA), and then cooled down to RT at 100 °C/h. These three groups are denoted as SiHfN-13, SiHfN-15, and SiHfN-17, respectively.

3.1.1.2 Characterization

The phase compositions of the ceramic samples were determined with a STADI P powder diffractometer (STOE & Cie GmbH, Germany, Mo $\text{K}\alpha 1$ radiation source) in transmission geometry. The refinements of the obtained XRD patterns were performed using the General Structure Analysis Software-II (GSAS-II) software package [237]. The peak shape was fitted by using pseudo-Voigt profile functions and 10 background coefficients were fitted using Chebyshev-1 functions. Thermogravimetric analyses (TGA) were carried out by a thermal analysis device (STA 449F3 Jupiter, Netzsch, Germany) in flowing ammonia atmosphere (10 vol.% Ar in NH_3 ; Ar >99.999 %, Tyczka Industrie-Gase GmbH, purified by Entegris Gatekeeper GPUS IX $p(\text{O}_2) < 100$ ppt, $p(\text{H}_2\text{O}) < 100$ ppt; NH_3 >99.999 %, Air Liquide, purified by Entegris Gatekeeper GPUS YX $p(\text{O}_2) < 1$ ppb, $p(\text{H}_2\text{O}) < 1$ ppb) from room temperature to 110 °C for 2 h, and then heated to 1000 °C at the heating rate of 5 °C/min. The measurements were corrected for the buoyancy. The surface morphology of the annealed samples was investigated with a Philips XL30 FEG high-resolution scanning electron microscope (FEI Company, Hillsboro, Oregon, USA), coupled with an energy-dispersive X-ray (EDX) spectroscope (Mahwah, New Jersey, USA). Transmission electron microscopy (TEM) in combination with the selected area electron diffraction (SAED) technique was done on a JEM-2100 microscope (JEOL Ltd, Tokyo, Japan) at an acceleration voltage of 200 kV (wavelength 152.51 pm) to investigate the generated microstructure and phase composition of the SiHfN ceramics. Carbon and nitrogen/oxygen contents of the SiHfN ceramic powder ammonolyzed at 1000 °C were measured using a LECO C-200 (LECO Instrumente GmbH, Mönchengladbach, Germany) and a LECO TC-436 analyzer, respectively. The elemental analysis of the SiHfN pellets annealed at high temperatures was performed by EDX.

3.1.1.3 Mechanical properties

The as-prepared pellets were finally polished with 1/4 μm polycrystalline diamond powder on a felt cloth and subsequently cut into a rectangular shape with a dimension of $4 \times 3 \times 2 \text{ mm}^3$ for measurements

of the mechanical properties. The skeletal density and open porosity of the annealed monoliths obtained at 1300 °C were determined using the water immersion method (Archimedes' method) according to the following equations:

$$\rho_s = m_d \rho_{H_2O} / (m_d - m_{ww}) \quad (1)$$

$$P (\%) = (m_w - m_d) / m_w - m_{ww} \% \quad (2)$$

where, ρ_s and ρ_{H_2O} are the skeletal density and density of water, P (%) is open porosity. m_d is the dry weight of the pellets. The pellet was vacuumed in deionized water until no more bubbles appeared within 10 min, and the weight of the wet pellet (m_w) was obtained, while m_{ww} amounts the weight of the pellet immersed in water. All samples have been dried at 60 °C for 24 h before the measurements. Furthermore, the true density is measured by pycnometer method using ethanol as medium based on Eq. (3).

$$\rho_t = m \rho_1 / (M_1 + m - M_2) \quad (3)$$

where ρ_t is the true density, ρ_1 is absolute ethanol density (0.78945 g/cm³ at 20 °C), M_1 is pycnometer weight filled with absolute ethanol, m is the sample mass, and M_2 is the pycnometer mass added the SiHfN-13 powder into the pycnometer. By repeating the above measurements for 5 times, the true density of the SiHfN-13 powder is analyzed to be 3.42 g/cm³.

Vickers hardness measurements were performed on an AHVD-1000XY microindenter (Shanghai Jvjing Precision Instrument Manufacturing Co., Ltd., China) with a diamond Vickers point under a load of 9.8 N held for 15 s. For additional nanoindentation studies, the samples were glued onto an aluminum holder and then fixed on the stage for the nanoindentation measurements using an iNano device (Nanomechanics Inc., Oak Ridge, TN, USA). For each sample, 9 random indentations were performed on the polished surface using a Berkovich tip (Synton-MDP AG, Nidau, Switzerland), and the maximum load was 50 mN at a strain rate of 0.2 $\mu\text{N s}^{-1}$. The recorded load-displacement curves during both loading and unloading were analyzed using the built-in software package based on the model proposed by Oliver and Pharr [238]. The machine compliance and tip area function were calibrated by a fused silica reference sample.

3.1.2 Results and discussion

3.1.2.1 Fabrication of bulk SiHfN ceramic

The polymer-to-ceramic transformation of the PHPS and Hf-modified PHPS precursor were investigated via TGA/DTA measurements. As demonstrated in the TGA/DTA curves (Figure 3. 1), the original PHPS shows a ceramic yield of 83.0 wt% at 1000 °C for 2 h under ammonia, while the ceramic yield of the SiHfN precursor can be significantly raised up to 97.4 wt% by the addition of hafnium. The

exothermic peaks at ca. 110 °C and 200 °C, respectively, shown in Figure 3. 1 indicate typical cross-linking reactions assigned to dehydrocoupling and transamination, along with bond redistribution and thermal decomposition. In the temperature range from RT to approximately 110 °C, PHPS exhibits a minor weight loss of 0.3 wt%, while the SiHfN precursor presents a weight loss of 1.3 wt%. As the temperature increases to approximately 200 °C, the weight loss of PHPS is as high as 13.9 wt%, while the SiHfN precursor shows a slight change of 0.44 wt%, indicating that the cross-linking reaction temperature of the original PHPS is much higher than that of the SiHfN precursor. High cross-linking reaction temperature is detrimental for the preparation of dense bulk materials as cross-linking is usually accompanied by decomposition and gas evolution. Interestingly, the SiHfN precursor exhibits an obvious weight gain in the temperature range from 200 °C to 400 °C, while PHPS always shows a weight loss. According to our previous study [19], the Hf-modified PHPS leads to a significant increase in the nitrogen content in the resultant SiHfN ceramics due to the reaction of the polymeric precursor and ammonia. In reactive ammonia atmosphere, excess silicon remaining in the PHPS precursor can be terminated by NH₃, and the obtained NH_x-terminated Si easily reacts with TDMAH to form Si-N-Hf linkages at around 300 °C [239, 240]. However, the terminated NH_x in the pure PHPS-derived ceramic will be decomposed without the formation of further linkages, resulting in a continuous weight loss. Therefore, the Hf-modified PHPS does not only enhance the cross-linking reaction of the polymer, but also significantly increases the ceramic yield. The weight loss at temperatures beyond 400 °C (Figure 3. 1b) is attributed to transamination reactions between NH/NH₂ and the NMe₂ dimethylamido ligands, and the removal of carbon or carbon residues by the reaction with ammonia [241, 242]. Additionally, the cross-linking degree of the precursor can be significantly improved if higher pressures are applied during the warm-pressing process. These results indicate that the highly cross-linked SiHfN precursor can be prepared at a temperature range between 100 °C and 200 °C. The density of green bodies prepared at 100 MPa pressure and at 110 °C, 150 °C, and 200 °C was measured. Accordingly, there is no change in the density values of samples warm-pressed at 110 °C and 150 °C. The green body derived at 200 °C is delaminated after the mechanical demolding (Figure 3. 2). Consequently, the temperature for warm-pressing is fixed at 110 °C, being most energy-efficient, and the influence of the pressure of the warm-pressing step on the density and mechanical properties is further investigated.

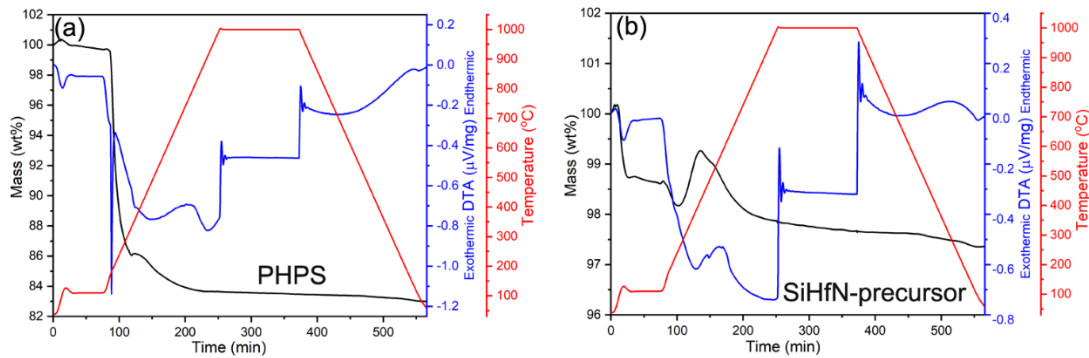


Figure 3. 1 TG (black lines), DTA (blue lines), and temperature (red lines) curves of (a) original PHPS and (b) SiHfN precursor under flowing ammonia/argon atmosphere (90 vol.% NH₃).

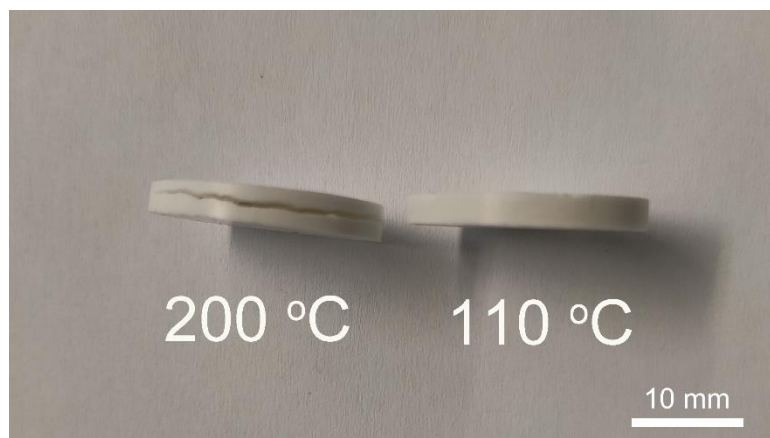


Figure 3. 2 Optical images of SiHfN green bodies prepared at 100 MPa, 110 °C, and 200 °C.

The open porosity and skeletal densities of the SiHfN specimens annealed at 1300 °C are presented in Figure 3. 3. It can be seen that the open porosity and skeletal density are strongly affected by the pressure applied during warm-pressing. The open porosity initially decreases, and the minimum open porosity is as low as 2.35 % at a pressure of 120 MPa. However, the relative density of the SiHfN-13 ceramic warm-pressed at 120 MPa amounts to 84% according to the ratio of skeletal density and true density, indicating that additional closed pores are present. The open porosity increases to 19.65 % if pressures up to 200 MPa are used during warm-pressing, and the reasons will be presented in combination with SEM studies. Meanwhile, the skeletal densities of the samples show the opposite variation trend as the open porosity. The “theoretical density” of the amorphous Si₃N₄ has seldom been reported because its composition, especially the hydrogen content, is difficult to determine and to estimate and has a significant effect on the density of amorphous Si₃N₄. Undoubtedly, the skeletal density of the amorphous matrix is lower than that of the corresponding crystalline counterpart. Therefore, the amorphous SiHfN specimen shows a low density (2.84 g/cm³) as compared to the theoretical density of crystalline Si₃N₄ (3.2 g/cm³). Indeed, the warm-pressing method developed here is of excellent advantage in terms of the

synthesis of Si₃N₄-based ceramics in amorphous form, via a simple process at low temperature, low porosity, and without sintering additives.

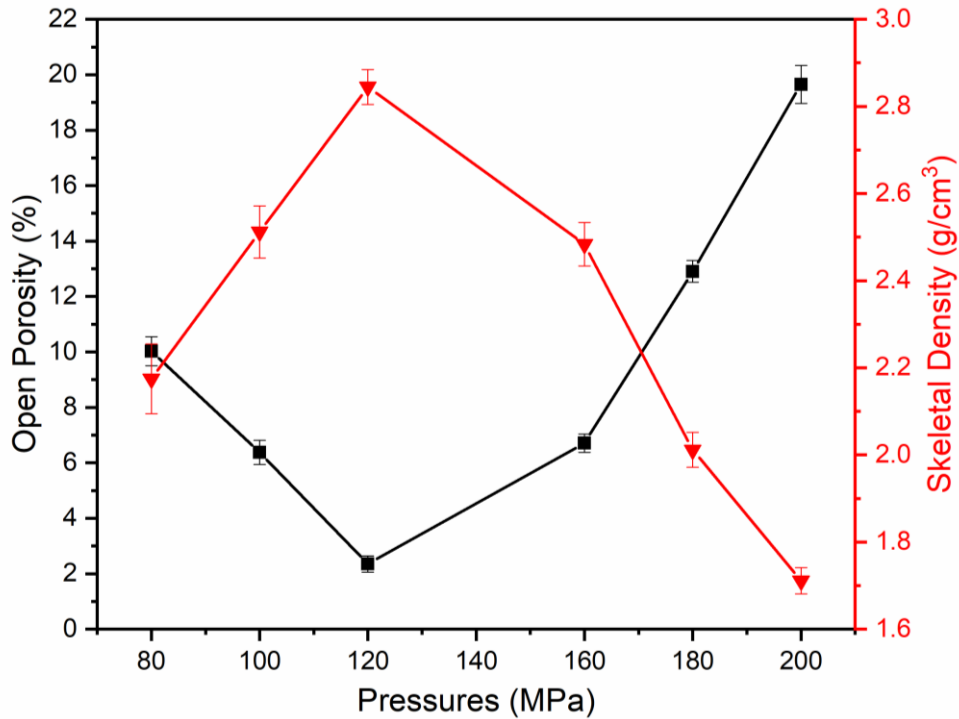


Figure 3. 3 Open porosity and skeletal density of SiHfN ceramics annealed at 1300 °C as a function of pressure applied during warm-pressing.

The densification of samples warm-pressed at various pressures is investigated by analyzing the polished surface of the SiHfN samples, and SEM micrographs are shown in Figure 3. 4. According to XRD results presented in Figure 3. 7, it is worth to note that all samples show no crystalline phase, indicating that the SiHfN samples remain amorphous even at high temperatures up to 1300 °C. A few separated micron-sized pores are found in the pyrolyzed samples (Figure 3. 4a, b, c, d) warm-pressed under 80 and 100 MPa. The specimen obtained under 120 MPa shows almost complete densification, without open pores and cracks (Figure 3. 4e, f). The sample prepared at higher warm-pressing pressures (> 120 MPa) exhibits pores and cracks (see Figure 3. 4g, h, i, j, k, l), in comparison to the pyrolyzed sample warm-pressed at 120 MPa.

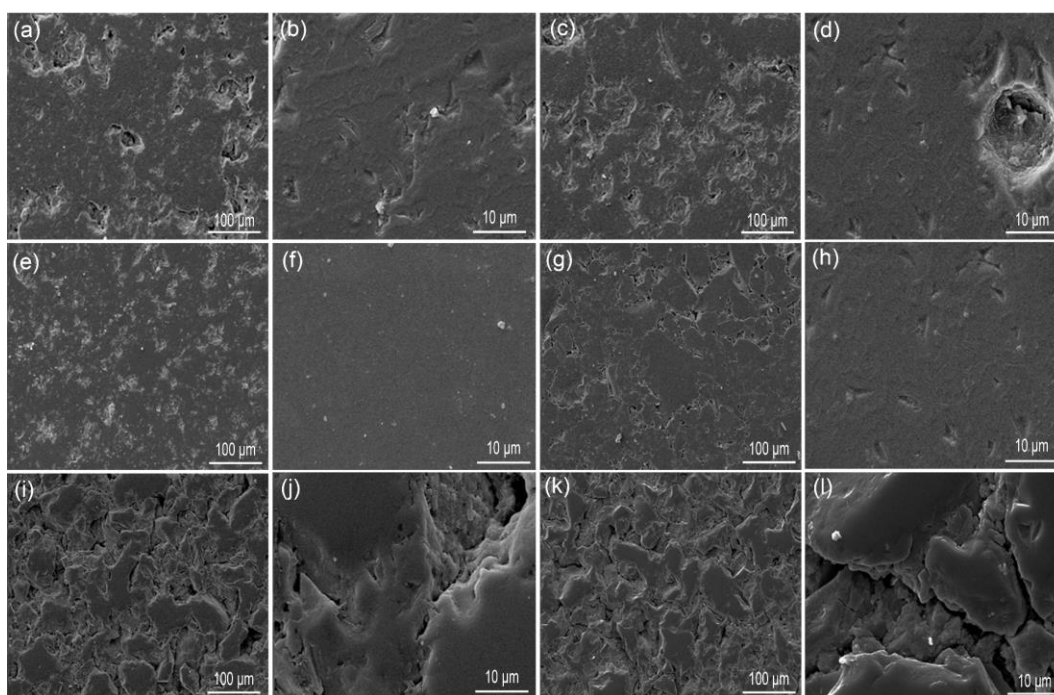


Figure 3. 4 SEM micrographs taken with 15 kV accelerating voltage of SiHfN samples produced at 1300 °C warm-pressing at 110 °C and under different pressure loads as follows: (a, b) 80 MPa, (c, d) 100 MPa, (e, f) 120 MPa, (g, h) 160 MPa, (i, j) 180 MPa, and (k, l) 200 MPa.

We assume that there are two reasons for the formation of pores and cracks, which are discussed as follows: i) Densification of the warm-pressed samples at high pressures prevents the effluence of gaseous by-products from inside to the surface during further ammonolysis, leading to the formation of pores and cracks; ii) A springback mechanism when releasing the pressure in uniaxial warm-pressing of the precursor is the second reason, resulting in defects (pores and cracks) at higher pressures due to the formation of pressure gradients during pressing [243]. Figure 3. 5 summarizes the densification process of the cross-linked SiHfN precursors by cold and warm-pressing. During the cold pressing, particle arrangement and particle sliding occur via physical force to gradually consolidate the samples. With respect to the warm-pressing densification process, further particle arrangement and particle sliding are triggered due to the inner- and inter-particle cross-linking reactions and the plastic deformation of the polymeric precursor. The sample is deformed to a dense green compact, and then the deformation is fixed by increasing the holding time. However, the warm-pressed samples undergo a significant springback when the pressure and temperature exceed critical values. Therefore, the densification exhibits a turning point at a pressure of 120 MPa as presented in Figure 3. 3, and the springback will occur at 160 MPa after unloading pressure and lead to a counterproductive effect on the densification. In addition, as can be seen from the EDX elemental mapping of the annealed SiHfN ceramic shown in Figure 3. 4 A, Si, N, and Hf elements are distributed homogeneously in the amorphous structure without obvious agglomeration. Elemental composition obtained from EDX is shown in Table 3. 1, indicating

that the SiHfN-13 sample is a ceramic with a composition of $\text{Si}_{1.00\pm 0.06}\text{Hf}_{0.05\pm 0.01}\text{N}_{1.30\pm 0.10}\text{O}_{0.32\pm 0.08}$. Carbon element can no longer be detected, in agreement with the ammonolyzed ceramic powder at 1000 °C (0.01 wt%). However, the oxygen content in the SiHfN-13 pellets (8.66 ± 2.09 wt%) is higher than oxygen contents of the ammonolyzed ceramic powder at 1000 °C (2.03 ± 0.46 wt%), which is inevitably caused during the process of warm-pressing and polishing in the air. Therefore, oxygen is mainly present on the surface of the sample, which is also verified by the following XRD results.

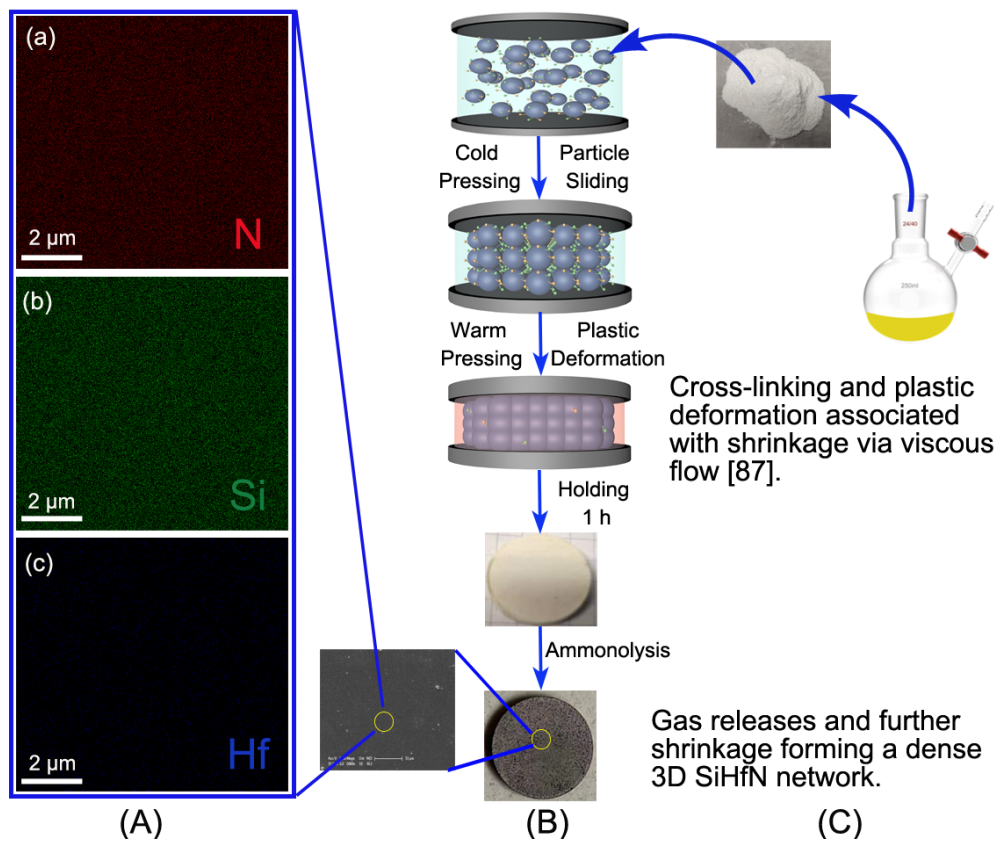


Figure 3. 5 (A) Elemental mappings of the SiHfN ceramic prepared via warm-pressing of the precursor at 120 MPa and subsequent annealing at 1300 °C. (B) Schematic diagram of the preparation principle of high-density SiHfN ceramic: The first step corresponds to the cold pressing of the polymer. The second step is the controlled warm-pressing of the SiHfN precursors into a green body, and the final step corresponds to the pressureless ammonolysis of a representative disk-shaped SiHfN specimen. (C) Basic suggested principles involved in the warm-pressing procedure from polymeric precursor to dense SiHfN ceramic [87].

Table 3. 1 Elemental composition of the annealed SiHfN ceramics.

Sample	Composition (wt%)					Empirical formula
	Si	Hf	N	O	C	
SiHfN (1000 °C)	49.68±	14.77±	33.51±	2.03±	0.01	$\text{Si}_{1.00\pm 0.06}\text{Hf}_{0.05\pm 0.01}\text{N}_{1.35\pm 0.16}\text{O}_{0.07\pm 0.02}\text{C}_{0.0005}$
	3.16	2.72	3.84	0.46		
SiHfN-13	46.81±	13.93±	30.60±	8.66±	-	$\text{Si}_{1.00\pm 0.06}\text{Hf}_{0.05\pm 0.01}\text{N}_{1.31\pm 0.14}\text{O}_{0.32\pm 0.08}$
	2.98	2.07	3.34	2.09		
SiHfN-17	45.39±	11.56±	31.97±	11.08	-	$\text{Si}_{1.00\pm 0.12}\text{Hf}_{0.04\pm 0.01}\text{N}_{1.41\pm 0.19}\text{O}_{0.43\pm 0.15}$
	5.31	3.19	4.21	±3.77		

3.1.2.2 Crystallization and thermal behavior

In order to investigate the crystallization and thermal behavior of the SiHfN-based ceramics annealed at different temperatures, XRD, TEM, and surface changes of the ceramics were measured and recorded, and the results are shown in Figures 3. 6 – 3. 10.

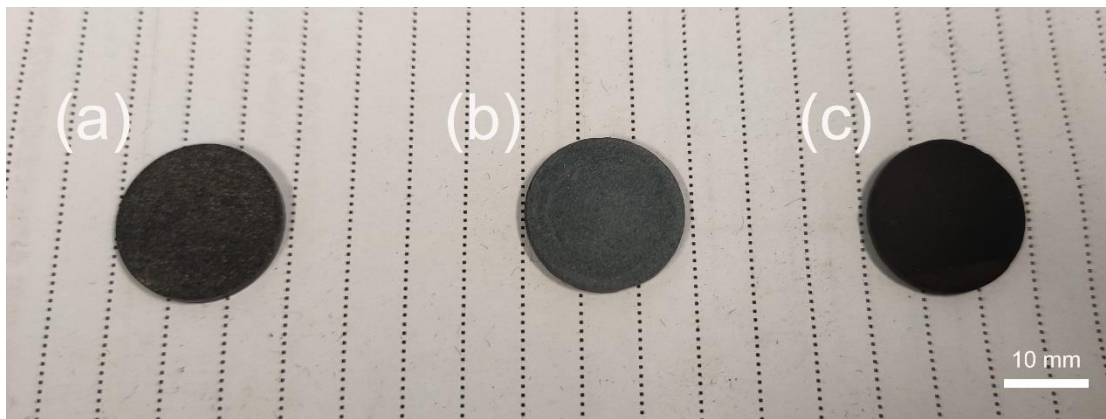


Figure 3. 6 Optical images of SiHfN ceramic specimens: (a) SiHfN-13, (b) SiHfN-15, and (c) SiHfN-17.

Optical images of the SiHfN ceramics after annealing at different temperatures are displayed in Figure 3. 6. The samples degrade uniformly, and their surface gradually becomes rougher with increasing annealing temperature, which is illustrated below.

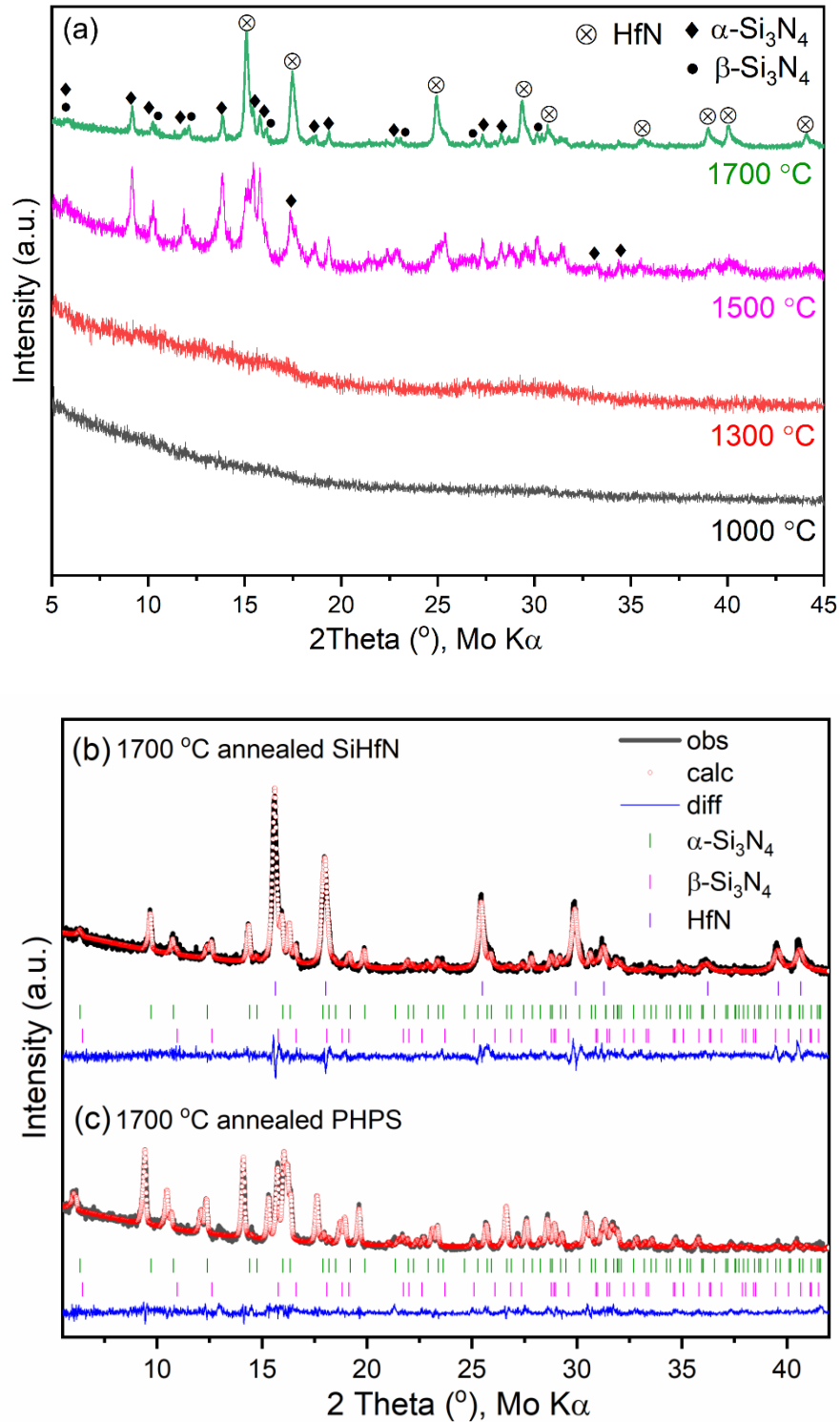


Figure 3. 7 (a) XRD patterns of the SiHfN ceramics annealed at 1000 °C, 1300 °C, 1500 °C, and 1700 °C; Rietveld refinements of the XRD patterns of (b) SiHfN ceramic and (c) PHPS-derived Si $_3$ N $_4$ annealed at 1700 °C.

XRD patterns (Figure 3.7) and TEM images combined with SAED patterns (Figure 3. 9a, b) reveal that the SiHfN ceramic obtained at 1000 °C is mainly X-ray amorphous. While with increasing annealing temperature up to 1300 °C, the ceramic sample shows a weight loss of 0.81 wt% (Figure 3. 8), and the XRD pattern remains X-ray amorphous as that of the sample at 1000 °C (Figure 3. 7). The corresponding SAED (inset in Figure 3. 9c) pattern also proves that the SiHfN ceramic is amorphous, which further verifies the conclusion drawn from the XRD pattern. Therefore, further densification of the annealed pellet has occurred at 1300 °C rather than a phase transformation. Interestingly, the high-resolution TEM (HRTEM) image (Figure 3. 9d) of the SiHfN ceramic shows a small amount of HfN nanoprecipitations embedded within an amorphous SiHfN-based matrix, indicating that crystallization takes place at 1300 °C starting from Hf-containing regions, which is not visible from the XRD pattern shown in Figure 3. 7.

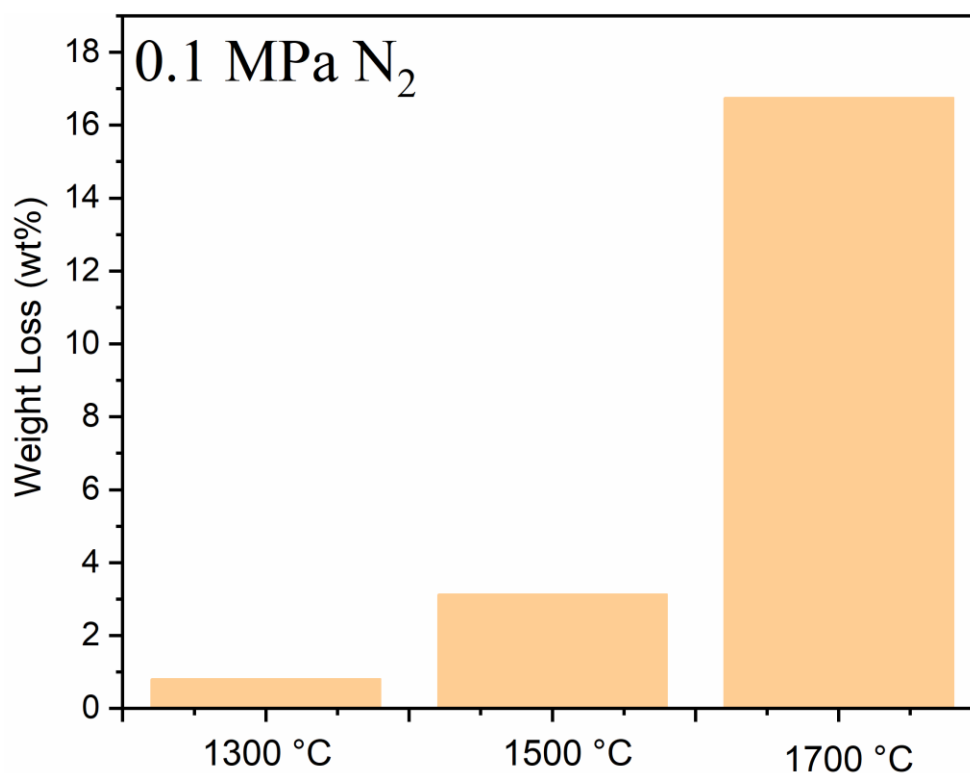


Figure 3. 8 Weight loss of the SiHfN-13, SiHfN-15, and SiHfN-17 ceramic samples after annealing at different temperatures in 0.1 MPa N₂.

The weight loss of the sample amounts 3.13 wt% (Figure 3. 8) when the annealing temperature is raised to 1500 °C, which is attributed to the decomposition of amorphous SiN_x-rich regions, SiN_x = x Si + N₂ (weight loss) [244]. Characteristic reflections of α-Si₃N₄, β-Si₃N₄, and HfN are found in the XRD pattern (Figure 3. 7). Furthermore, nanocrystalline α-Si₃N₄ segregations and HfN nano-grains (ca. 10 nm) are also observed in HRTEM and SAED micrographs (Figure 3. 10a, b), which is consistent with the XRD results and confirms that the X-ray amorphous SiHfN ceramic converts into HfN/Si₃N₄ nanocomposites undergoing phase separation and crystallization at 1500 °C. The slight weight loss of 3.13 wt% indicates

the high temperature resistance of the HfN/Si₃N₄ ceramic nanocomposites [245]. It is worth noting that the diffraction intensity of β-Si₃N₄ is quite weak, indicating that almost no α-Si₃N₄ to β-Si₃N₄ transformation takes place at 1500 °C, the reason is discussed in more detail below.

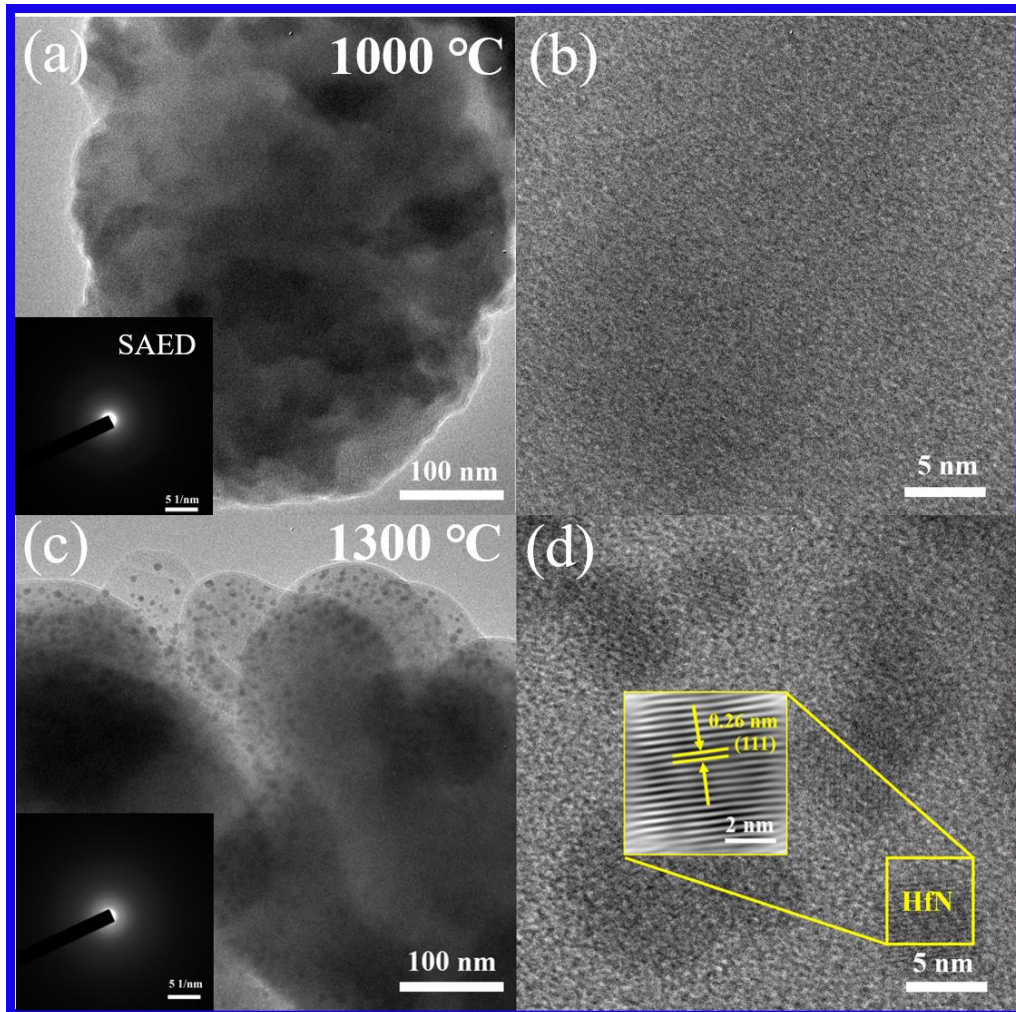


Figure 3. 9 TEM images of SiHfN annealed at 1000 °C (a and b) and at 1300 °C (c and d); (b) and (d) are high resolution micrographs magnified from (a) and (c), respectively; the inset in (a) and (b) is the SAED images; the inset in (d) is the FFT image from the selected area.

A weight loss of 16.76 wt% (Figure 3. 8) is measured after annealing the sample at 1700 °C in 1 bar nitrogen atmosphere. The weight loss here is likely ascribed to a partial decomposition of Si₃N₄ (cf., Si₃N₄ = 3 Si + 2 N₂) at higher temperature (≥ 1650 °C) [171], which results in pores and a decrease of the SiHfN ceramic density. It can be evidently seen from the XRD pattern in Figure 3. 7 that the rather sharp reflections concentrated at 2 Theta = 15.60°, 18.03°, 25.61°, 30.13°, and 31.50° correspond to the (111), (200), (220), (311), and (222) lattice planes of HfN, respectively, which means that HfN nanodots (ca. 50 nm) are well-crystallized after annealing at 1700 °C. The XRD pattern of the SiHfN-17 sample analyzed by Rietveld refinements (Figure 3. 7, Table 3.2 and 3. 3) shows that the predominant phase in the ceramic is α-Si₃N₄ (71.3 wt%), and the rest is related to β-Si₃N₄ (14.3 wt%) and HfN (14.4 wt%).

The weight fraction of HfN determined by Rietveld refinements is consistent with the elemental analysis result (Table 3. 1) obtained by EDX (12.5 wt%). The refinements of the XRD pattern of the ceramic derived from PHPS at 1700 °C (Figure 3. 7c) reveals a phase composition composed of α -Si₃N₄ (76.4 wt%) and β -Si₃N₄ (26.3 wt%). It is well documented that the phase transformation from α -Si₃N₄ to β -Si₃N₄ starts at ~1650 °C, and is basically completed at ~1700 °C [246-248]. Therefore, we assume that the addition of Hf has a remarkable effect on the phase transformation, suppressing the formation of β -Si₃N₄ at high temperatures. Additional evidence is supplied by HRTEM and SAED micrographs (Figure 3. 10c, d). The (202) lattice plane of α -Si₃N₄ can be found in the SAED micrograph (inset in Figure 3. 10c). Lattice fringes with a distance of 0.26 nm and 0.67 nm are analyzed in Figure 3. 10b, corresponding to the (111) lattice plane of HfN (JPCDS card no. 00-065-4298) and the (100) lattice plane of α -Si₃N₄ (JPCDS card no. 00-071-0623), respectively, in agreement with the XRD results. No β -Si₃N₄ is found in the sample annealed at 1500 °C in the TEM image.

Table 3. 2 Results of the Rietveld refinements.

Parameter	α -Si ₃ N ₄	β -Si ₃ N ₄	HfN
Space group	<i>P3₁c</i>	<i>P6₃/m</i>	<i>Fm$\bar{3}$m</i>
<i>a</i> (Å)	7.767(2)	7.62(1)	4.5978(3)
<i>c</i> (Å)	5.631(1)	2.869(1)	~
<i>V</i> (Å ³)	294.17(9)	144.467(3)	97.20(2)
<i>R</i> _{wp} (%)		9.988	

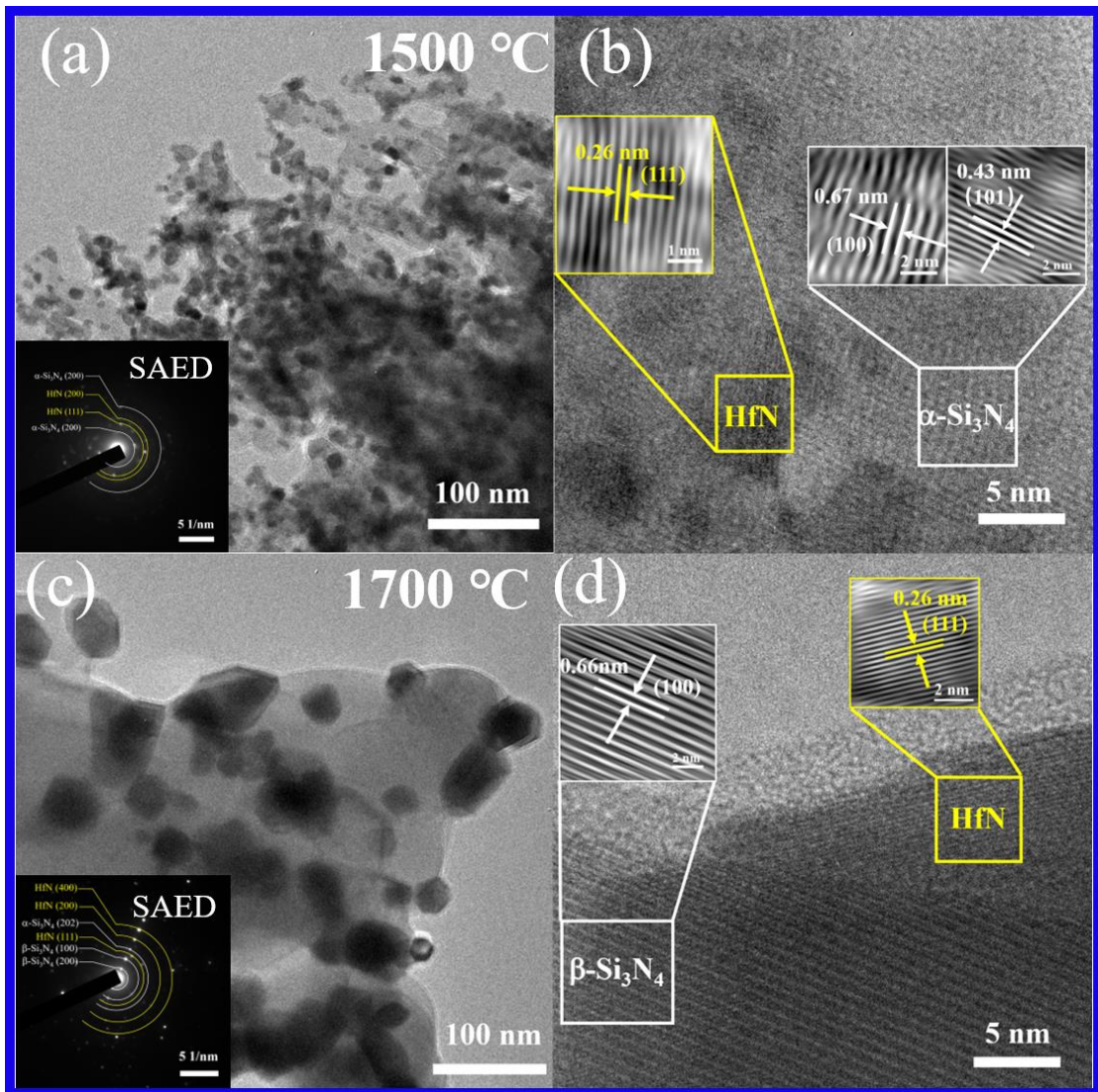


Figure 3. 10 TEM micrographs of SiHfN-15 (a and b), b) is a high-resolution image enlarged from a) and SiHfN-17 (c and d), d) is a high-resolution image magnified from c); the inset in (a) and (b) is a SAED image; the insets in (b) and (d) are FFT images from the selected areas.

Table 3. 3 Refined structural parameters.

Sample	Atom	<i>x</i>	<i>y</i>	<i>z</i>	<i>U_{iso}</i> (Å ²)
α -Si ₃ N ₄	Si(1)	0.519(6)	0.427(5)	0.638(4)	0.1113
	Si(2)	0.165(2)	0.916(2)	0.441(2)	0.0101
	N(1)	0.572(9)	0.915(11)	0.49(3)	0.1781
	N(2)	0.334(7)	0.022(9)	0.70(1)	0.0338
	N(3)	0.66(6)	0.33(3)	0.66(2)	0.0614
	N(4)	0	0	0.49(2)	0.0046
β -Si ₃ N ₄	Si(1)	0.762(5)	0.158(5)	0.25	0.0820
	N(1)	0.037(5)	0.330(7)	0.25	0.0199
	N(2)	0.66(6)	0.33(3)	0.25	0.0373
HfN	Hf(1)	0	0	0	0.0100
	N(1)	0.5	0.5	0.5	0.0266

3.1.2.3 Mechanical properties

The investigation of crystallization and thermal behavior reveals that high annealing temperatures (≥ 1500 °C) inevitably cause the SiHfN ceramic to decompose by producing gas reducing the density of SiHfN ceramics. The SEM analysis indicates that pores and cracks are formed as the warm-pressing pressure increased to 200 MPa (Figure 3 .4k, l). Consequently, the investigation of the mechanical properties is focused on specimens prepared at warm-pressing pressures of 80 MPa, 100 MPa, 120 MPa, 160 MPa, and 180 MPa and subsequently annealed at 1300 °C. Random nano-hardness and Young's modulus of SiHfN samples are determined by means of nanoindentation tests and calculated from their load-displacement curve, as shown in Figure 3. 11. It can be seen that all the scattered points of the sample prepared at 120 MPa during warm-pressing almost fall onto the same region with a mean hardness of 17 GPa and Young's modulus of 185 GPa. However, the nano-hardness and Young's modulus of the other specimens show a relatively large dispersion of values. The closed pores, defects and cracks formed inside the SiHfN ceramics should be the most possible reason for the largely scattered data of nano-hardness and Young's modulus, because they can interact with the indentations and either

directly or indirectly affect the measured hardness and Young's modulus values. In addition, another mechanism affecting the nano-hardness and Young's modulus can be attributed to the presence of internal stresses in the SiHfN ceramics, owing to the thermal expansion mismatch of the amorphous Si₃N₄ matrix and partially crystallized HfN particles.

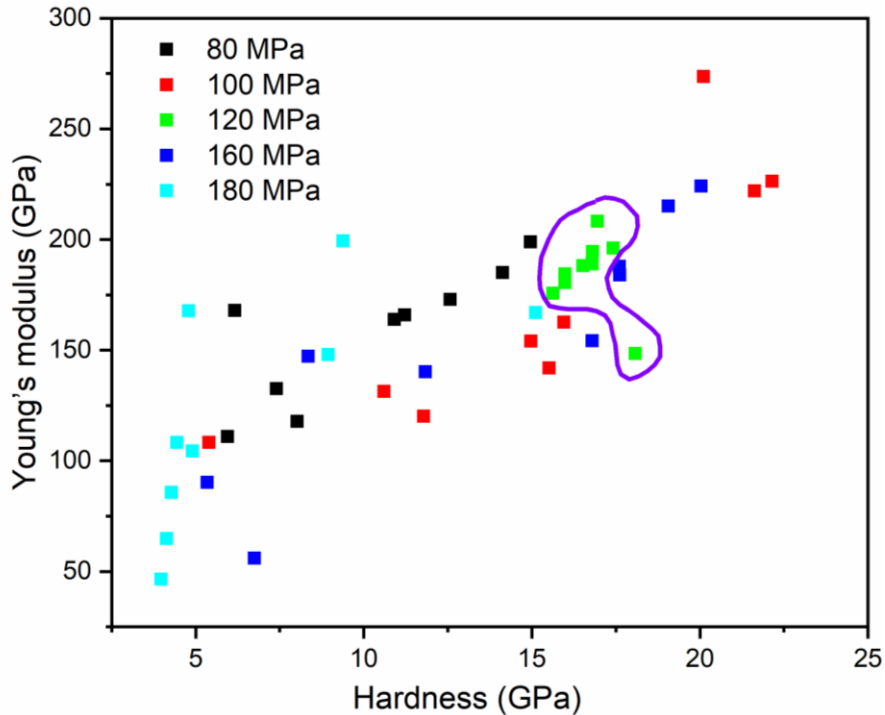


Figure 3. 11 Evolution of the nano hardness and Young's modulus obtained from 9 nanoindentation tests on SiHfN samples produced at 1300 °C after warm pressing at different loads.

The Vickers hardness of the SiHfN ceramics was also investigated by microindentation with the load setting to 9.8 N and the results are shown in Figure 3. 12. The Vickers micro-hardness exhibits an increasing trend up to a warm-pressing pressure of 120 MPa, and then decreases. Average maximum Vickers hardness of 19.6 GPa is achieved in SiHfN specimen prepared at 120 MPa, which shows a similar trend to the variation of skeletal density. Hence, the Vickers hardness value is also affected by the presence of porosity and induced defects. In addition, a comparison between this work and other recorded amorphous and polycrystalline Si₃N₄-based ceramics is summarized and shown in Figure 3. 13. It can be seen that the as-prepared SiHfN ceramic exhibits outstandingly higher nano and Vickers hardness than most of the previously reported Si₃N₄-based ceramics [21, 22, 194, 246, 249-257], which may provide a valuable guidance in the preparation of dense and additive-free Si₃N₄-based ceramics. Notably, TiN@a-Si₃N₄ ceramic prepared under the same condition shows higher hardness than that of HfN@a-Si₃N₄ ceramic due to the higher theoretical hardness of TiN (23.6 GPa) [258] compared with HfN (15.3 GPa) [258].

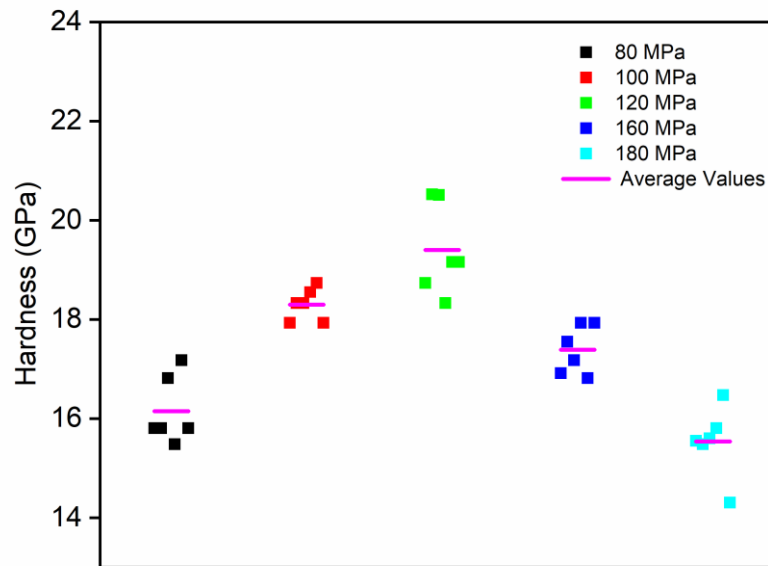


Figure 3. 12 Effect of the pressure applied during warm-pressing on the Vickers hardness of SiHfN ceramics.

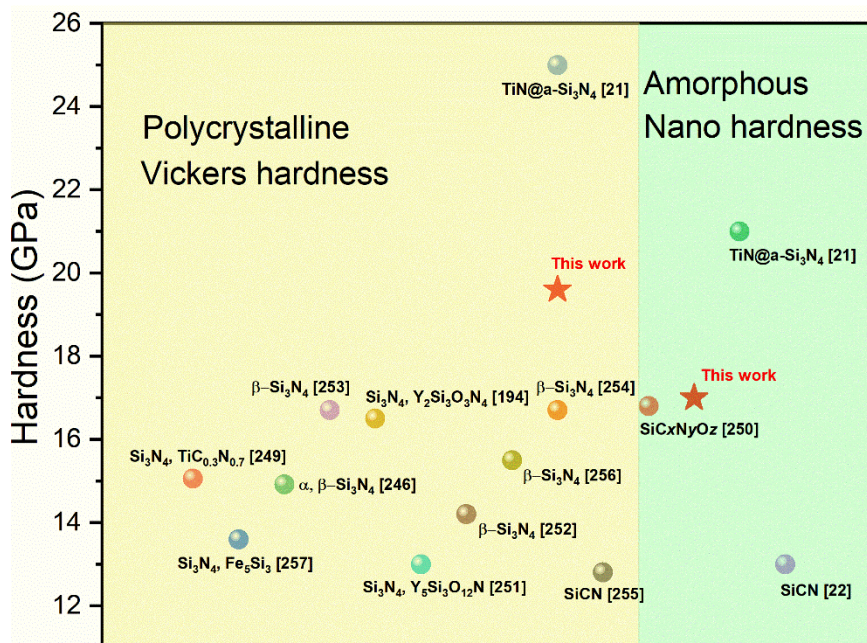


Figure 3. 13 Comparison of the Vickers hardness and nano hardness of the amorphous SiHfN-13 ceramic prepared by warm-pressing at 120 MPa and reported silicon-based bulk ceramics.

3.1.3 Conclusion

In the present study, additive-free amorphous bulk SiHfN ceramics were successfully fabricated by in situ consolidation of preceramic polymer powders via warm-pressing followed by ammonolysis and annealing. Investigation of the warm-pressing conditions shows that temperature and pressure have a

significant influence on the consolidation of the polymer powders, the subsequent polymer-to-ceramic conversion process, and the density of the obtained SiHfN ceramics. Although warm-pressing at 150 °C and 200 °C and high loads (> 120 MPa) promotes further cross-linking and improved densification of the green bodies, cracks are formed due to the lack of pores for degassing of volatile species and byproducts during the final ammonolysis. The optimum densification condition is achieved at 110 °C under 120 MPa during warm pressing. The microstructural investigation of the SiHfN ceramics reveals that the crystallization of the amorphous SiHfN ceramic begins at 1300 °C starting from Hf-containing regions. The SiHfN ceramics annealed at 1500 °C and 1700 °C convert into HfN/ α -Si₃N₄ and HfN/ α -Si₃N₄/ β -Si₃N₄ nanocomposites, respectively. In addition, the impact of pressure during warm-pressing of the green samples on the mechanical properties of the obtained amorphous bulk SiHfN ceramics has been investigated. The highest mechanical properties of the SiHfN ceramic are obtained by warm pressing of the preceramic polymer at 120 MPa and subsequent annealing of the green sample at 1300 °C. Its open porosity, Vickers hardness, nano hardness, and Young's modulus are found to be 2.35 %, 19.6 GPa, 17 GPa, and 185 GPa, respectively. These values show a significant improvement in comparison to most of the reported polymer-derived amorphous and polycrystalline Si₃N₄-based ceramics. Therefore, the present work indicates that amorphous bulk Si₃N₄-based ceramic nanocomposites with prospective mechanical properties can be prepared via the PDC route.

The content of this Chapter is under review:

2. **Li W**, Yu Z, Wiehl L, et al. Hard and Tough Novel High-Pressure γ -Si₃N₄/Hf₃N₄ Ceramic Nanocomposites [J]. *Journal of Advanced Ceramics*, Available online: 08 May 2023.

In this chapter, the structural evolution of the amorphous SiHfN precursor and its crystallization to γ -Si₃N₄/Hf₃N₄ ceramic nanocomposites under HPHT is firstly assessed by in-situ synchrotron energy-dispersive X-ray diffraction measurements at ~19.5 GPa in the temperature range from 990 °C to 1920 °C. The optimal condition for the formation and stability of the γ -Si₃N₄/Hf₃N₄ ceramic nanocomposites was determined to be 19.5 GPa and 1500 °C. Then, the investigation of the mechanical properties of the resultant γ -Si₃N₄/Hf₃N₄ nanocomposites reveals that the γ -Si₃N₄/Hf₃N₄ (6.98 MPa m^{1/2}) ceramic nanocomposite exhibits a significant improvement in fracture toughness than that of pure γ -Si₃N₄ (3.5 MPa m^{1/2}) without sacrificing the hardness of the material.

3.2.1 Experimental methods

3.2.1.1 Single-source-precursor synthesis and ammonolysis

Hf-containing single-source precursor for the preparation of the SiHfN based ceramic was synthesized upon the chemical modification of the commercial perhydropolysilazane solution (20 wt% of PHPS in dibutyl ether, Merck, KGaA, Germany) by tetrakis(dimethylamido) hafnium (IV) (TDMAH, $\geq 99.99\%$, Sigma-Aldrich, Germany) with a weight ratio of TDMAH/PHPS = 30/70 [19]. Anhydrous toluene (Merck, Germany) was used as the reaction solvent. The synthesis of the single-source precursor was performed under an argon atmosphere using the standard Schlenk technique. The synthesis process was carried out through the following steps: the brown and transparent solution of 1 g TDMAH dissolved in 5 mL anhydrous toluene was added dropwise into a solution of 11.5 g PHPS (2.3 g pure PHPS) with constant stirring at room temperature for 6 h until a milky white gel-like reaction mixture was obtained. Then, the product was heated up to 50 °C for 2 h followed by vacuum drying (10–2 mbar) for 5 h to remove the solvent and low molecular weight by-products yielding a colorless solid precursor. The as-synthesized SiHfN precursor was ground and sieved in an Ar-filled glovebox to avoid contamination with air and moisture. The sieved fine powders were placed in an alumina boat and then transferred into a horizontal Schlenk tube under the protection of Ar atmosphere. Afterwards, the tube was pumped three times under vacuum and refilled with high-purity ammonia (NH₃ > 99.98 %, Air Liquide, H₂O \leq 200 wt. ppm) up to atmospheric pressure. The sample was ammonolyzed at 1000 °C for 2 h at a heating rate of 50 °C/h under a continuous flow of ammonia (1.5 L/h) and then cooled down to room temperature at a rate of 60 °C/h. The as-ammonolyzed specimen was used as raw material for the subsequent high-

pressure experiments.

3.2.1.2 High-pressure synthesis including in-situ ED-XRD

High-pressure high-temperature (HP-HT) experiments were carried out using a Hall-type six-ram large volume pressure (LVP) (mavo press LPQ6 1500-100; Max Voggenreiter GmbH, Germany) at the beamline P61B at DESY, Hamburg [259]. Tungsten carbide second stage anvils (32 mm Fujilloid TF08) with a truncated edge length of 4 mm were used to compress a 10 mm edge length MgO octahedron (Cr₂O₃-doped). The MgO octahedron assembly was used as pressure transmitting medium along with a hBN-TiB₂ cylindrical heater. Further details about the assembly can be found elsewhere [259]. The obtained precursor powder was hand-pressed into a hole in a metal disc (h = 1.4 mm, ϕ = 1.8 mm) inside the glovebox and then placed into an h-BN tube to avoid contact with air or moisture. The assembly was first compressed to the target pressure at room temperature and then heated stepwise to a target temperature.

HP-HT in-situ energy-dispersive X-ray diffraction (ED-XRD) used to investigate the crystallization behavior of the SiHfN ceramic. Prior to the experiments, the Ge-detector position was determined to be 5.009° using LaB₆ standard (NIST SRM 660c) and diffracted X-rays from the sample were collected in the energy range of 20 – 160 keV. ED-XRD patterns were recorded during heating at different temperatures up to 1920 ± 20 °C (based on a calibrated power-temperature relationship), after the temperature had reached a steady state during each heating step. The main phases were identified with the help of a program called PDIndexer [260]. The temperature dependence of the Si₃N₄ and Hf₃N₄ lattice parameters was determined using the program GSAS-II [237].

In-situ ED-XRD was also used to monitor the pressure in real-time inside the octahedron assembly using the MgO pressure marker (run #BT448, 19.5 ± 0.5 GPa). In order to investigate the mechanical properties of the obtained γ -Si₃N₄/Hf₃N₄ ceramic nanocomposites, an additional synthesis experiment was carried out without X-rays at a calibrated pressure and temperature (run # HH547, ~20 GPa and ~1500 °C). The sample recovered in run #HH547 was used for further characterizations.

3.2.1.3 Characterization

The synthesis and the crosslinking process of the single-source precursors were analyzed ex situ by Fourier transform infrared (FTIR) spectroscopy on a Varian IR-670 spectrometer (Agilent Technologies, USA), using attenuated total reflection (ATR) mode in the range of 500 – 4000 cm⁻¹. High-resolution angle-dispersive X-ray diffraction (AD-XRD) of the recovered samples was performed at the high-energy beamline P02.1 (60 keV, λ = 0.207 Å) of PETRA III, DESY, Hamburg. Quantitative phase analysis was made by Rietveld refinement, using the program GSAS-II [237]. The instrumental profile parameters were calibrated with a LaB₆ standard material. The surface of the recovered sample was coated with gold for the measurements of the microstructure and chemical composition using a scanning

electron microscope (FEI Company, Hillsboro, Oregon, USA) equipped with an energy-dispersive detector (EDX, Mahwah, New Jersey, USA). Carbon and nitrogen/oxygen contents of the SiHfN ceramic pyrolyzed at 1000 °C were measured using a LECO C-200 (LECO Instrumente GmbH, Mönchengladbach, Germany) and a LECO TC-436 analyzer, respectively. The content of silicon and hafnium was analyzed by EDX. The lamella for the transmission electron microscopy (TEM)/scanning transmission electron microscopy (STEM) measurements was prepared using a Jeol JIB-4600F focused ion beam (FIB) instrument. To investigate the micro-structure of the recovered sample (#HH547), transmission electron microscopy (TEM) images (some also at high resolution, HRTEM) were acquired along with selected area electron diffraction (SAED) patterns using a JEM ARM 200F microscope. The acceleration voltage was 200 kV. The Vickers hardness of the polished sample was measured for each applied load from 0.49 N to 19.6 N using a diamond indenter (FV-700B, Future-Tech, Japan), and the loading time was kept at 15 s. At least five indentations were repeated and averaged to ensure the reliability of the results. The impression diagonals and the crack length were measured by SEM for the calculation of the fracture toughness [25, 261].

3.2.2 Results and discussion

3.2.2.1 Single-source precursor synthesis and pyrolysis

The PHPS chemically-modified with TDMAH was investigated by FTIR spectroscopy. FTIR spectra of the dried pristine PHPS as well as after its reaction with TDMAH and of the obtained amorphous SiHfN ceramic are shown in Figure 3. 14. The absorption bands at 3372 and 1171 cm^{-1} (N–H), 2137 cm^{-1} (Si–H), and 840 – 1030 cm^{-1} (Si–N–Si) are characteristic for the dried pure PHPS. The FTIR spectrum of unreacted TDMAH exhibits typical C–H absorption bands at 2766, 2822, and 2948 cm^{-1} . The absorption bands at 932 and 1251 cm^{-1} are assigned to Hf–N–C vibrations [239]. The intensity of the N–H and Si–H absorption bands of the PHPS decreases after the chemical modification, indicating that the reaction with TDMAH occurred at the Si–H/N–H groups of PHPS. Based on the reported literatures [65, 239, 240] and our previous work [19], PHPS with Hf-modified N–H and Si–H bonds leads to the formation of N–Hf at N centers and Si–N–Hf linkages, which is accompanied by the release of HNMe_2 and CH_4 . The absorption peaks of the N–H and Si–H bands completely vanish after pyrolysis at 1000 °C, which indicates that complete polymer-to-ceramic transformation has been achieved.

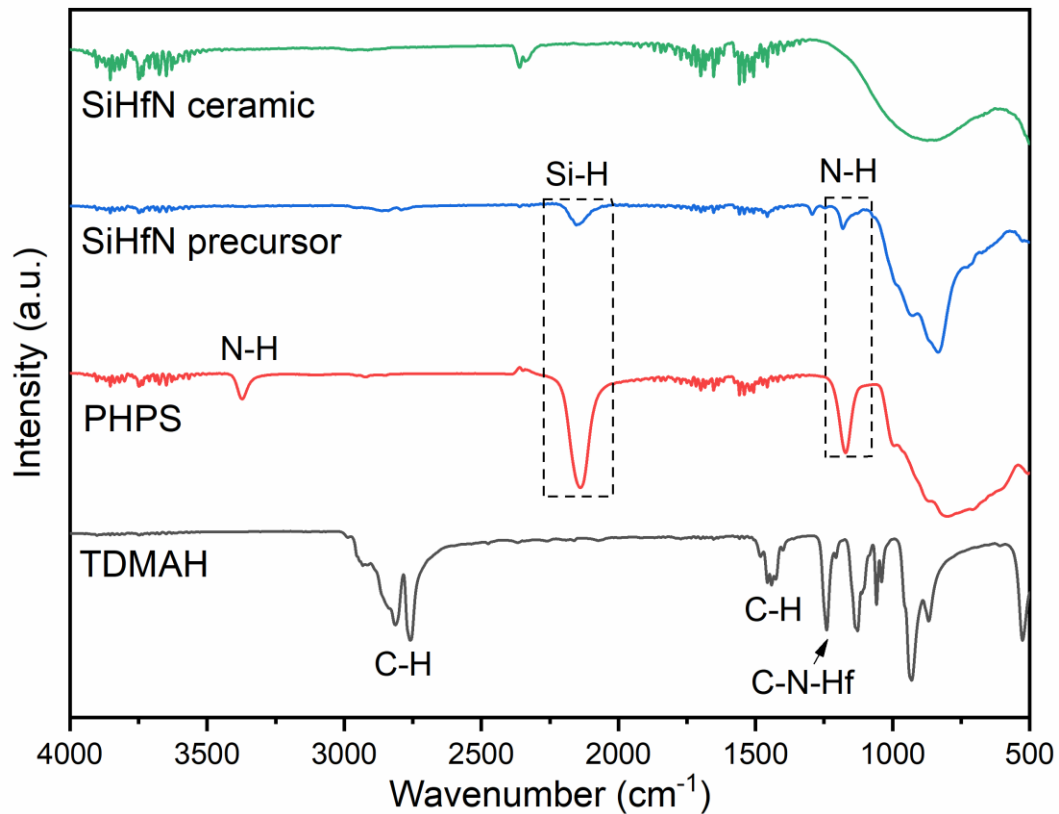


Figure 3. 14 FTIR spectra of TDMAH, dried PHPS, SiHfN precursor, and SiHfN ceramic obtained after pyrolysis of the precursor at 1000 °C in ammonia.

The ceramic yield of the SiHfN ceramic pyrolyzed at 1000 °C under ammonia is as high as 97.86 wt% (Figure 3. 15a). In the temperature range from room temperature to 245 °C, the SiHfN precursor shows a weight loss of 1.7 wt%, which is attributed to the volatilization and decomposition of low-molecular-weight oligomers, and also accompanied by cross-linking reaction assigned to dehydrocoupling. Interestingly, the TG curve of SiHfN precursor presents a mass gain of 1.1 wt% in the temperature ranging of 245 °C–417 °C. The weight gain is mainly related to the formation of Si-N-Hf linkages by the reaction between NH_x-terminated Si and TDMAH in the reactive ammonia atmosphere, leading to the increase in the nitrogen content [239, 240]. At temperatures beyond 417 °C, the SiHfN precursor exhibits a gradual weight loss, which is ascribed to the transamination reaction and removal of carbon residues by the reaction with ammonia [241, 242]. The elemental analysis of the as-obtained SiHfN ceramic revealed a composition of Si (49.68 wt%), Hf (14.77 wt%), N (33.51 wt%), O (2.03 wt%) and C (0.01 wt%), demonstrating that the Hf-modified PHPS leads to a significant increase in the nitrogen content in comparison with the pure PHPS (ca. 25 wt%). Based on the analytical data, a respective phase composition of 0.3 Si₃N₄ + 0.05 HfN + 0.07 SiO₂ is calculated according to the empirical formula of Si_{1.00}Hf_{0.05}N_{1.35}O_{0.07} by neglecting the carbon contamination. The Si:Hf ratio of the pyrolyzed SiHfN ceramic amounts ca. 21:1, which is close to the molar ratio used for the synthesis of the SiHfN precursor. According to our previous investigation [19], the modification of PHPS with TDMAH was limited in

the SiHfN system due to the steric hindrance and reactivity, which is consistent with our work. In addition, the XRD pattern shown in Figure 3.15b reveals that the as-obtained SiHfN ceramic is X-ray amorphous. Therefore, it has to be considered that during the subsequent high pressure and high temperature treatment of the amorphous SiHfN ceramic phase transitions will occur to form α -Si₃N₄, β -Si₃N₄, and γ -Si₃N₄, as well as HfN and Hf₃N₄.

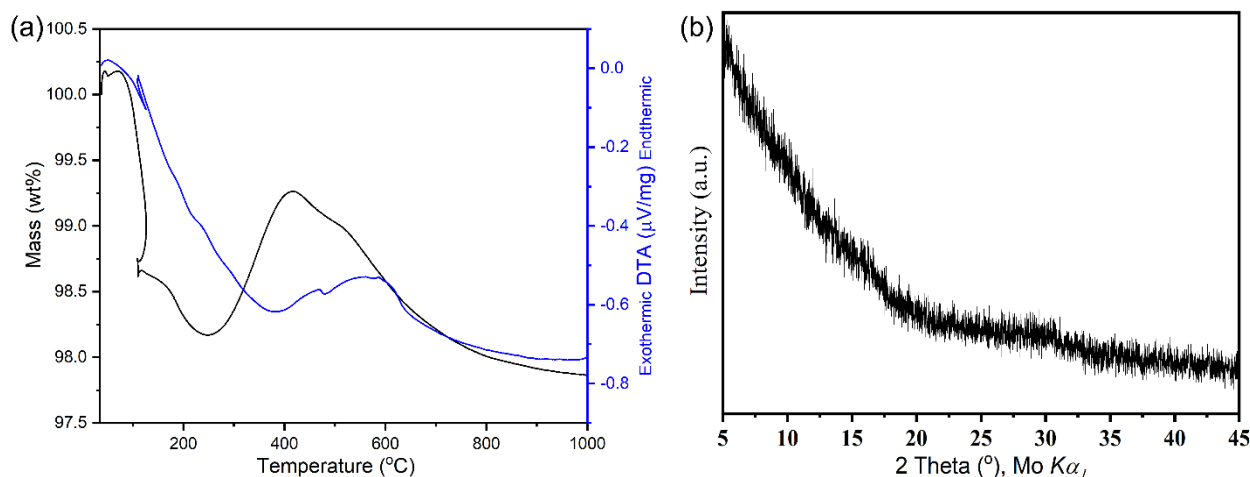


Figure 3. 15 (a) TG (black line) and DTA (blue line) curves of SiHfN precursor under flowing ammonia/argon atmosphere (90 vol.% NH₃). (b) XRD patterns of the SiHfN sample pyrolyzed at 1000 °C under ammonia atmosphere.

3.2.2.2 Structural evolution of the SiHfN ceramic at HP-HT

A selection of ED-XRD patterns recorded at 19.5 (± 0.5) GPa and at different temperatures in the range from room temperature to approx. 1920 °C (± 20 °C) are shown in Figure 3. 16. At 990 °C only intense fluorescence lines of Hf and Pb (from detector shielding materials) were observed, indicating that no crystalline phase is formed in the amorphous SiHfN ceramic up to this temperature, which is in agreement with our XRD results of the synthesized amorphous SiHfN ceramic (Figure 3. 15b). Starting at ~ 1090 °C, Bragg-reflections of γ -Si₃N₄ and Th₃P₄-type Hf₃N₄ appear and grow in intensity on further heating. In addition, some reflections of β -Si₃N₄ are visible at the beginning, which disappear on further heating. Under these conditions, β -Si₃N₄ transforms into the stable γ -phase. There are no further structural changes in the XRD patterns up to ~ 1570 °C, which reveals that the γ -Si₃N₄/Hf₃N₄ composite is thermodynamically stable up to ~ 1570 °C. Based on this observation, the synthesis conditions of around ~ 1500 °C and ~ 20 GPa are selected to prepare a γ -Si₃N₄/Hf₃N₄ ceramic nanocomposite in an additional experiment (#HH547). This sample is used for further analysis of the microstructure and mechanical properties.

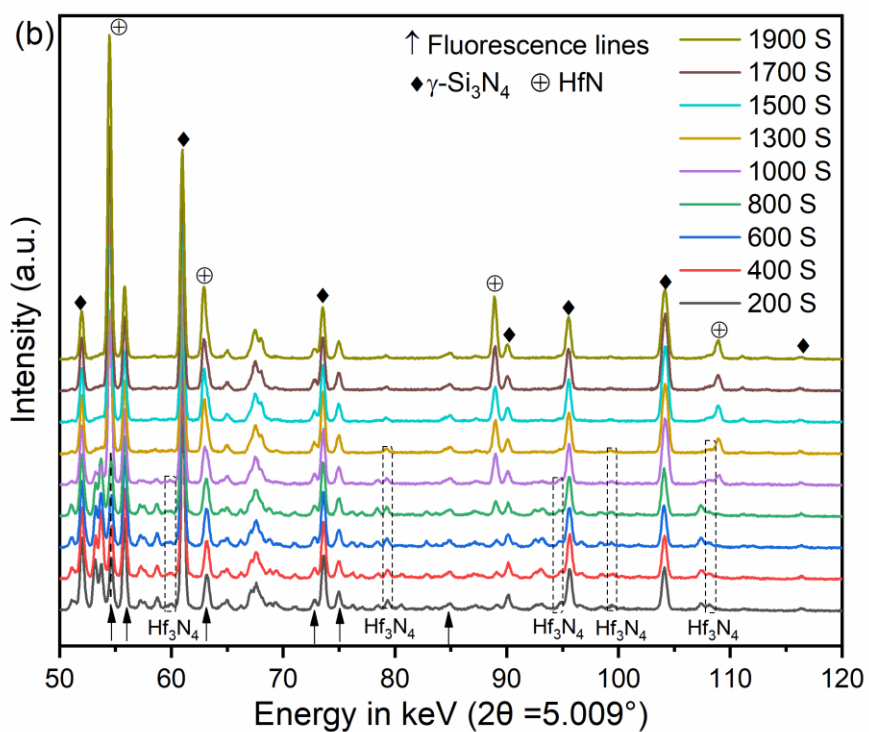
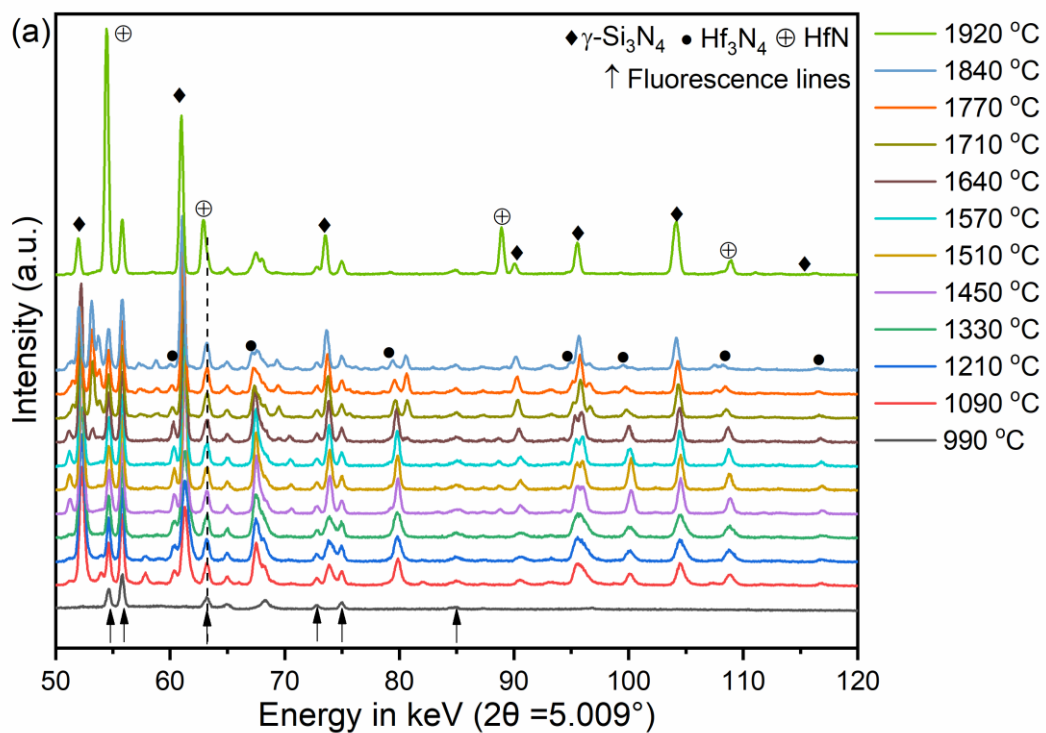


Figure 3. 16 Sequence of ED-XRD patterns, showing the phase transformation of the SiHfN ceramic at 19.5 (± 0.5) GPa: (a) on heating in the temperature range of 990 °C – 1920 (± 20) °C; (b) on holding the maximum temperature of 1920 °C during a time range between 200 and 1900 s.

Above this temperature, some new peaks appear and gradually strengthen with increasing temperature up to ~ 1920 °C, whereas the diffraction peaks of Th_3P_4 -type Hf_3N_4 gradually weaken and completely vanish at that temperature. It is obvious that a mixture of crystalline phases has been formed in the

temperature range from 1640 °C to 1920 °C. In order to investigate the phase transformation of Th₃P₄-type Hf₃N₄, the temperature was kept constant at ~1920 °C for about half an hour and a series of ED-XRD patterns were acquired during this time, which are shown in Figure 3. 16b. It can be observed that Th₃P₄-type Hf₃N₄ disappears after about 1000 s, and the diffraction peaks of rocksalt-type HfN show up at the same time, indicating the decomposition of Hf₃N₄ into rocksalt HfN. ED-XRD patterns of the sample after quenching the temperature at high pressure and decompression indicate that the phase transition of Hf₃N₄ into rocksalt HfN is irreversible because the decomposition reaction tends towards the stable phase. An additional XRD measurement (Figure 3. 17) of the recovered sample (#BT448) showed a mixture of γ -Si₃N₄ and HfN and only a tiny fraction of remaining Hf₃N₄ (0.1 wt%). The refined phase fractions are Si₃N₄ : HfN = 47 wt% : 6.6 wt%, corresponding to an atomic ratio of Si : Hf = 29 : 1, similar to the result from elemental analysis of the precursor (Si : Hf = 21 : 1). The rest of the phase fractions are the capsule material c-BN, which could not be completely separated from the samples.

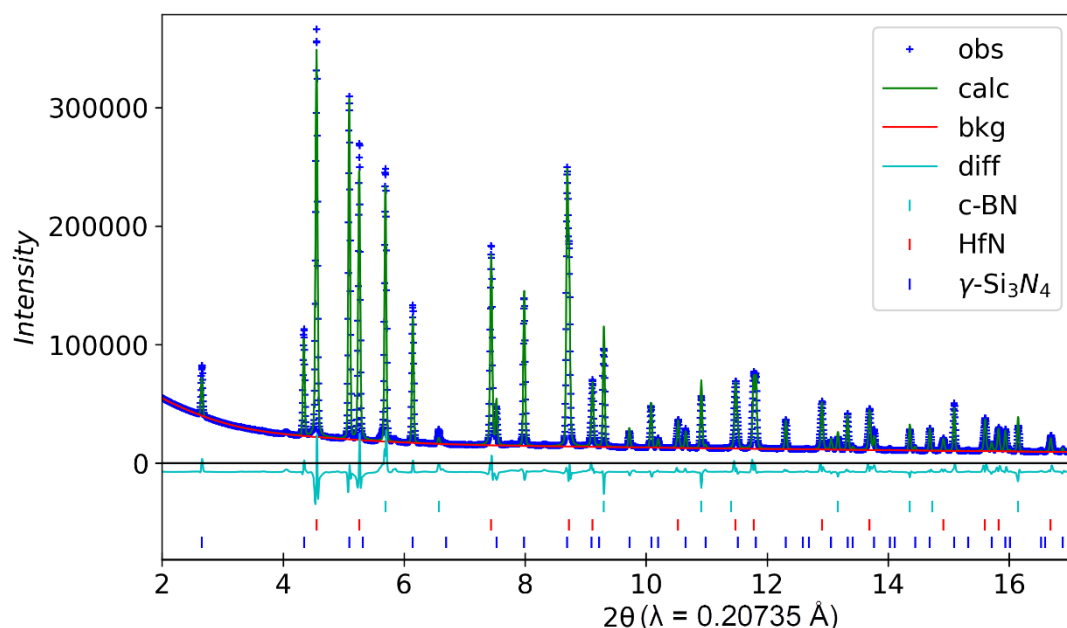
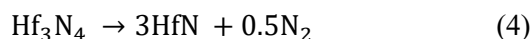


Figure 3. 17 Rietveld refinement of the AD-XRD powder pattern of SiHfN sample recovered from the HP-HT experiment after completing the ED-XRD measurements (The final residual is $wR = 7.3\%$).

As illustrated the phase diagram in Figure 3. 18, the amorphous SiHfN phase separates along the tie line into γ -Si₃N₄ and Hf₃N₄ at ~20 GPa and ~1090 °C. At temperature far beyond 1570 °C, Hf₃N₄ decomposes along the tie line into rock salt-type HfN and N₂ according to equation (4), which is then in thermodynamic equilibrium with γ -Si₃N₄.



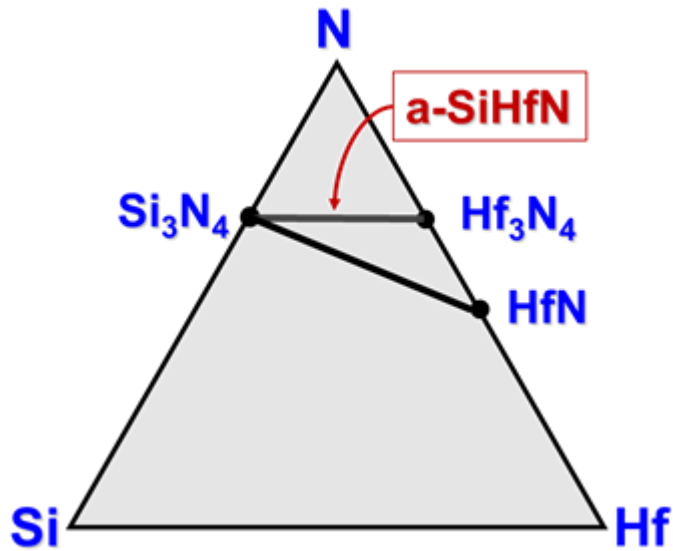


Figure 3. 18 Thermodynamic guideline for the synthesis of high-pressure nitride nanocomposites in the ternary SiHfN system.

3.2.2.3 Characterization of the γ -Si₃N₄/Hf₃N₄ composite

An AD-XRD powder pattern of the recovered sample #HH547 was measured using synchrotron radiation. Rietveld refinement (Figure 3. 19) showed essentially two phases, namely γ -Si₃N₄ and Hf₃N₄ and some small reflections of a yet unidentified third phase, resulting in a residual of wR = 9.6%. The refined phase fractions are Si₃N₄ : Hf₃N₄ = 24.4 wt% : 2.7 wt%, corresponding to an atomic ratio of Si : Hf = 38:1. Other reflections are from the capsule material c-BN, which could not be completely separated from the sample. This value is larger than that of the result from elemental analysis of the precursor (Si : Hf = 21:1), suggesting that the unknown third phase is rich in Hf.

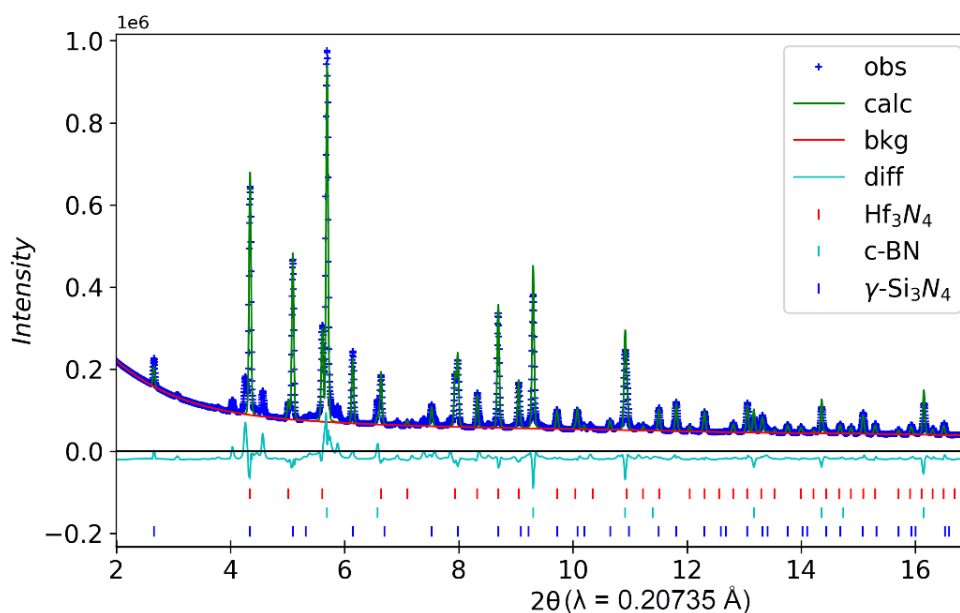


Figure 3. 19 Rietveld refinement of the γ - $\text{Si}_3\text{N}_4/\text{Hf}_3\text{N}_4$ composite, recovered from a HP-HT experiment at ~ 20 GPa and ~ 1500 °C.

The TEM images and SEM-EDS analysis of the resultant γ - $\text{Si}_3\text{N}_4/\text{Hf}_3\text{N}_4$ ceramic nanocomposite synthesized at ~ 20 GPa and ~ 1500 °C are shown in Figure 3. 20 and Figure 3. 21, respectively. Fig. 3. 20a and g indicate that the Hf_3N_4 grains/particles identified by the significant darker contrast are homogeneously dispersed in the γ - Si_3N_4 matrix. The microstructure of the γ - $\text{Si}_3\text{N}_4/\text{Hf}_3\text{N}_4$ ceramic nanocomposite has been studied through TEM images and SAED patterns as shown in Figure 3. 20b and Figure 3. 20c to identify the two phases. The SAED pattern with zone axis [001] in Figure 3. 20b shows the face-centered cubic lattice of the large γ - Si_3N_4 single crystal visible in the image and two representative reflections, (4 0 0) and (2 2 0), are denoted in the SAED pattern. The corresponding lattice spacings are 0.193 nm and 0.274 nm. The SAED image taken from the whole region in Figure 3. 20c exhibits a polycrystalline aggregate composed of Hf_3N_4 and γ - Si_3N_4 . Furthermore, in the HR-TEM image (Figure 3. 20e and f), the lattice plane (3 1 1) of γ - Si_3N_4 and the lattice plane (2 1 1) of Hf_3N_4 are also identified by the d-values of 0.233 nm and 0.274 nm, respectively. In addition, the existence of Hf_3N_4 in the γ - Si_3N_4 matrix can also be clearly seen from Figure 3. 20c, d, e and f. In Figure 3. 20f, dispersed Hf_3N_4 nanocrystallites are embedded in micron sized Si_3N_4 -particles. Furthermore, nanopores and amorphous interphase between Hf_3N_4 and γ - Si_3N_4 were observed as shown in Fig. 5g-i.

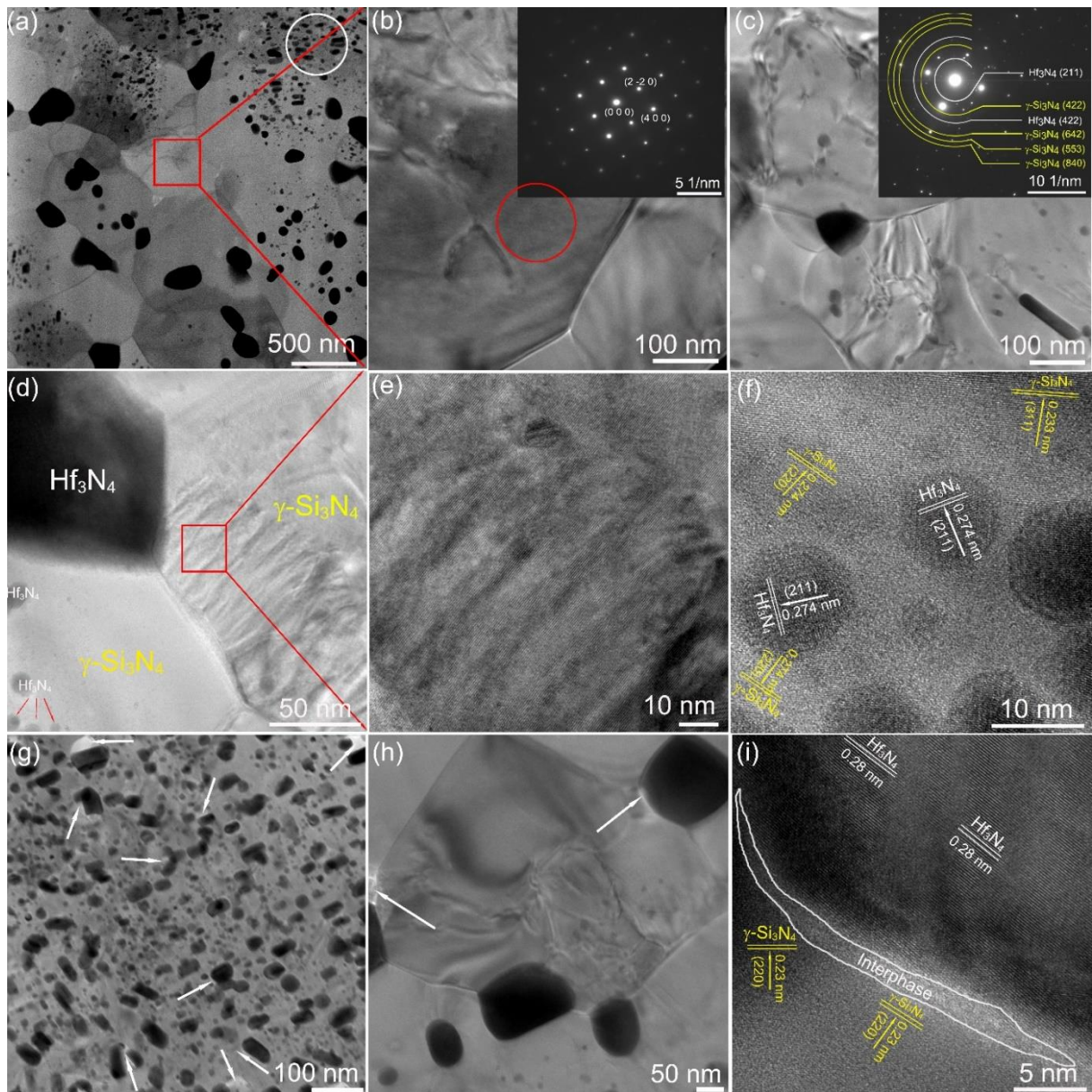


Figure 3. 20 TEM images of the γ - $\text{Si}_3\text{N}_4/\text{Hf}_3\text{N}_4$ nanocomposite synthesized at ~ 20 GPa and ~ 1500 $^\circ\text{C}$. (a) TEM image of a typical microstructure of the γ - $\text{Si}_3\text{N}_4/\text{Hf}_3\text{N}_4$ nanocomposite. (b) TEM image acquired from a, the inset is a SAED image taken from the red box region. (c) TEM image and corresponding SAED image. (d) TEM image shows grain boundaries between Hf_3N_4 and γ - Si_3N_4 crystals. (e) HR-TEM micrograph magnified from the red box area in d, showing lattice fringes from an imperfect γ - Si_3N_4 single crystal with some embedded nanospheres of Hf_3N_4 . (f) Hf_3N_4 nano particles embedded in γ - Si_3N_4 . (g) TEM image obtained from the white circled area in image a, the white arrows represent nanopores. (h) HR-TEM image shows the interaction relationship between γ - Si_3N_4 , Hf_3N_4 nanograins and nanopores. (i) HR-TEM micrograph magnified from the interphase area.

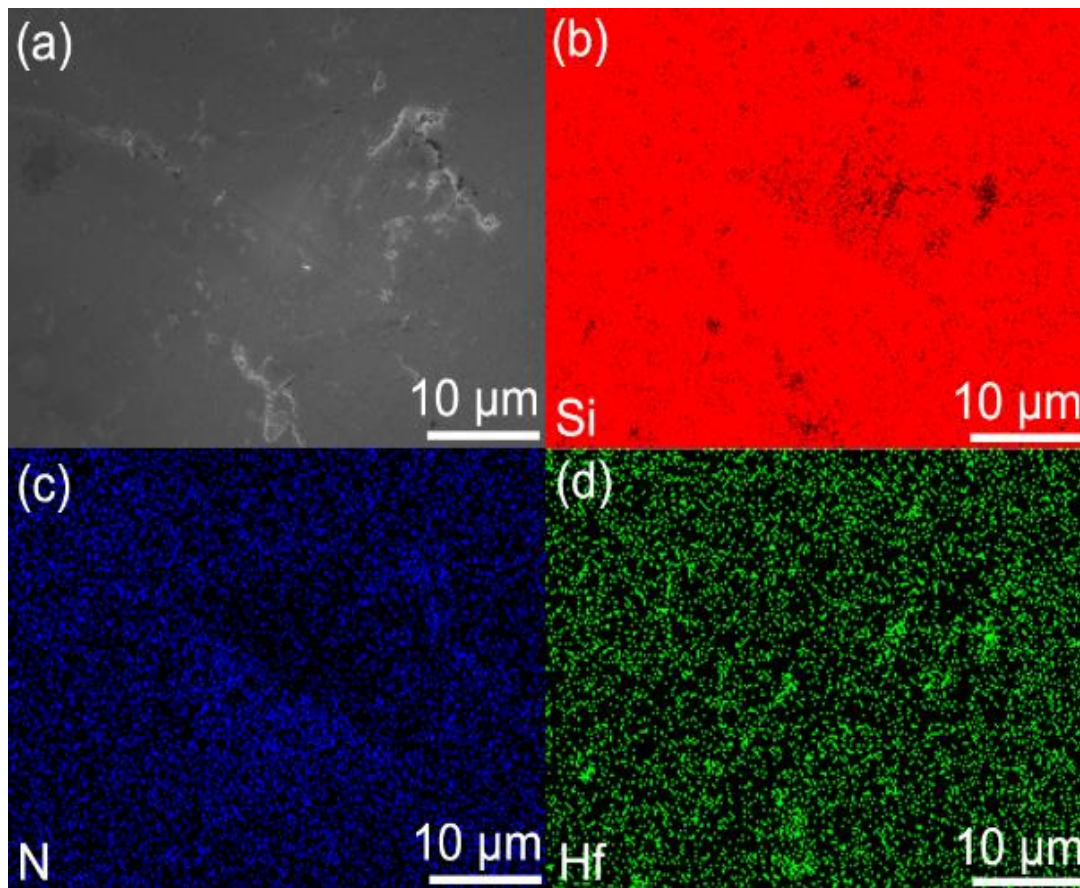


Figure 3. 21 SEM graph and elemental mappings of the γ -Si₃N₄/Hf₃N₄ ceramic nanocomposites, indicating homogeneous Si, Hf, and N elemental distributions.

3.2.2.4 Mechanical properties

Vickers hardness and fracture toughness of the γ -Si₃N₄/Hf₃N₄ nanocomposites were measured at indentation loads from 0.49 N to 19.6 N on a polished surface. As can be seen from Figure 3. 22, the Vickers hardness and the fracture toughness of γ -Si₃N₄/Hf₃N₄ decrease with increasing load. Although the Vickers hardness of Hf₃N₄ (18.7 GPa) [262] is lower than that of γ -Si₃N₄ (43 GPa) [2, 263], an average hardness value of 27.8 ± 2.0 GPa for the γ -Si₃N₄/Hf₃N₄ composite is achieved at an applied load of 9.8 N, which is comparable to the Vickers hardness of γ -Si₃N₄, stishovite SiO₂ (33 GPa) [264, 265] and γ -Ge₃N₄ (28 GPa) [266], and is much higher than that of the experimental and theoretical hardness values of transition metal nitrides, such as Hf₃N₄ [262], Zr₃N₄ [262, 267], NbN [268], γ -MoN [269], HfN [268], and ZrN [268].

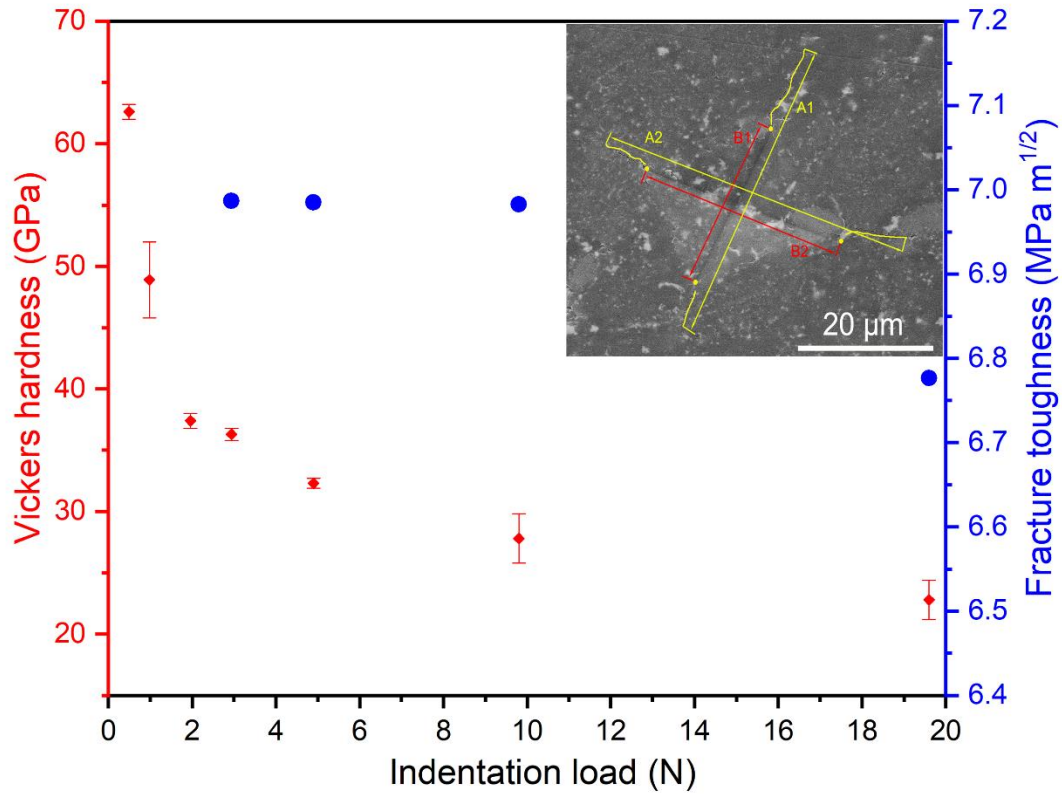


Figure 3. 22 Hardness and fracture toughness of the γ -Si₃N₄/Hf₃N₄ nanocomposite as a function of indentation loads in the range of 0.49 N–19.6 N. The inset is a representative SEM indentation image showing cracks under an indentation load of 19.6 N.

No cracks are observed from the indentation trace (Figure 3. 23 a, b, c) when the applied load is less than 2.94 N. Therefore, the fracture toughness (Figure 3. 22) of the γ -Si₃N₄/Hf₃N₄ ceramic nanocomposite at 2.94 N, 4.9 N, 9.8 N, and 19.6 N is estimated based on the relation between indentation load and the radius/length of cracks. The fracture toughness decreases with increasing indentation load showing an average value of 6.93 MPa·m^{1/2}, which is twice as much as that of pure γ -Si₃N₄ (3.5 MPa·m^{1/2}) [25]. The toughening mechanism of γ -Si₃N₄/Hf₃N₄ ceramic nanocomposite is discussed in terms of the transgranular fracture mode [270, 271] as can be seen from Figure 3. 23d. Moreover, the presence of nano-sized grains in the γ -Si₃N₄/Hf₃N₄ composite can cause an increase of the fracture toughness due to crack deflection and bridging of the composite with low-stiffness interface [272].

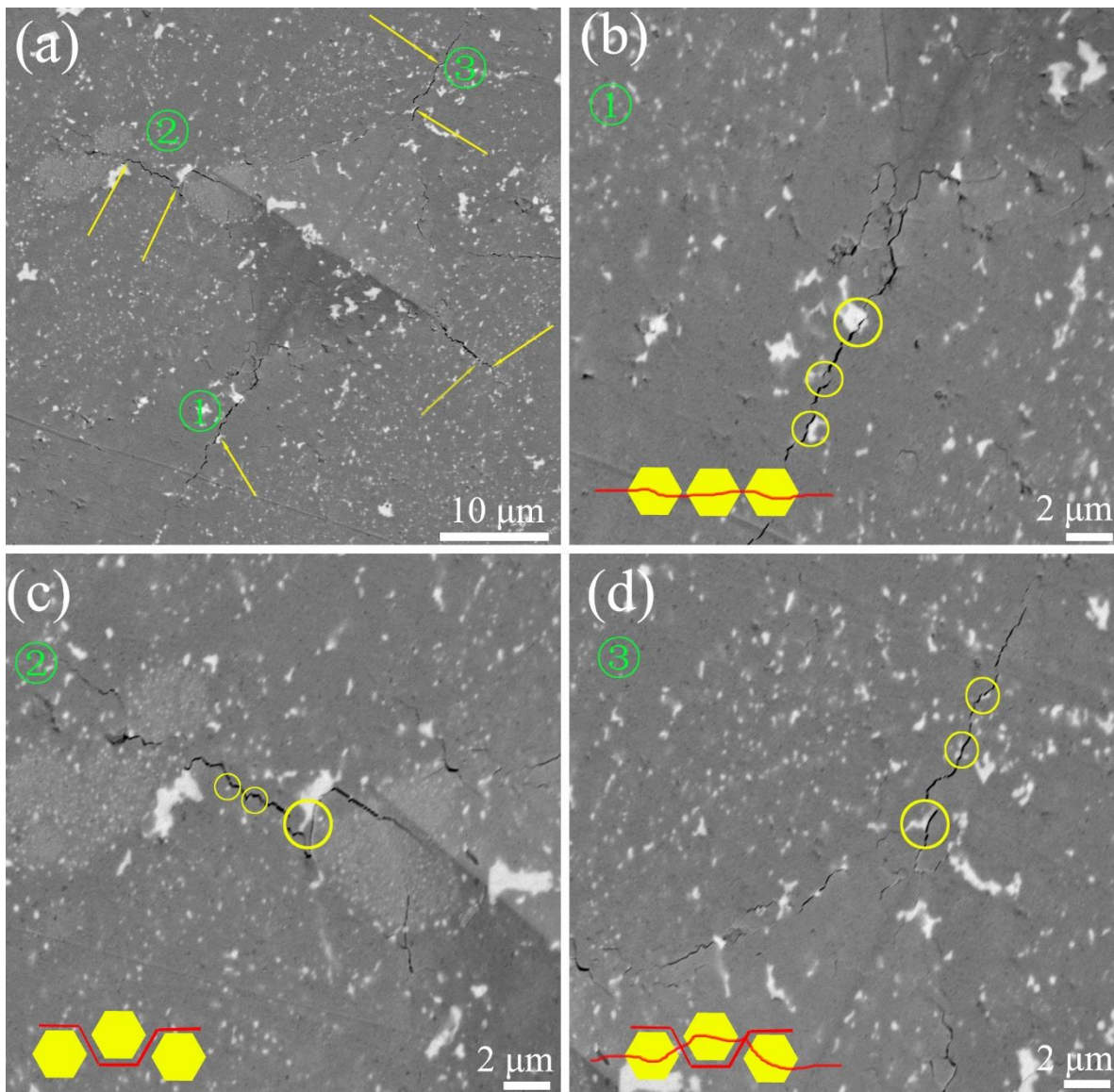


Figure 3.23 SEM image of the indentation and cracks at 9.8 N, yellow arrows indicate transgranular cracks. Insets are the simulation path of crack propagation (The hexagons show the grain, and the red color represents the crack).

In order to comprehensively evaluate the Vickers hardness and the fracture toughness of the γ - $\text{Si}_3\text{N}_4/\text{Hf}_3\text{N}_4$ nanocomposite, a comparison with other hard materials is compiled and shown in Fig. 7 [25, 273-288]. Accordingly, the resultant γ - $\text{Si}_3\text{N}_4/\text{Hf}_3\text{N}_4$ ceramic composite exhibits both high hardness and fracture toughness simultaneously, which is an excellent trade-off between hardness and fracture toughness compared to most other materials. Therefore, the high-pressure γ - $\text{Si}_3\text{N}_4/\text{Hf}_3\text{N}_4$ nanocomposite is considered to be a potential candidate material for cutting tool applications.

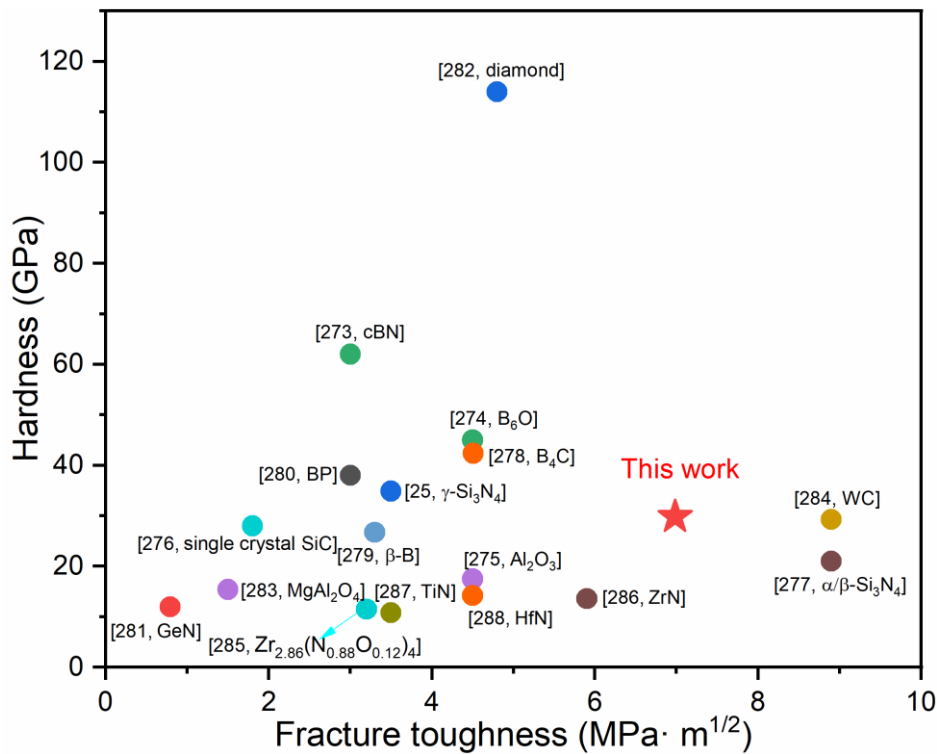


Fig. 7 Vickers hardness and fracture toughness of the γ -Si₃N₄/Hf₃N₄ nanocomposite (load: 9.8 N) in comparison with reported hard materials.

3.2.3 Conclusions

Within the present work, the phase transformation of amorphous SiHfN ceramic prepared by the PDC route under HPHT conditions is investigated by means of synchrotron X-ray diffraction measurements. The results provide clear guidance for the preparation of high-pressure γ -Si₃N₄/Hf₃N₄ and γ -Si₃N₄/HfN ceramic nanocomposites. Based on in-situ XRD analysis, the γ -Si₃N₄/Hf₃N₄ ceramic nanocomposite is obtained at ~1500 °C and ~20 GPa. At temperatures beyond 1500 °C under the same pressure, the Hf₃N₄ phase decomposes to hafnium mononitride and a γ -Si₃N₄/HfN composite is formed.

The fracture toughness of the resultant γ -Si₃N₄/Hf₃N₄ ceramic nanocomposite (~7 MPa m^{1/2}) exhibits a significant improvement over pure γ -Si₃N₄ (3.5 MPa m^{1/2}) without sacrificing the hardness of the material. Characterizations by means of XRD, SEM, and TEM proved that the enormous enhancement (2 times) in the fracture toughness has to be discussed in terms of synergetic effects of nano-scale composite (γ -Si₃N₄ ≤ 200 nm, Hf₃N₄ ≤ 50 nm) and transgranular fracture mode. In addition to the unique combination of high hardness and high toughness, the γ -Si₃N₄/Hf₃N₄ nanocomposite can be operated in extreme environments and at elevated temperature as the two individual high pressure nitride phases γ -Si₃N₄ and Hf₃N₄ have been shown to be high temperature resistant.

3.3 Single-source-precursor derived bulk $\text{Si}_3\text{N}_4/\text{HfB}_x\text{N}_{1-x}$ ultra-high temperature ceramic nanocomposites

The content of this Chapter is published in:

1. **Li W**, Du H, Tian C, et al. Single-source-precursor derived bulk $\text{Si}_3\text{N}_4/\text{HfB}_x\text{N}_{1-x}$ ceramic nanocomposites with excellent oxidation resistance [J]. *Zeitschrift für anorganische und allgemeine Chemie.*, 2022.

In this chapter, the SiHf(B)N single-source precursors with varied compositions were synthesized by chemical modification of PHPS with TDMAH and BMS. The chemical reactions between Si–H and N–H groups of PHPS and BMS and TDMAH were confirmed by FT-IR and XPS. Then, the polymer-to-ceramic transformation of the single-source precursors was investigated via the cross-linking and pyrolysis by TGA/DTA, FTIR and XPS. Subsequently, the conversion of amorphous to crystalline reveals that the modification with hafnium and boron not only increases the ceramic yield of the final products but also efficiently improves the high-temperature stability of the PHPS-derived Si_3N_4 against crystallization greatly. Finally, the oxidation behavior of the resultant SiHf(B)N ceramics was investigated, and the effect of B/Hf incorporation on the oxidation resistance was carefully discussed.

3.3.1 Experimental procedures

3.3.1.1 Synthesis and pyrolysis of the single-source precursors

All chemical synthesis processes were carried out under purified argon atmosphere (Argon-filled Glovebox and Standard Schlenk technique) to keep inert environment, and anhydrous toluene (Merck, Germany) was used as a reaction solvent. Commercially available PHPS solution, TDMAH, and BMS were used as the starting materials to synthesize Hf/B- containing single-source precursors. The modification of PHPS with different TDMAH contents was reported in our previous work [19], in which the optimized ratio of TDMAH and PHPS was determined to be 3:7. Therefore, for the synthesis of Hf/B-modified single-source precursors, the weight ratio of TDMAH to PHPS was set to 3:7, and the amount of BMS added to the Hf-modified PHPS was adjusted according to B/Hf molar ratios of 2:1, 5:1, 10:1. The synthesized single-source precursors are denoted as BHPSY (Y is the B/Hf molar ratio). Here, a typical synthesis process of the BHPS2 was carried out as follows: 1 g TDMAH dissolved in 10 mL anhydrous toluene was added dropwise into a solution of 11.25 g PHPS (2.3 g pristine PHPS) with stirring at room temperature for 2 h. Then, a solution of BMS (2.4 mL, 25 mmol) in anhydrous toluene (10 mL) was added dropwise into the mixture of TDMAH and PHPS under stirring at ≈ -78 °C (dry ice/acetone bath). The mixture was stirred at ≈ -78 °C for 2 h and then naturally warmed up to room temperature. After continuous stirring for 24 h, the synthesized mixture was heated at 80 °C for 3 h followed by vacuum drying (10^{-2} mbar) at 50 °C for 5 h to yield the solid single-source precursor BHPS2.

The resultant BHPSY single-source precursors were warm-pressed at 110 °C and 120 MPa. In order to investigate the polymer-to-ceramic transformation of the warm-pressed BHPSY pellets and the high temperature behavior of the resulting SiHfBN ceramics, the obtained precursor was transferred into a horizontal Schlenk tube and pyrolyzed at 1000 °C for 2 h at a heating rate of 50 °C/h under NH₃ atmosphere, and then cooling down to room temperature at 100 °C/h. Subsequently, the as-pyrolyzed specimens were annealed at 1300 °C, 1500 °C and 1700 °C for 2 h in N₂ atmosphere. In the subsequent discussion, the synthesized precursors and the annealed SiHfBN ceramics are denoted as expressed in Table 3. 4.

Table 3. 4 Composition, preparation temperatures and notation of the synthesized BPSZX, BHPSY precursors and SiHfBN-based bulk samples.

Notation	Samples	Molar ratio	Temperature (°C)
BHPSY	BHPS2	2:1 (B:Hf)	80
	BHPS5	5:1 (B:Hf)	80
	BHPS10	10:1 (B:Hf)	80
SiHfBN_1000	SiHfBN2_1000	2:1 (B:Hf)	1000
	SiHfBN5_1000	5:1 (B:Hf)	1000
	SiHfBN10_1000	10:1 (B:Hf)	1000
SiHfBN_1300	SiHfBN2_1300	2:1 (B:Hf)	1300
	SiHfBN5_1300	5:1 (B:Hf)	1300
	SiHfBN10_1300	10:1 (B:Hf)	1300
SiHfBN_1500	SiHfBN2_1500	2:1 (B:Hf)	1500
	SiHfBN5_1500	5:1 (B:Hf)	1500
	SiHfBN10_1500	10:1 (B:Hf)	1500
SiHfBN_1700	SiHfBN2_1700	2:1 (B:Hf)	1700
	SiHfBN5_1700	5:1 (B:Hf)	1700
	SiHfBN10_1700	10:1 (B:Hf)	1700

3.3.1.2 Characterization

The synthesized single-source precursors and their cross-linking process were analyzed by means of attenuated total reflection-Fourier transform infrared (ATR-FTIR) spectroscopy in the range of 550 – 4000 cm⁻¹ on a Varian IR-670 instrument (Agilent Technologies, USA). The polymer-to-ceramic

transformation of the BPSZX precursor was characterized by means of thermogravimetric analysis/differential thermal analysis (TGA/DTA) in flowing nitrogen atmosphere with an STA 449C Jupiter (Netzsch Gerätebau GmbH, Germany) in situ coupled with a mass spectrometer (MS, QMS 403C Aëolos, Netzsch Gerätebau GmbH, Germany). The polymer-to-ceramic conversion of the BHPSY precursor was recorded by a thermal analysis device (STA 449F3 Jupiter, Netzsch, Germany) in flowing nitrogen and ammonia atmosphere (10 vol.% Ar in NH₃; Ar >99.999 %, Tyczka Industrie-Gase GmbH, purified by Entegris Gatekeeper GPUS IX p(O₂) < 100 ppt, p(H₂O) < 100 ppt; NH₃ >99.999 %, Air Liquide, purified by Entegris Gatekeeper GPUS YX p(O₂) < 1 ppb, p(H₂O) < 1 ppb) from room temperature to 110 °C for 2 h, and then heated to 1100 °C at a heating rate of 5 °C/min. The measurements were corrected for the buoyancy. The phase identification of the ceramic samples was performed on a powder X-ray diffraction diffractometer utilizing Mo *Kα1* radiation source (STOE & Cie GmbH, Germany) in transmission geometry. Transmission electron microscopy coupled with the selected area electron diffraction technique were done on a JEM-2100 microscope (JEOL Ltd, Tokyo, Japan) under an acceleration voltage of 200 kV to investigate the microstructures and phase distribution of the Si(Hf)BN ceramics. The chemical bonding of the BHPS5 precursor and samples heat-treated at different temperatures (25 °C, 400 °C and 1000 °C) were characterized by in-line UHV integrated XPS (SPECS) with a hemispherical energy analyzer (PHOIBOS 150, Focus 500 with XR50M) at a pressure <5 × 10⁻¹⁰ mbar. Monochromatized Al *Kα* line (1486.74 eV) was used as the X-ray source. Survey spectra were recorded with a pass energy of 25 eV and a step width of 1 eV, and detailed spectra were recorded with 10 and 0.05 eV, respectively. The obtained spectra were analyzed with the software CasaXPS to employ Shirley background correction and Gaussian-Lorentzian peak fitting, adjusting the binding energy position, peak intensity, and full width at half maximum values.

3.3.1.3 Oxidation tests

The monolithic SiHfBN samples prepared by warm-pressing of the precursor powder and subsequent pyrolysis of the green body were polished with diamond paste to μm roughness, and the polished samples were ultrasonically cleaned in acetone and dried at 100 °C for 24 h in an oven. The skeletal density and open porosity of the pellets were determined by the Archimedes method. The oxidation behavior of SiHfBN_1700 monoliths was performed in a muffle furnace at 1500 °C. The oxidation times of the monolithic samples amounted from 1 h to 50 h and the weight changes were measured with an analytical balance (with an accuracy of ±0.01 mg) at specific interval times.

3.3.2 Results and Discussion

3.3.2.1 Synthesis of the single-source precursors

The FTIR spectra of BMS, pristine PHPS, and the obtained boron modified PHPS (BPSZX, X is molar ratio of Si:B) precursors are shown and compared in Figure 3. 24. Typical absorption bands of N-H (1120, 3302 cm⁻¹), Si-H (2159 cm⁻¹), and Si-N-Si (830 – 1050 cm⁻¹) groups are expectedly shown in

the FTIR spectrum of PHPS. With the addition of BMS into PHPS, the N–H and Si–H groups of PHPS and the B–H (2391 cm^{-1}) groups of BMS are consumed, while B–N groups (1315 cm^{-1}) are formed simultaneously, as shown in the spectra of BPSZX precursors. Hence, dehydrocoupling reactions between the N–H (Si–H) and B–H groups are proposed as reaction mechanisms and are shown schematically in Figure 3. 25. Unlike the N–H groups, which are reacted in a high amount, only a small number of the Si–H groups are involved in the modification process. It was reported by Hapke et. al [289] that the reaction of Si–H groups is affected by steric hindrance during the chemical modification of the PHPS. Additionally, the existence of B–H (1091 cm^{-1}) groups in BPSZ1 and BPSZ2 reveals that the silazane-bonded B–H groups have not been completely reacted. The C–H vibrations ($2786 - 2995\text{ cm}^{-1}$) detected in the spectra of the BPSZX samples stem from the residual solvent dibutyl ether.

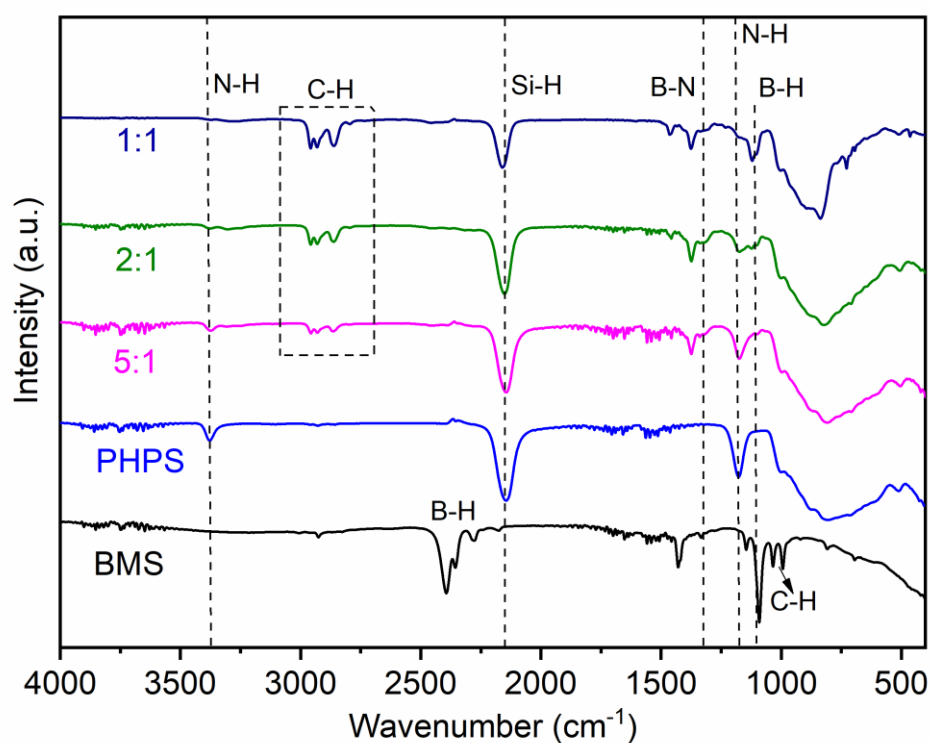


Figure 3. 24 FTIR spectra of BMS, pristine PHPS, BPSZ5, BPSZ2 and BPSZ1.

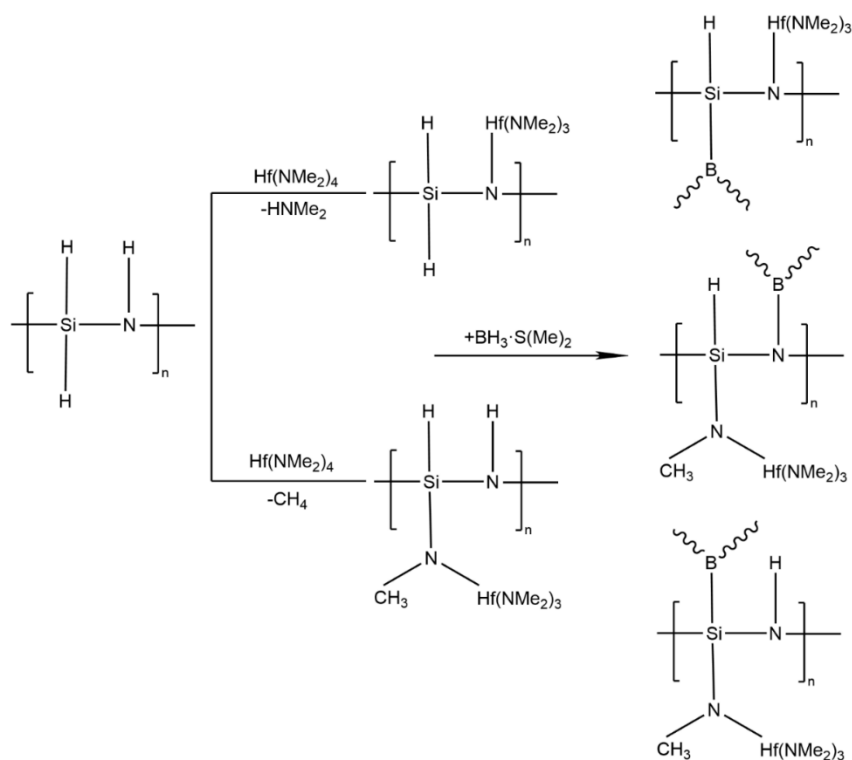


Figure 3. 25 Proposed pathway of the reaction of PHPS with TDMAH and BMS.

Based on the above investigation of SiHfN (chapter 3.1 and 3.2) and SiBN precursors, a series of SiHfBN precursors with different B/Hf molar ratios were synthesized and investigated by means of FT-IR and XPS. The FT-IR spectra of TDMAH, pristine PHPS, BMS, as well as the synthesized BHPSY precursors are shown in Figure 3. 26. In the FT-IR spectrum of PHPS, typical absorption bands related to Si-H (2159 cm^{-1}), N-H ($1120, 3302\text{ cm}^{-1}$), and Si-N-Si ($840 - 1050\text{ cm}^{-1}$) groups are expectedly observed. The absorption bands at 1088 cm^{-1} and $2260 - 2534\text{ cm}^{-1}$ are characteristic vibrations of BMS and are assigned to B-H units. The peaks appearing at 940 and 1246 cm^{-1} are related to the stretching vibration modes of Hf-N-C in TDMAH. As can be seen from the spectra of the BHPSY precursors, the intensity of the peaks related to Si-H and N-H groups becomes smaller with the addition of BMS and TDMAH into PHPS, while the peak intensity of B-N (1315 cm^{-1}) gradually increases. Furthermore, the presence of the B-N peak (401.8 eV) in the XPS spectra (Figure 3. 27c) of the N 1s line also confirms that B atoms exist in the N substitutional sites of Si-N [290], indicating that dehydrocoupling reactions occur between N-H and Si-H groups of PHPS and B-H of BMS. Additionally, in the Si 2p XPS spectrum (Figure 3. 27d), a signal at 222 eV is assigned to rich silicon in precursor [19], which is consistent with the reported results and plays a great role in the polymer-to-ceramic transformation. The disappearance of absorption bands related to B-H groups as well as to Hf-N-C bonds in the BHPSX precursors (Figure 3. 26) indicates that all B-H groups of BMS and all Hf-N-C groups of TDMAH are involved in the reaction. The weaker bands at $2786 - 2995\text{ cm}^{-1}$ in the FT-IR spectra (Figure 3. 26) are ascribed to C-H vibrations of sp^3 carbon of the methyl groups in TDMAH. C-N, C-C and C-NH units

are also found in the XPS spectra of the C 1s signal (Figure 3. 27b) [14]. This residual carbon source is attributed to the residual solvent toluene and dibutyl ether, and is removed after pyrolysis under NH_3 as discussed in the next section.

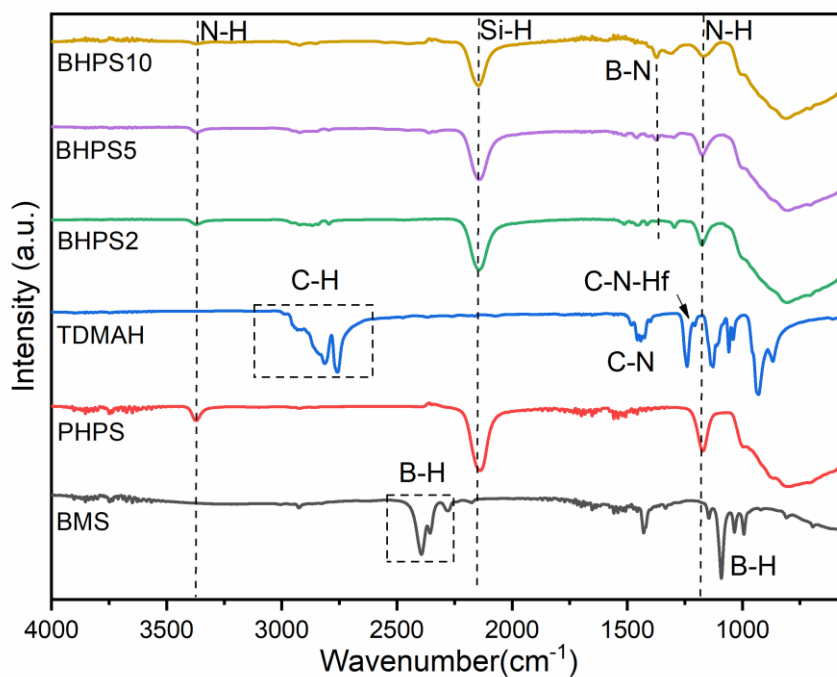


Figure 3. 26 FT-IR spectra of BMS, PHPS, TDMAH, and BHPSY precursors.

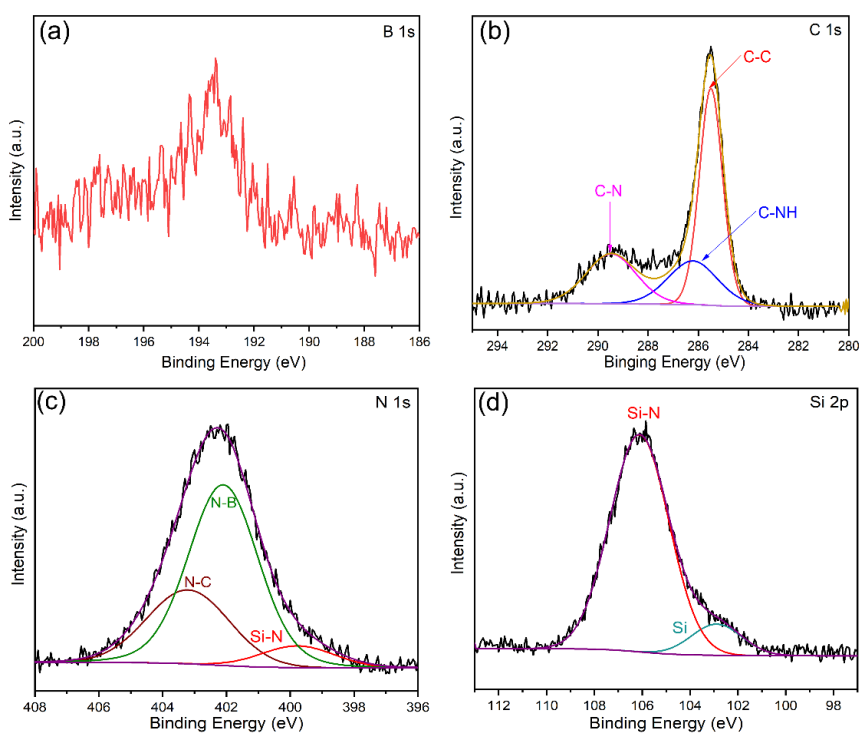


Figure 3. 27 XPS spectra of BHPS5 precursor (a) B 1s; (b) C 1s; (c) N 1s; (d) Si2p.

The reaction between PHPS and TDMAH and BMS is schematically shown in Figure 3. 25 and is based on spectroscopic studies [19, 291]. Similar chemical reaction of both Si–H and N–H groups with BMS and the hafnium amido complex was reported in our previous work [291]. Unlike the N–H groups, only a small amount of the Si–H groups react (see Figure 3. 26), which is discussed in terms of steric hindrance [19, 291].

3.3.2.2 Polymer-to-ceramic conversion

The polymer-to-ceramic transformation of the BHPSY single-source precursors was investigated by means of TGA/DTA and FT-IR measurements. As shown in the TGA/DTA curves (Figure 3. 28), the BHPSY precursors exhibit four regions of mass changes. The first two steps from RT to ≈ 200 °C show an overall weight loss of 4.8 wt%, while the third step, 200 to ≈ 450 °C, is characterized by a significant increase in mass up to ca. 107 wt%. The last step at temperatures beyond 400 °C corresponds to the ammonolysis resulting in the final ceramic yield, which amounts 100.4 wt%, 100.8 wt% and 101.6 wt% for the BHPS2, BHPS5 and BHPS10 precursors, respectively.

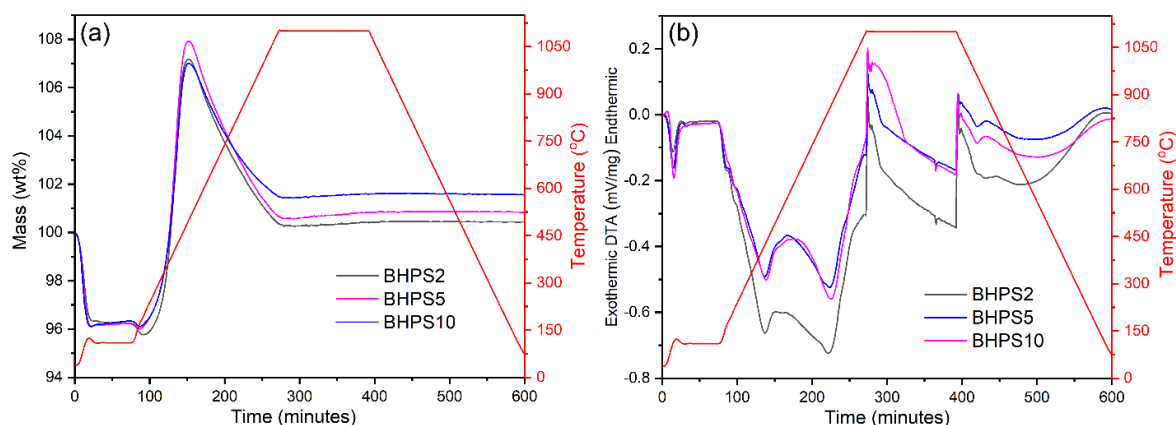


Figure 3. 28 TG (a), DTA (b) and temperature vs time curves of the BHPSY precursor under flowing ammonia/argon atmosphere (90 vol.% NH_3)

The weight loss of 2.8 wt% in step 1 and 2 is ascribed to the evaporation of residual solvent, moisture and unreacted organic chains. Additionally, the exothermic peaks at ca. 110 °C (Figure 3. 28b) indicate typical dehydrocoupling cross-linking reactions with bond redistribution and thermal decomposition, leading to additional weight loss. However, the weight loss of BHPSY precursors at ≈ 200 °C is lower than that of the Hf- and B-free PHPS (13.9 wt%), which is considered to be related to the higher degree of cross-linking of the Hf- and B-modified precursor. The cross-linking reactions are supported by the FT-IR spectra (Figure 3. 29), where the N–H and Si–H absorption peaks almost vanish with increasing temperature up to 400 °C. The exothermic peak and mass gain in step 3 should be due to the reaction of the polymeric precursor with ammonia. In reactive ammonia atmosphere, excess silicon found in PHPS is terminated by NH_x -groups which readily react with TDMAH to form Si–N–Hf linkages at around 300 °C [239]. The XPS spectrum (Figure 3. 30) of the SiHfBN5 sample heat-treated at 400 °C shows

that all expected bonds such as C–N, C–C and C–NH for carbon, N–C, N–B and Si–N for nitrogen and Si–N and elemental Si for silicon were detected, indicating that polymer-to-ceramic transformation requires higher heat treatment temperature.

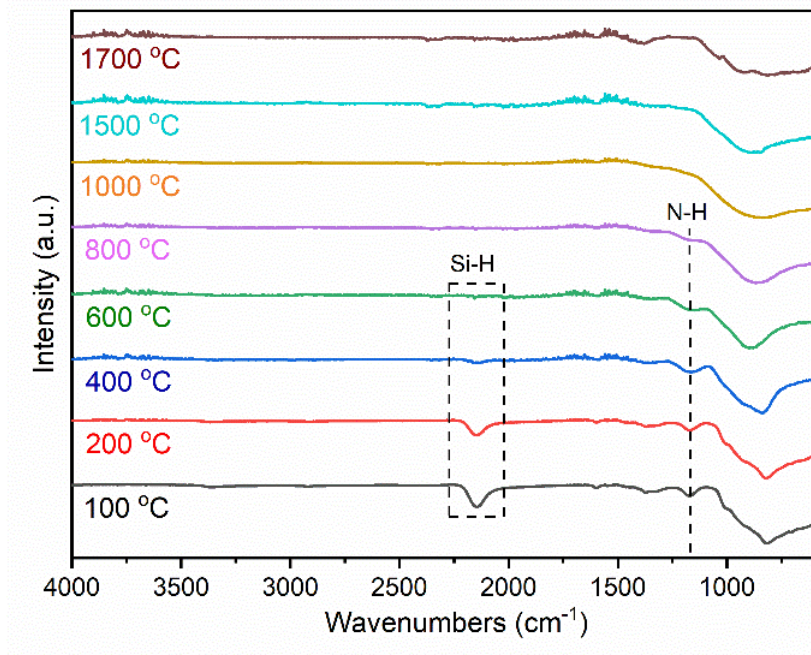


Figure 3. 29 FT-IR spectra of BHPS5 annealed at different temperatures.

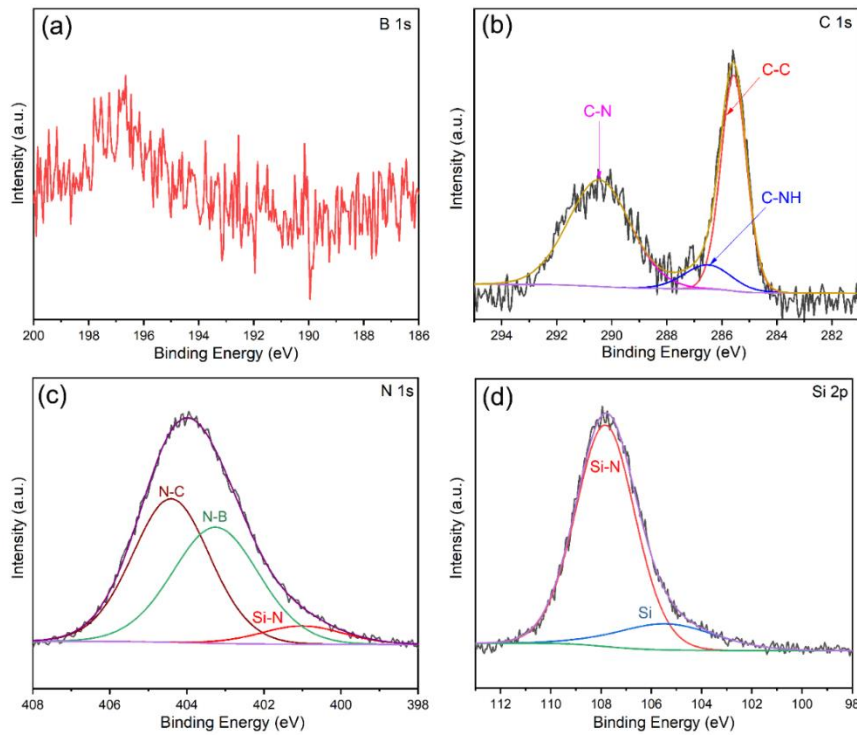


Figure 3. 30 XPS spectra of SiHfBN5 sample heat-treated at 400 °C (a) B 1s; (b) C 1s; (c) N 1s; (d) Si 2p.

The weight loss in the last step is ascribed to transamination and polycondensation reactions with the release of volatile dimethylamine and ammonia [241]. The disappearance of C signals in the C 1s XPS spectrum (Figure 3. 30) of the obtained ceramics provides clear evidence that carbon is totally consumed during pyrolysis in the presence of ammonia. In Figs. 3 1a and 3 1c, the B 1s and N 1s XPS spectra exhibit a prominent chemical signals at 191.1 eV and 399.9 eV, respectively, which are attributed to Hf bonded to B and N [292]. Furthermore, the ceramization process is supported by the FT-IR spectra (Figure 3. 29), where the absorption peaks of Si–H and N–H completely vanish beyond 600 °C and 800 °C, respectively. The final ceramic yield of BHPSX is around 100.5 wt%, which is higher than those of the pristine PHPS (78 wt%), boron-modified PHPS (93 wt%) and hafnium-modified PHPS (97 wt%). The significant improvement of the ceramic yield has been associated with the presence of HfN_x and BN_x regions, which are more stable concerning their decomposition than that of the SiN_x regions [19]. In addition, the HfN_x- and BN_x-phases are discussed to encapsulate the SiN_x-rich regions and suppress their decomposition [41].

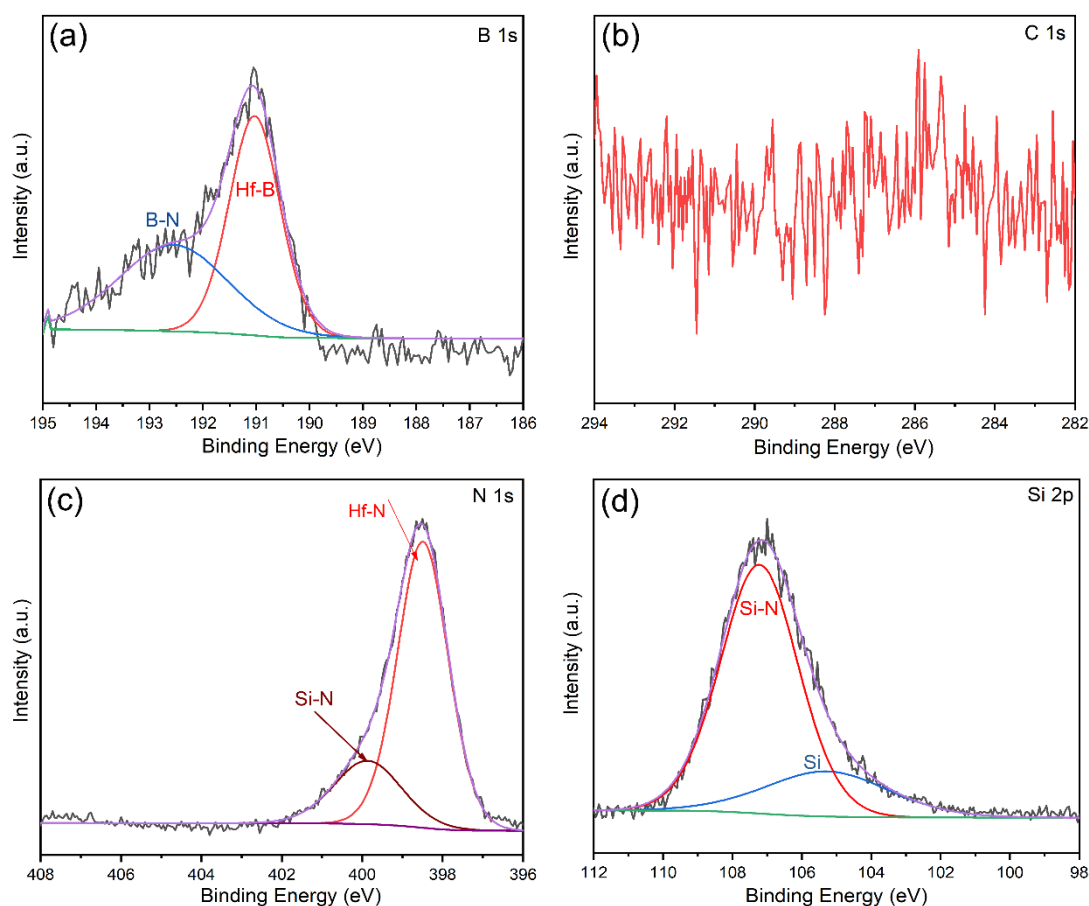


Figure 3. 31 XPS spectra of SiHfBN5 sample pyrolyzed at 1000 °C (a) B 1s; (b) C 1s; (c) N 1s; (d) Si 2p.

3.3.2.3 Microstructural characterization

3.3.2.3.1 XRD analysis

The high temperature behavior with respect to crystallization, phase composition as well as microstructural evolution of the heat-treated SiHfBN specimens at 1000 °C, 1300 °C, 1500 °C and 1700 °C was investigated via a combination of XRD and HRTEM. In Figure 3. 32, XRD patterns of the SiHfBN ceramics obtained upon pyrolyzing/annealing at different temperatures are presented. All of the BHPSY precursors pyrolyzed at 1000 °C and subsequently annealed at 1300 °C in nitrogen are predominantly X-ray amorphous (Figure 3. 32a, b). The SiHfBN ceramics with a molar ratio of B:Hf = 5 and 10 in the feed, still remain X-ray amorphous at 1500 °C, while crystallization of the SiHfBN2_1500 ceramic is significantly advanced, showing broad, low-intensity reflections of α -Si₃N₄ (Figure 3. 32c).

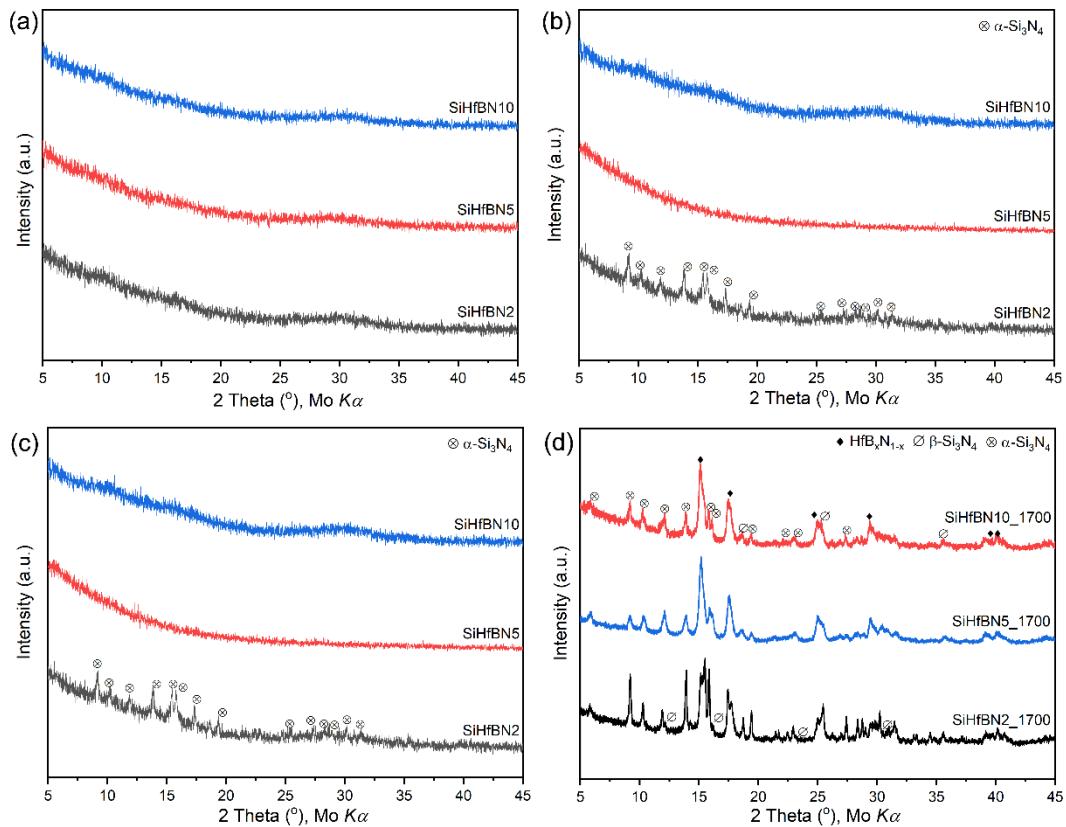


Figure 3. 32 XRD patterns of SiHfBN ceramics upon heat treatment in the temperature range of 1000–1700 °C under different atmospheres: (a) 1000 °C (NH₃), (b) 1300 °C (N₂), (c) 1500 °C (N₂), (d) 1700 °C (N₂).

As the annealing temperature is raised up to 1700 °C, all the amorphous SiHfBN samples undergo crystallization processes and phase separation. Figure 3. 32d represents the XRD patterns of three SiHfBN samples with different B:Hf ratio. They all show reflections from the dominating phase α -Si₃N₄, whereas the amount of β -Si₃N₄ is small and only the strongest β -Si₃N₄ reflections are visible as tiny peaks (indicated in the lower pattern of Figure 3. 32d). Additional reflections, not attributed to one of the Si₃N₄ polymorphs, are visible in the 2 θ ranges around 15°, 17°, 25°, and 30°, representing the contribution of Hf containing phases, which show an increase in intensity with increasing B:Hf ratio with respect to that of α -Si₃N₄. A quantitative phase analysis of the SiHfBN2_1700 XRD pattern by

Rietveld refinement, using GSAS-II [237] allowed to identify a mixture of three cubic NaCl-type phases (space group Fm-3m) with lattice parameters of 4.515 Å, 4.546 Å, and 4.598 Å. They are attributed to ternary Hf(B, N) phases, solid solutions of rock salt-type HfN and HfB, with different B:N ratio. The observed range of lattice parameters compares well with the reported values for HfN with $a = 4.526$ Å [293] or $a = 4.5101$ Å [294] and for HfB with $a = 4.65$ Å [295] or $a = 4.62$ Å [296]. The resulting Rietveld refinement is shown in Figure 3.33. The intensity distribution in the region of the Hf(B, N) reflections shows some fine structuring, which cannot be described by just one Hf(B, N) phase with a corresponding larger line width. This finding indicates an inhomogeneous B/N distribution across the sample. The refined phase fractions of α -Si₃N₄, β -Si₃N₄, and Hf(B, N)-1/ -2/ -3 are analyzed to amount 88.0/5.3/2.7/2.5/1.5 wt%, $wR = 7.1$ %.

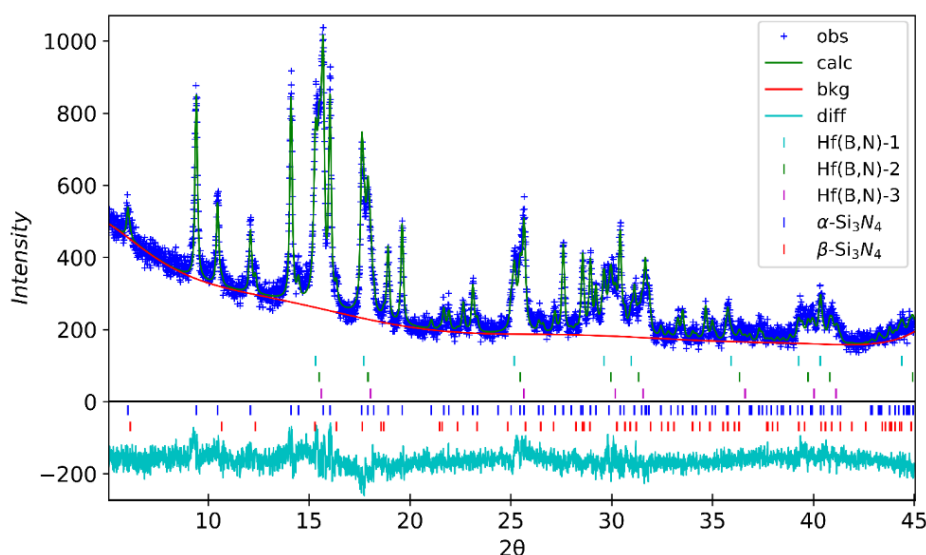


Figure 3. 33 Rietveld refinement of SiHfBN2_1700 XRD pattern.

3.3.2.3.2 TEM characterization

The crystallization behavior and microstructural development of SiHfBN5 prepared under different temperatures ranging from 1000 °C to 1700 °C are also supported by means of TEM investigations along with SAED (Figure 3. 34 and Figure 3. 35). In accordance with the XRD results (Figure 3. 32), the samples SiHfBN5_1000 and SiHfBN5_1300 are amorphous as shown by the featureless SAED pattern of the TEM images (Figure 3. 34).

After annealing at 1500 °C, contrast variations in Figure 3. 35a indicate that phase separation in sample SiHfBN5 takes place at 1500 °C, where small crystals of HfB_xN_{1-x} were found to be homogeneously dispersed throughout the matrix. Lattice fringes of the poorly crystallized HfB_xN_{1-x} nanograins can be identified in the high-resolution image in Figure 3. 35b. Although Si₃N₄ crystallites were not visualized in Figure 3. 35b and in the XRD patterns in Figure 3. 32c, the SAED pattern (Figure 3. 35a) shows also the presence of α -Si₃N₄. These observations indicate that the SiHfBN5 ceramic undergoes phase

separation starting from Hf-containing regions at 1500 °C.

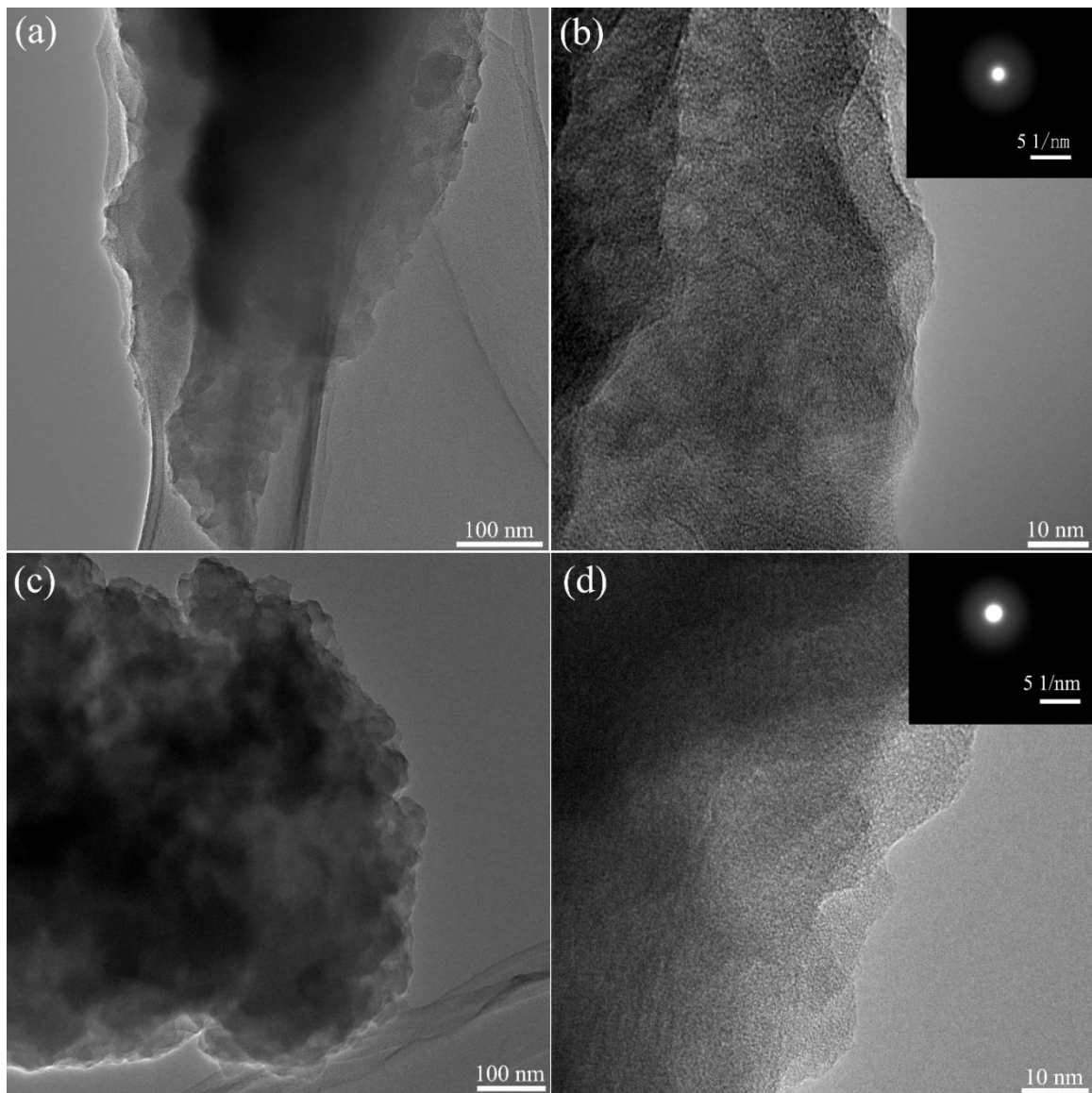


Figure 3.34 TEM images of the SiHfBN_1000 (a and b) and SiHfBN_1300 (c and d) bulk ceramics; (b) and (d) are high resolution images magnified from (a) and (c), respectively; the inset in (b) and (d) is the SAED images.

The TEM images of the SiHfBN5 sample annealed at 1700 °C show the presence of $\text{HfB}_x\text{N}_{1-x}$ crystals embedded within crystalline $\alpha/\beta\text{-Si}_3\text{N}_4$ nanoparticles, which are distinguished by their dark ($\text{HfB}_x\text{N}_{1-x}$) and light contrast ($\alpha/\beta\text{-Si}_3\text{N}_4$). Lattice fringes of the well-crystallized $\text{HfB}_x\text{N}_{1-x}$ and $\alpha/\beta\text{-Si}_3\text{N}_4$ nanograins are displayed in the high-resolution images (Figure 3.35d), in which the distances of 0.25 nm and 0.67 nm correspond to $\text{HfB}_x\text{N}_{1-x}$ and the (100) lattice plane of $\beta\text{-Si}_3\text{N}_4$, respectively, which is consistent with the XRD results. Furthermore, the lattice plane of $\alpha/\beta\text{-Si}_3\text{N}_4$ and $\text{HfB}_x\text{N}_{1-x}$ are also found in the SAED images (inset in Figure 3.35c).

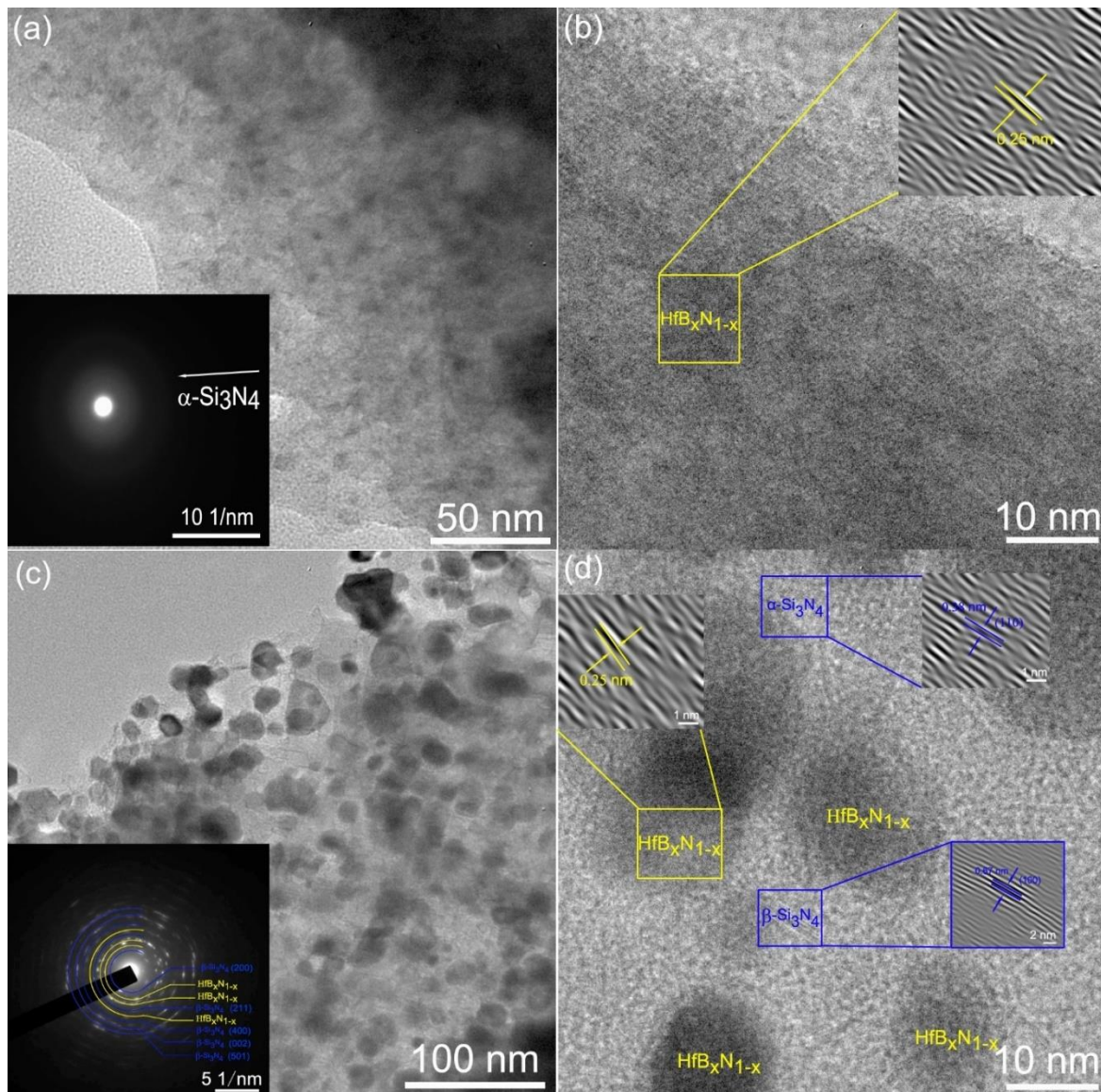


Figure 3.35 TEM images of bulk SiHfBN_1500 (a and b, b is a high-resolution image enlarged from a) and SiHfBN_1700 (c and d, d is a high-resolution image magnified from c); the insets in (a) and (c) are SAED images; the insets in (b) and (d) are FFT images from the selected areas.

3.3.2.4 Oxidation resistance

The oxidation behavior of bulk $\text{Si}_3\text{N}_4/\text{HfB}_x\text{N}_{1-x}$ specimens annealed at 1700 °C was investigated. The open porosity and skeletal density of the monolithic samples prepared by warm-pressing of the precursor powder and finally heat-treated at 1700 °C are 12.6, 12.9, 14.4 % and 2.67, 2.62, 2.55 $\text{g}\cdot\text{cm}^{-3}$ for SiHfBN2_1700, SiHfBN5_1700 and SiHfBN10_1700, respectively. The bulk $\text{Si}_3\text{N}_4/\text{HfB}_x\text{N}_{1-x}$ specimens were oxidized in static air at temperature up to 1500 °C for 50 h, and the mass change with the variation of oxidation times is shown in Figure 3.36. All samples undergo a rapid mass gain in the initial 10 h. The mass gain decreases with increasing molar ratio of boron in the feed, $\text{Si}_3\text{N}_4/\text{HfB}_x\text{N}_{1-x}$

ceramic nanocomposite with a molar ratio of B:Hf=10:1 shows the lowest weight change with only 2.57%, the SiHfBN5_1700 and SiHfBN2_1700 samples show higher weight gain up to 4.37% and 4.31%, respectively. The oxidation of SiHfBN ceramics does not conform with a parabolic oxidation behavior, which relates to the presence of open porosity in the investigated bulk samples.

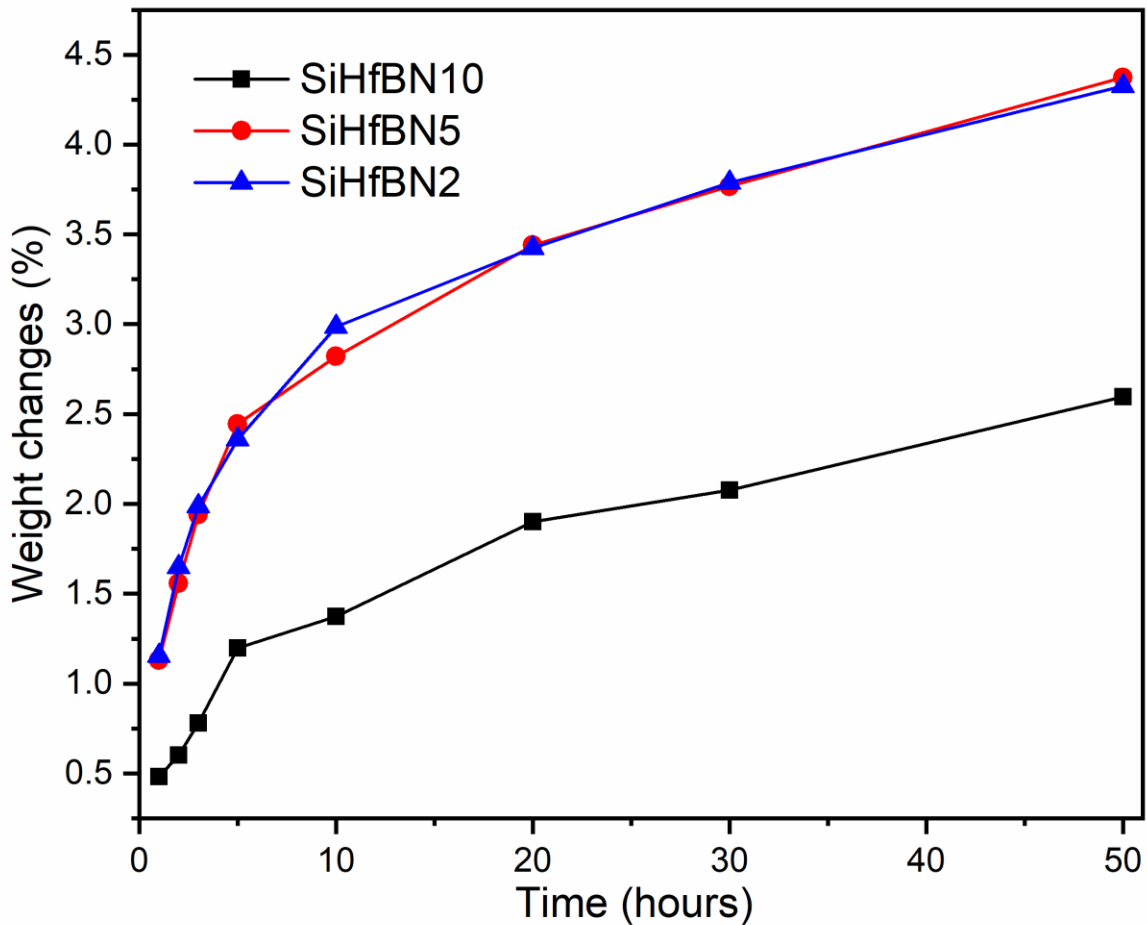


Figure 3. 36 Weight changes with the variation of oxidation times for bulk SiHfBN_1700 samples at 1500 °C.

In order to investigate the effects of hafnium and boron on the oxidation behavior of the $\text{Si}_3\text{N}_4/\text{HfB}_x\text{N}_{1-x}$ ceramic nanocomposites, the oxidized specimens were analyzed by means of XRD, and the XRD patterns are presented in Figure 3. 37. For all oxidized $\text{Si}_3\text{N}_4/\text{HfB}_x\text{N}_{1-x}$ samples, SiO_2 , HfSiO_4 and HfO_2 were analyzed, indicating that the oxidation of the $\text{HfB}_x\text{N}_{1-x}$ phase has an important contribution to the oxidation behavior of $\text{Si}_3\text{N}_4/\text{HfB}_x\text{N}_{1-x}$ ceramics [297]. The formation of HfSiO_4 is caused by the reaction between HfO_2 and SiO_2 , which is expected to enhance the oxidation resistance [298-300]. The oxidation of Si_3N_4 and $\text{HfB}_x\text{N}_{1-x}$ results in the formation of SiO_2 scale and liquid B_2O_3 at high oxidized temperature, respectively [301, 302]. The SiO_2 - B_2O_3 glass (i.e., borosilicate) was reported to form between a low-viscous B_2O_3 [303] and high-viscous SiO_2 glass [304], leading to a dense and continuous protective layer. The SiBO glass plays a role as a barrier against the inward diffusion of O_2 more effectively than that of liquid HfO_2 and B_2O_3 [305, 306]. Therefore, the oxidation resistance of the $\text{Si}_3\text{N}_4/\text{HfB}_x\text{N}_{1-x}$

ceramics takes advantage of the formation of HfSiO_4 , B_2O_3 and SiO_2 . However, no diffraction peaks of boron-containing crystalline phases were detected in the XRD patterns [20, 307]. This is because that boron is mainly located in $\text{HfB}_x\text{N}_{1-x}$ and homogeneously dispersed within the Si_3N_4 matrix. In addition, B_2O_3 is at the outer surface of the borosilicate layer, which is preferentially evaporated at temperature $> 1200\text{ }^\circ\text{C}$, resulting in the measured outer surface consisting predominantly of SiO_2 , HfSiO_4 and HfO_2 [301, 308].

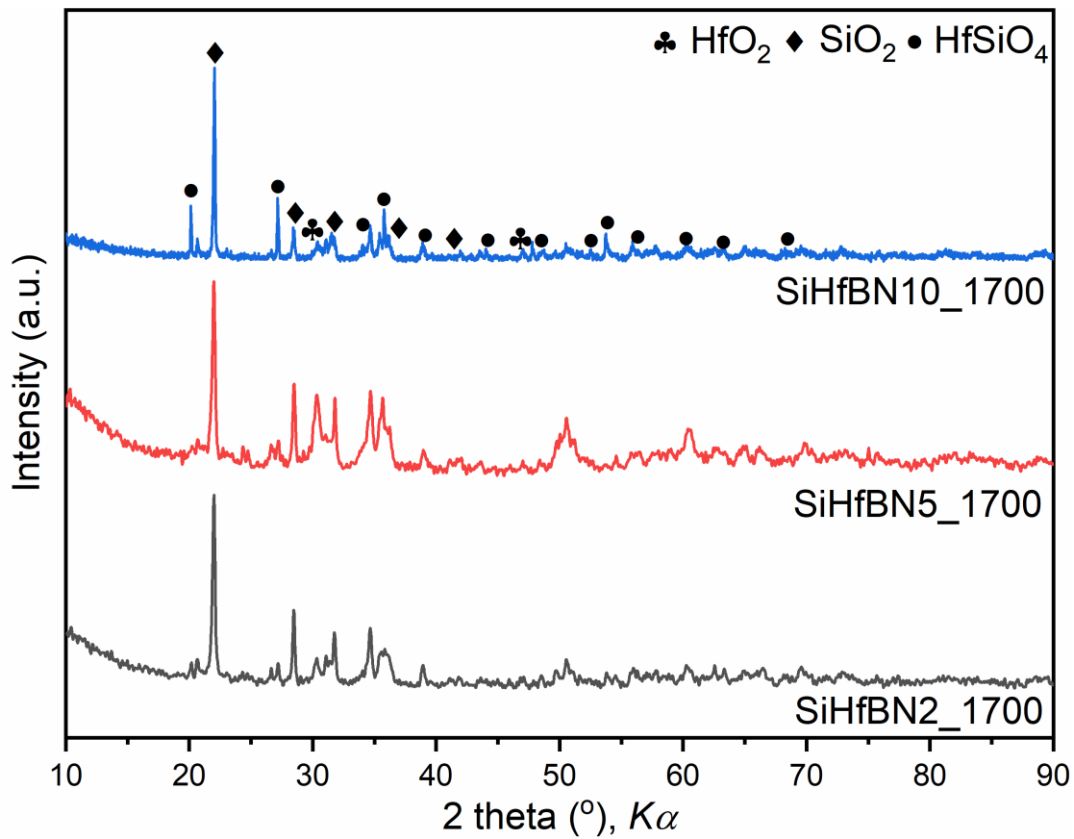


Figure 3. 37 XRD patterns of bulk SiHfBN₁₇₀₀ samples oxidized at 1500 °C in static air.

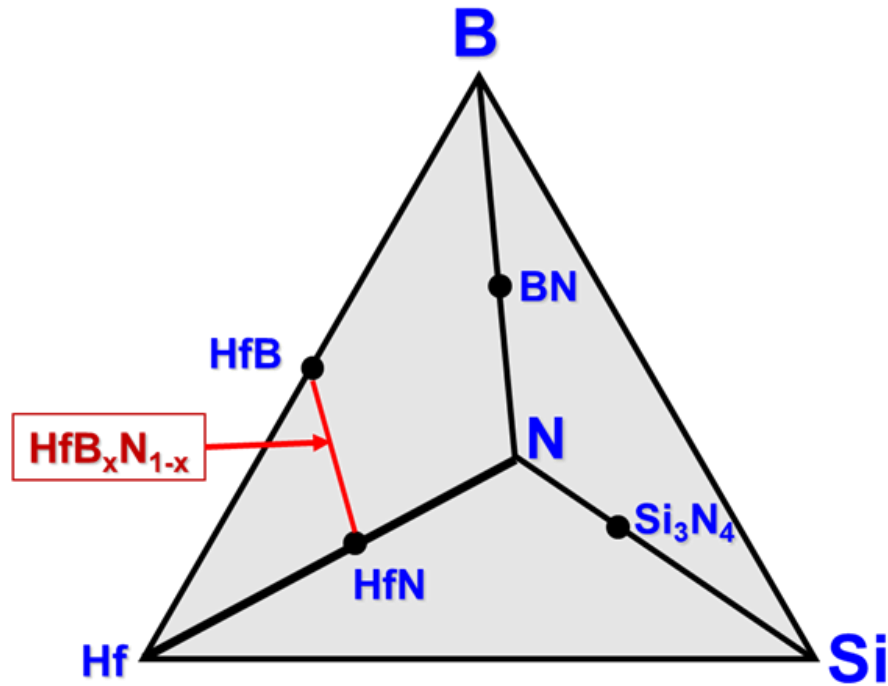


Figure 3. 38 Quaternary isothermal phase diagram SiHfBN with the two-phase subsystems, Si_3N_4 , HfN, HfB and BN. The analyzed crystalline ternary HfBN phase is part of the three-phase field Hf, N and B with compositions located on the tie line marked in red between NaCl-type HfB and HfN.

3.3.3 Conclusion

In the present study, SiBN and SiHfBN ceramics were prepared from novel single-source precursors, which were synthesized by the reaction of PHPS with TDMAH and BMS. The polymer-to-ceramic transformation of the single-source precursors shows that the incorporation of hafnium/boron significantly enhances the ceramic yield. The as-prepared BPSZX-derived ceramics are shown to possess remarkable resistance against crystallization in comparison to PHPS-derived boron-free Si_3N_4 ceramics. The resultant SiHfBN samples annealed in N_2 at temperatures in the range of 1300 – 1700 °C are found to undergo a phase conversion of the amorphous SiHfBN into nanostructured $\text{Si}_3\text{N}_4/\text{HfB}_x\text{N}_{1-x}$ composites. These results indicate that the conversion of the amorphous SiHfBN into $\text{Si}_3\text{N}_4/\text{HfB}_x\text{N}_{1-x}$ ceramic nanocomposites is thermodynamically controlled (Figure 3. 38), thus providing a route to prepare single-phase amorphous or multi-phase crystalline stable materials with tailored compositions. Moreover, bulk SiHfBN samples were successfully prepared by warm-pressing of the precursors at 110 °C and 120 MPa and subsequent pyrolysis of the obtained green bodies. The SiBN powders and bulk SiHfBN_1700 samples show improved oxidation behavior due to the formation of $\text{SiO}_2\text{-B}_2\text{O}_3$ glass.

4 Conclusions and outlook

4.1 Conclusions

Within the scope of this Ph.D. work, four types of Si_3N_4 -based ceramic nanocomposites (1. $\text{HfN}@a\text{-Si}_3\text{N}_4$, 2. $\text{HfN}/\text{Si}_3\text{N}_4$, 3. $\gamma\text{-Si}_3\text{N}_4/\text{Hf}_3\text{N}_4$, 4. $\text{Si}_3\text{N}_4/\text{HfB}_x\text{N}_{1-x}$) were synthesized by heat treatment of corresponding Hf-containing single-source precursors which were synthesized by chemical modification of PHPS with tetrakis(dimethylamido) hafnium(IV). Moreover, additive-free $\text{HfN}@a\text{-Si}_3\text{N}_4$, $\text{Si}_3\text{N}_4/\text{HfB}_x\text{N}_{1-x}$ and $\gamma\text{-Si}_3\text{N}_4/\text{Hf}_3\text{N}_4$ monoliths were fabricated by warmpressing and high pressure high temperature technique, respectively. The resultant SiHf(B)N ceramic nanocomposites were proven to exhibit promising mechanical properties and oxidation behavior due to the nanocomposite formation and unique microstructure. Several detailed findings are now summarized here.

- Additive-free bulk $\text{HfN}@a\text{-Si}_3\text{N}_4$ ceramic nanocomposite in which HfN nanocrystallites are homogeneously embedded in amorphous Si_3N_4 were prepared by in situ consolidation of preceramic polymer powders via warm-pressing followed by densification via ammonolysis and annealing. The critical issues concerning gas evolution and crystallization inducing bloating and cracking are addressed as follows: i) The warm-pressed samples with high density prevents the effluence of gaseous by-products from inside to the surface during further ammonolysis, resulting in the formation of pores and cracks; ii) A springback mechanism when releasing the pressure in uniaxial warm-pressing of the precursor causes cracks at higher pressures.
- The Vickers hardness and nano hardness of the resultant amorphous bulk SiHfN ceramics are 19.6 GPa and 17 GPa, respectively, which is comparable to most of polycrystalline Si_3N_4 - and amorphous Si_3N_4 -based ceramics. But the densification method in this work, warm pressing, is a resource-efficient low-temperature molding method compared with liquid phase sintering, hot-pressing (HP) or spark plasma sintering (SPS).
- In situ ED-XRD assessment of the phase evolution of the single-phase amorphous Si-Hf-N precursor under high pressure determined the optimal conditions (19.5 GPa and 1500 °C) for the formation and stability of $\gamma\text{-Si}_3\text{N}_4/\text{Hf}_3\text{N}_4$ ceramic nanocomposites. $\gamma\text{-Si}_3\text{N}_4/\text{Hf}_3\text{N}_4$ ceramic nanocomposite was prepared from an amorphous Si-Hf-N precursor at 20 GPa and 1500 °C.
- The fracture toughness of the resultant $\gamma\text{-Si}_3\text{N}_4/\text{Hf}_3\text{N}_4$ (6.98 $\text{MPa m}^{1/2}$) ceramic nanocomposite exhibits a significant improvement over pure $\gamma\text{-Si}_3\text{N}_4$ (3.5 $\text{MPa m}^{1/2}$) without sacrificing the hardness of the material, which is an excellent trade-off between hardness and fracture toughness compared to most other hard materials.
- The single-source precursors of B/Hf-PHPS were synthesized by modification of PHPS with TDMAH and BMS. The chemical reaction to form the single-source precursor was confirmed by

FT-IR and XPS, in which both Si-H and N-H groups of PHPS react with BMS and TDMAH. The investigation of the polymer-to-ceramic transformation indicates that the ceramic yield of B/Hf-modified PHPS is up to 100 wt% after pyrolysis at 1000 °C under ammonia.

- $\text{Si}_3\text{N}_4/\text{HfB}_x\text{N}_{1-x}$ ceramic nanocomposites were fabricated after annealing of the amorphous SiHfBN ceramic at 1700 °C under nitrogen. The found ternary $\text{HfB}_x\text{N}_{1-x}$ phase was determined to be a solid solution of rock salt-type HfN and HfB by XRD, Rietveld Refinement and TEM, which are homogeneously dispersed in the Si_3N_4 matrix.
- The oxidation behavior of the obtained $\text{Si}_3\text{N}_4/\text{HfB}_x\text{N}_{1-x}$ monoliths was investigated at 1500 °C. Incorporation of boron and hafnium into Si_3N_4 matrix substantially enhanced the oxidation resistance of the Si_3N_4 -based ceramics, which is ascribed to the decreased self-diffusion coefficient due to the formation of rigid B-N and Hf-N bonds in the Si-N network, which leads to the formation of HfSiO_4 , B_2O_3 and SiO_2 oxidation protective layer.

4.2 Outlook

During the course of this Ph.D. work, a systematic study of SiHf(B)N ceramics derived from suitable single-source precursors was carried out. Numerous useful information about single-source-precursor synthesis, polymer-to-ceramic transformation, microstructural evolution as well as mechanical properties and oxidation behavior was collected, which can provide some inspiration and guidance for future research. An outline for future works is recommended below.

- Additive-free bulk HfN@a- Si_3N_4 ceramic nanocomposite was prepared by a resource-efficient low-temperature molding method, warm-pressing. Although open porosity of the obtained ceramic is as low as 2.35%, its relative density amounts to 84%, indicating that additional closed pores are present. To avoid the formation of closed pores should be further investigated in order to improve the mechanical properties.
- Binary $\gamma\text{-Si}_3\text{N}_4/\text{Hf}_3\text{N}_4$ ceramic composites with excellent mechanical properties have been discovered using the polymer-derived ceramic route and high pressure-high temperature synthesis methods. In addition, several new groups of Bragg-reflections were observed to appear and disappear in different temperature regions by in-situ energy dispersive XRD, which could not be correlated with known phases and are candidates for possible ternary SiHfN compositions or solid solutions with the general composition $(\text{Si}_{1-x}/\text{Hf}_x)_3\text{N}_4$. Thus, the detailed analysis of these possible new phases should be pursued in the future.
- Amorphous SiBN ceramic powders exhibit an improved oxidation resistance compared with reported amorphous silicon nitride. However, preparing dense and additive-free SiBN monoliths is still a great challenge due to its low self-diffusion and has not been studied in detail yet, which deserves further study.

-
- The oxidation mechanism of $\text{Si}_3\text{N}_4/\text{HfB}_x\text{N}_{1-x}$ ceramic nanocomposites was analyzed and ascribed to precipitation of HfSiO_4 into borosilicate. However, a quantitative and qualitative analysis of the presence of B_2O_3 in the $\text{SiO}_2\text{-B}_2\text{O}_3$ glass (i.e., borosilicate) layers is still lacking due to the low sensitivity of most characterization techniques to light elements. This issue could be further investigated by advanced techniques (e.g., XPS and secondary ion mass spectrometry).
 - Single-source-precursor derived SiHf(B)N ceramics exhibited excellent mechanical properties and oxidation resistance. Thermal properties such as thermal shock resistance, thermal expansion and thermal conductivity should be investigated as the obtained SiHf(B)N ceramics are potential material candidates, which can be applied at high temperature beyond $1000\text{ }^\circ\text{C}$ up to $1500\text{ }^\circ\text{C}$.

5 Reference

- [1] Zerr A, Mische G, Serghiou G, Schwarz M, Kroke E, Riedel R, et al. Synthesis of cubic silicon nitride. *Nature*. 1999;400:340-342.
- [2] Zerr A, Kempf M, Schwarz M, Kroke E, Göken M, Riedel R. Elastic Moduli and Hardness of Cubic Silicon Nitride. *J Am Ceram Soc*. 2002;85:86-90.
- [3] Katz RN. High-temperature structural ceramics. *Science*. 1980;208:841-847.
- [4] Ziegler G, Heinrich J, Wötting G. Relationships between processing, microstructure and properties of dense and reaction-bonded silicon nitride. *J Mater Sci*. 1987;22:3041-3086.
- [5] Riley FL. Silicon Nitride and Related Materials. *J Am Ceram Soc*. 2000;83:245-265.
- [6] Krstic Z, Krstic VD. Silicon nitride: the engineering material of the future. *J Mater Sci*. 2011;47:535-552.
- [7] Klemm H. Silicon Nitride for High-Temperature Applications. *J Am Ceram Soc*. 2010;93:1501-1522.
- [8] Bocanegra-Bernal MH, Matovic B. Dense and near-net-shape fabrication of Si₃N₄ ceramics. *Mater Sci Eng A*. 2009;500:130-149.
- [9] Niihara K. New design concept of structural ceramics ceramic nanocomposites. *J Ceram Soc Jpn*. 1991;99:974-982.
- [10] Palmero P. Structural Ceramic Nanocomposites: A Review of Properties and Powders Synthesis Methods. *Nanomaterials*. 2015;5:656-696.
- [11] Mukhopadhyay A, Basu B. Consolidation-microstructure-property relationships in bulk nanoceramics and ceramic nanocomposites: a review. *Int Mater Rev*. 2007;52:257-288.
- [12] Sternitzke M. Structural ceramic nanocomposites. *J Eur Ceram Soc*. 1997;17:1061-1082.
- [13] Tian CY, Liu N. Effect of nano-TiN particles on microstructure and mechanical properties of Si₃N₄-based nanoceramics. *Adv Appl Ceram*. 2013;110:205-210.
- [14] Yuan J. SiHf(B)CN-based ultra-high temperature ceramic nanocomposites: Single-source precursor synthesis and behavior in hostile environments. Darmstadt: Technische Universität Darmstadt; 2015.
- [15] Wen Q. Single-Source-Precursor Synthesis and Properties of SiMC(N) Ceramic Nanocomposites (M = Hf, Ta, HfTa). Darmstadt: Technische Universität Darmstadt; 2017.
- [16] Zhou C. Ternary Si-Metal-N Ceramics: Single-Source-Precursor Synthesis, Nanostructure and Properties Characterization. Darmstadt: Technische Universität Darmstadt; 2017.
- [17] Wen Q, Xu Y, Xu B, Fasel C, Guillon O, Buntkowsky G, et al. Single-source-precursor synthesis of dense SiC/HfC_xN_{1-x}-based ultrahigh-temperature ceramic nanocomposites. *Nanoscale*. 2014;6:13678-13689.
- [18] Yu Z, Yang Y, Mao K, Feng Y, Wen Q, Riedel R. Single-source-precursor synthesis and phase evolution of SiC-TaC-C ceramic nanocomposites containing core-shell structured TaC@C nanoparticles. *J Adv Ceram*. 2020;9:320-328.
- [19] Zhou C, Gao X, Xu Y, Buntkowsky G, Ikuhara Y, Riedel R, et al. Synthesis and high-temperature

- evolution of single-phase amorphous Si-Hf-N ceramics. *J Eur Ceram Soc.* 2015;35:2007-2015.
- [20] Yuan J, Galetz M, Luan XG, Fasel C, Riedel R, Ionescu E. High-temperature oxidation behavior of polymer-derived SiHfBCN ceramic nanocomposites. *J Eur Ceram Soc.* 2016;36:3021-3028.
- [21] Bechelany MC, Proust V, Gervais C, Ghisleni R, Bernard S, Miele P. In situ controlled growth of titanium nitride in amorphous silicon nitride: a general route toward bulk nitride nanocomposites with very high hardness. *Adv Mater.* 2014;26:6548-6553.
- [22] Galusek D, Riley FL, Riedel R. Nanoindentation of a Polymer-Derived Amorphous Silicon Carbonitride Ceramic. *J Am Ceram Soc.* 2001;84:1164-1166.
- [23] Lee C-H, Lu H-H, Wang C-A, Nayak PK, Huang J-L. Microstructure and mechanical properties of TiN/Si₃N₄ nanocomposites by spark plasma sintering (SPS). *J Alloys Compd.* 2010;508:540-545.
- [24] Hou Z, Wang H, Yang Y-n, Song X, Chen S, Wan S, et al. High-pressure synthesis of high-performance submicron-sized polycrystalline β -Si₃N₄ bulk without additives. *Ceram Int.* 2020;46:12449-12457.
- [25] Nishiyama N, Ishikawa R, Ohfuji H, Marquardt H, Kurnosov A, Taniguchi T, et al. Transparent polycrystalline cubic silicon nitride. *Sci Rep.* 2017;7:44755-44763.
- [26] Wang P, Wang S, Zou Y, Zhu J, He D, Wang L, et al. Novel Nitride Materials Synthesized at High Pressure. *Crystals.* 2021;11:614-636.
- [27] Yunoshev A. Shock-Wave Synthesis of Cubic Silicon Nitride. *Combust Explos Shock Waves.* 2004;40:370-373.
- [28] Colombo P, Mera G, Riedel R, Sorarù GD. Polymer-Derived Ceramics: 40 Years of Research and Innovation in Advanced Ceramics. *J Am Ceram Soc.* 2010;93:1805-1837.
- [29] Fritz G, Raabe B. Bildung siliciumorganischer Verbindungen. V. Die Thermische Zersetzung von Si(CH₃)₄ und Si(C₂H₅)₄. *Z Anorg Allg Chem.* 1956;286:149-167.
- [30] Chantrell P, Popper P. Inorganic polymers and ceramics. *Special ceramics.* 1965;67:87-103.
- [31] Ainger F, Herbert J. The preparation of phosphorus-nitrogen compounds as non-porous solids. *Angewandte Chemie-international editoin: Wiley-Y-CH verlag GMBH Muhlenstrasse 33-34, D-13187 Berlin, Germany; 1959. p. 653-653.*
- [32] Verbeek W. Production of shaped articles of homogeneous mixtures of silicon carbide and nitride. *Google Patents; 1974.*
- [33] Verbeek W, Winter G. Formkoerper aus siliciumcarbid und verfahren zu ihrer herstellung. *DE Patent. 1974;2236078:A1.*
- [34] Winter G, Verbeek W, Mansmann M. Production of shaped articles of silicon carbide and silicon nitride. *Google Patents; 1975.*
- [35] Yajima S, Hayashi J, Omori M. Continuous silicon carbide fiber of high tensile strength. *Chem Lett.* 1975;4:931-934.
- [36] Yajima S, Okamura K, Hayashi J, Omori M. Synthesis of continuous SiC fibers with high tensile strength. *J Am Ceram Soc.* 1976;59:324-327.

- [37] Yajima S, Hayashi J, Omori M, Okamura K. Development of a silicon carbide fibre with high tensile strength. *Nature*. 1976;261:683-685.
- [38] Yajima S, Hasegawa Y, Okamura K, Matsuzawa T. Development of high tensile strength silicon carbide fibre using an organosilicon polymer precursor. *Nature*. 1978;273:525-527.
- [39] Yajima S, Omori M, Hayashi J, Okamura K, Matsuzawa T, Liaw C-f. Simple synthesis of the continuous SiC fiber with high tensile strength. *Chem Lett*. 1976;5:551-554.
- [40] Weinmann M, Haug R, Bill J, de Guire M, Aldinger F. Boron-modified polysilylcarbodi-imides as precursors for Si-B-C-N ceramics: Synthesis, plastic-forming and high-temperature behavior. *Appl Organomet Chem*. 1998;12:725-734.
- [41] Weinmann M, Schuhmacher J, Kummer H, Prinz S, Peng J, Seifert HJ, et al. Synthesis and Thermal Behavior of Novel Si-B-C-N Ceramic Precursors. *Chem Mater*. 2000;12:623-632.
- [42] Wang ZC, Aldinger F, Riedel R. Novel silicon-boron-carbon-nitrogen materials thermally stable up to 2200 °C. *J Am Ceram Soc*. 2001;84:2179-2183.
- [43] Yuan J, Li D, Johanns KE, Fasel C, Durst K, Kleebe H-J, et al. Preparation of dense SiHf(B)CN-based ceramic nanocomposites via rapid spark plasma sintering. *J Eur Ceram Soc*. 2017;37:5157-5165.
- [44] Wen Q, Yu Z, Xu Y, Lu Y, Fasel C, Morita K, et al. SiC/Hf_yTa_{1-y}C_xN_{1-x}/C ceramic nanocomposites with Hf_yTa_{1-y}C_xN_{1-x}-carbon core-shell nanostructure and the influence of the carbon-shell thickness on electrical properties. *J Mater Chem C*. 2018;6:855-864.
- [45] Ulrich AS, Kaiser T, Ionescu E, Riedel R, Galetz MC. Reactive element effect applied by alloying and SiHfBCN coating on the oxidation of pure chromium. *Oxid Met*. 2019;92:281-302.
- [46] Martínez-Crespiera S, Ionescu E, Kleebe H-J, Riedel R. Pressureless synthesis of fully dense and crack-free SiOC bulk ceramics via photo-crosslinking and pyrolysis of a polysiloxane. *J Eur Ceram Soc*. 2011;31:913-919.
- [47] Lange FF, Tu W, Evans A. Processing of damage-tolerant, oxidation-resistant ceramic matrix composites by a precursor infiltration and pyrolysis method. *Mater Sci Eng A*. 1995;195:145-150.
- [48] Plachký T, Lenčěš Z, Hric L, Šajgalík P, Baláž P, Riedel R, et al. Processing and mechanical properties of Si₃N₄ composites employing polymer-derived SiAlOC as sintering aid. *J Eur Ceram Soc*. 2010;30:759-767.
- [49] Ishihara S, Gu H, Bill J, Aldinger F, Wakai F. Densification of precursor-derived Si-C-N ceramics by high-pressure hot isostatic pressing. *J Am Ceram Soc*. 2002;85:1706-1712.
- [50] Mukherjee S, Ren Z, Singh G. Molecular polymer-derived ceramics for applications in electrochemical energy storage devices. *J Phys D: Appl Phys*. 2018;51:463001.
- [51] Wen Q, Qu F, Yu Z, Graczyk-Zajac M, Xiong X, Riedel R. Si-based polymer-derived ceramics for energy conversion and storage. *J Adv Ceram*. 2022;11:197-246.
- [52] Lale A, Schmidt M, Mallmann MD, Bezerra AVA, Acosta ED, Machado RAF, et al. Polymer-Derived Ceramics with engineered mesoporosity: From design to application in catalysis. *Surf Coat Technol*. 2018;350:569-586.

- [53] Bhandavat R, Pei Z, Singh G. Polymer-derived ceramics as anode material for rechargeable Li-ion batteries: a review. *Nanomater Energy*. 2012;1:324-337.
- [54] Sujith R, Jothi S, Zimmermann A, Aldinger F, Kumar R. Mechanical behaviour of polymer derived ceramics – a review. *Int Mater Rev*. 2020:1-24.
- [55] Hotza D, Nishihora RK, Machado RAF, Geffroy P-M, Chartier T, Bernard S. Tape casting of preceramic polymers toward advanced ceramics: A review. *Int J Ceram Eng Sci*. 2019;1:21-41.
- [56] Ishikawa T, Kohtoku Y, Kumagawa K. Production mechanism of polyzirconocarbo-silane using zirconium (IV) acetylacetonate and its conversion of the polymer into inorganic materials. *J Mater Sci*. 1998;33:161-166.
- [57] Ishikawa T, Kajii S, Matsunaga K, Hogami T, Kohtoku Y, Nagasawa T. A tough, thermally conductive silicon carbide composite with high strength up to 1600 °C in air. *Science*. 1998;282:1295-1297.
- [58] Ionescu E, Papendorf B, Kleebe HJ, Poli F, Müller K, Riedel R. Polymer-derived silicon oxycarbide/hafnia ceramic nanocomposites. Part I: phase and microstructure evolution during the ceramization process. *J Am Ceram Soc*. 2010;93:1774-1782.
- [59] Ionescu E, Linck C, Fasel C, Müller M, Kleebe HJ, Riedel R. Polymer-derived SiOC/ZrO₂ ceramic nanocomposites with excellent high-temperature stability. *J Am Ceram Soc*. 2010;93:241-250.
- [60] IWAMOTO Y, KIKUTA K-i, HIRANO S-i. Synthesis of poly-titanosilazanes and conversion into Si₃N₄-TiN ceramics. *J Ceram Soc Jpn*. 2000;108:350-356.
- [61] Papendorf B, Nonnenmacher K, Ionescu E, Kleebe HJ, Riedel R. Strong influence of polymer architecture on the microstructural evolution of hafnium-alkoxide-modified silazanes upon ceramization. *Small*. 2011;7:970-978.
- [62] Seyferth D, Lang H, Sobon CA, Borm J, Tracy HJ, Bryson N. Chemical modification of preceramic polymers: Their reactions with transition metal complexes and transition metal powders. *J Inorg Organomet Polym*. 1992;2:59-77.
- [63] Hauser R, Francis A, Theismann R, Riedel R. Processing and magnetic properties of metal-containing SiCN ceramic micro- and nano-composites. *J Mater Sci*. 2008;43:4042-4049.
- [64] Greenberg S, Clendenning SB, Liu K, Manners I, Aouba S, Ruda HE. Synthesis and lithographic patterning of polycarbosilanes with pendant cobalt carbonyl clusters. *Macromolecules*. 2005;38:2023-2026.
- [65] Iwamoto Y, Kikuta K, Hirano S. Synthesis of poly-titanosilazanes and conversion into Si₃N₄-TiN ceramics. *J Ceram Soc Jpn*. 2000;108:350-356.
- [66] Li Y, Zheng Z, Reng C, Zhang Z, Gao W, Yang S, et al. Preparation of Si–C–N–Fe magnetic ceramics from iron-containing polysilazane. *Appl Organomet Chem*. 2003;17:120-126.
- [67] Zhang X, Chen L, Meng L, Chen F, Kong J. Nickel silicide nanocrystal-containing magnetoceramics from the bulk pyrolysis of polysilazane and nickelocene. *Ceram Int*. 2014;40:6937-6947.

- [68] Tsirlin A, Shcherbakova G, Florina E, Popova N, Gubin S, Moroz E, et al. Nano-structured metal-containing polymer precursors for high temperature non-oxide ceramics and ceramic fibers-syntheses, pyrolyses and properties. *J Eur Ceram Soc.* 2002;22:2577-2585.
- [69] Amoros P, Beltran D, Guillem C, Latorre J. Synthesis and characterization of SiC/MC/C ceramics (M= Ti, Zr, Hf) starting from totally non-oxidic precursors. *Chem Mater.* 2002;14:1585-1590.
- [70] Toyoda R, Kitaoka S, Sugahara Y. Modification of perhydropolysilazane with aluminum hydride: Preparation of poly (aluminasilazane) s and their conversion into Si–Al–N–C ceramics. *J Eur Ceram Soc.* 2008;28:271-277.
- [71] Fonblanc D, Lopez-Ferber D, Wynn M, Lale A, Soleilhavoup A, Leriche A, et al. Crosslinking chemistry of poly (vinylmethyl-co-methyl) silazanes toward low-temperature formable preceramic polymers as precursors of functional aluminium-modified Si–C–N ceramics. *Dalton Trans.* 2018;47:14580-14593.
- [72] Bechelany MC, Proust V, Lale A, Miele P, Malo S, Gervais C, et al. Nanocomposites through the Chemistry of Single-Source Precursors: Understanding the Role of Chemistry behind the Design of Monolith-Type Nanostructured Titanium Nitride/Silicon Nitride. *Chemistry.* 2017;23:832-845.
- [73] Wen Q, Yu Z, Riedel R. The fate and role of in situ formed carbon in polymer-derived ceramics. *Prog Mater Sci.* 2020;109:100623-100686.
- [74] Wang Y, Su D, Ji H, Li X, Zhao Z, Tang H. Gradient structure high emissivity MoSi₂-SiO₂.SiOC coating for thermal protective application. *J Alloys Compd.* 2017;703:437-447.
- [75] Nakaya M, Kodama K, Yasuhara S, Hotta A. Novel gas barrier SiOC coating to PET bottles through a hot wire CVD method. *J Polym.* 2016;2016.
- [76] Nghiem Q-D, Kim D-P. Highly-resistant SiCBN films prepared by a simple spin-coating process with poly (borosilazane). *J Mater Chem.* 2005;15:2188-2192.
- [77] Wu C, Pan X, Lin F, Cui Z, Li X, Chen G, et al. High-temperature electrical properties of polymer-derived ceramic SiBCN thin films fabricated by direct writing. *Ceram Int.* 2022;48:15293-15302.
- [78] Eom J-H, Kim Y-W, Park CB, Wang C. Effect of forming methods on porosity and compressive strength of polysiloxane-derived porous silicon carbide ceramics. *J Ceram Soc Jpn.* 2012;120:199-203.
- [79] Hundley JM, Eckel ZC, Schueller E, Cante K, Biesboer SM, Yahata BD, et al. Geometric characterization of additively manufactured polymer derived ceramics. *Addit Manuf.* 2017;18:95-102.
- [80] Wang M, Xie C, He R, Ding G, Zhang K, Wang G, et al. Polymer-derived silicon nitride ceramics by digital light processing based additive manufacturing. *J Am Ceram Soc.* 2019;102:5117-5126.
- [81] Jana P, Santoliquido O, Ortona A, Colombo P, Sorarù GD. Polymer-derived SiCN cellular structures from replica of 3D printed lattices. *J Am Ceram Soc.* 2018;101:2732-2738.
- [82] Bernard S, Weinmann M, Gerstel P, Miele P, Aldinger F. Boron-modified polysilazane as a novel single-source precursor for SiBCN ceramic fibers: synthesis, melt-spinning, curing and ceramic conversion. *J Mater Chem.* 2005;15:289-299.
- [83] Liu Y, Chen K, Dong F, Peng S, Cui Y, Zhang C, et al. Effects of hydrolysis of precursor on the

-
- structures and properties of polymer-derived SiBN ceramic fibers. *Ceram Int.* 2018;44:10199-10203.
- [84] Silva BA, Ribeiro LFB, González SYG, Hotza D, Moreira RdFPM, Junior ADN. SiOC and SiCN-based ceramic supports for catalysts and photocatalysts. *Microporous Mesoporous Mater.* 2021;327:111435.
- [85] Li X, Zhang L, Yin X, Yu Z. Mechanical and dielectric properties of porous Si₃N₄-SiC (BN) ceramic. *J Alloys Compd.* 2010;490:L40-L43.
- [86] Li J, Bernard S, Salles V, Gervais C, Miele P. Preparation of polyborazylene-derived bulk boron nitride with tunable properties by warm-pressing and pressureless pyrolysis. *Chem Mater.* 2010;22:2010-2019.
- [87] Konetschny C, Galusek D, Reschke S, Fasel C, Riedel R. Dense silicon carbonitride ceramics by pyrolysis of cross-linked and warm pressed polysilazane powders. *J Eur Ceram Soc.* 1999;19:2789-2796.
- [88] Zhang T, Evans J, Woodthorpe J. Injection moulding of silicon carbide using an organic vehicle based on a preceramic polymer. *J Eur Ceram Soc.* 1995;15:729-734.
- [89] Walter S, Suttor D, Erny T, Hahn B, Greil P. Injection moulding of polysiloxane/filler mixtures for oxycarbide ceramic composites. *J Eur Ceram Soc.* 1996;16:387-393.
- [90] Liu D, Shi B, Wang C, Li Z, Wang X, Xu B, et al. Polymer-derived SiC ceramic aerogels with in-situ growth of SiC nanowires. *Ceram Int.* 2022;48:9157-9163.
- [91] Liu J, Qiao Y, Zhang P, Xue Y, Cai Z. Synthesis of SiC ceramics from polysilazane by laser pyrolysis. *Surf Coat Technol.* 2017;321:491-495.
- [92] Ma C, He C, Wang W, Yao X, Yan L, Hou F, et al. Metal-doped polymer-derived SiOC composites with inorganic metal salt as the metal source by digital light processing 3D printing. *Virtual Phys Prototyp.* 2020;15:294-306.
- [93] Bakumov V, Schwarz M, Kroke E. Emulsion processing of polymer-derived porous Si/C/(O) ceramic bodies. *J Eur Ceram Soc.* 2009;29:2857-2865.
- [94] Vakifahmetoglu C, Balliana M, Colombo P. Ceramic foams and micro-beads from emulsions of a preceramic polymer. *J Eur Ceram Soc.* 2011;31:1481-1490.
- [95] Hotza D, Nishihora RK, Machado RA, Geffroy Pm, Chartier T, Bernard S. Tape casting of preceramic polymers toward advanced ceramics: A review. *Int J Ceram Eng Sci.* 2019;1:21-41.
- [96] Kuo T, Rueschhoff LM, Dickerson MB, Patel TA, Faber KT. Hierarchical porous SiOC via freeze casting and self-assembly of block copolymers. *Scr Mater.* 2021;191:204-209.
- [97] Dong B-B, Wang F-H, Yang M-Y, Yu J-L, Hao L-Y, Xu X, et al. Polymer-derived porous SiOC ceramic membranes for efficient oil-water separation and membrane distillation. *J Membr Sci.* 2019;579:111-119.
- [98] Shah SR, Raj R. Mechanical properties of a fully dense polymer derived ceramic made by a novel pressure casting process. *Acta Mater.* 2002;50:4093-4103.
- [99] Seitz J, Bill J. Production of compact polysilazane-derived Si/C/N-ceramics by plastic forming. *J Mater Sci Lett.* 1996;15:391-393.

-
- [100] Ma M, Wang H, Xiong L, Huang S, Li X, Du X. Self-assembled homogeneous SiOC@C/graphene with three-dimensional lamellar structure enabling improved capacity and rate performances for lithium ion storage. *Carbon*. 2022;186:273-281.
- [101] Saha A, Raj R, Williamson DL. A model for the nanodomains in polymer-derived SiCO. *J Am Ceram Soc*. 2006;89:2188-2195.
- [102] Sorarù GD, Modena S, Guadagnino E, Colombo P, Egan J, Pantano C. Chemical durability of silicon oxycarbide glasses. *J Am Ceram Soc*. 2002;85:1529-1536.
- [103] Peña-Alonso R, Mariotto G, Gervais C, Babonneau F, Soraru GD. New Insights on the High-Temperature Nanostructure Evolution of SiOC and B-Doped SiBOC Polymer-Derived Glasses. *Chem Mater*. 2007;19:5694-5702.
- [104] Riedel R, Kienzle A, Dressler W, Ruwisch L, Bill J, Aldinger F. A silicoboron carbonitride ceramic stable to 2,000 °C. *Nature*. 1996;382:796-798.
- [105] Shao P, Ma C, Han D, Liu K, Li M, Liang Y, et al. Temperature-sensing performance of polymer-derived SiAlCN ceramics up to 1000 °C. *Ceram Int*. 2022;48:25277-25283.
- [106] Wen Q, Feng Y, Yu Z, Peng D-L, Nicoloso N, Ionescu E, et al. Microwave Absorption of SiC/HfC_xN_{1-x}/C Ceramic Nanocomposites with HfC_xN_(1-x)-Carbon Core-Shell Particles. *J Am Ceram Soc*. 2016;99:2655-2663.
- [107] Ionescu E, Linck C, Fasel C, Muller M, Kleebe HJ, Riedel R. Polymer-Derived SiOC/ZrO₂ Ceramic Nanocomposites with Excellent High-Temperature Stability. *J Am Ceram Soc*. 2010;93:241-250.
- [108] Kleebe H-J, Blum YD. SiOC ceramic with high excess free carbon. *J Eur Ceram Soc*. 2008;28:1037-1042.
- [109] Mera G, Ionescu E. Polymer-Derived Ceramics. *Encyclopedia of Inorganic and Bioinorganic Chemistry* 2019. p. 1-26.
- [110] Varshneya AK. *Fundamentals of inorganic glasses*: Elsevier; 2013.
- [111] Colombo P, Riedel R, Sorarù GD, Kleebe H-J. *Polymer derived Ceramics: from Nano-structure to Applications*. Lancaster, Pennsylvania: DEStech Publications; 2010.
- [112] Riedel R, Mera G, Hauser R, Klonczynski A. Silicon-based polymer-derived ceramics: synthesis properties and applications-a review dedicated to Prof. Dr. Fritz Aldinger on the occasion of his 65th birthday. *J Ceram Soc Jpn*. 2006;114:425-444.
- [113] Bernardo E, Fiocco L, Parcianello G, Storti E, Colombo P. Advanced Ceramics from Pre-ceramic Polymers Modified at the Nano-Scale: A Review. *Materials*. 2014;7:1927-1956.
- [114] Greil P. Polymer derived engineering ceramics. *Adv Eng Mater*. 2000;2:339-348.
- [115] Li W, Li F, Yu Z, Wen Q, Fan B, Feng Y, et al. Polymer-derived SiHfN ceramics: From amorphous bulk ceramics with excellent mechanical properties to high temperature resistant ceramic nanocomposites. *J Eur Ceram Soc*. 2022;42:4493-4502.
- [116] Zhuang K, Lin S, Huang W, Liao L, Zheng Y, Li L, et al. Realizing high ceramic yield and low

shrinkage of in-situ formed lightweight 3D-SiC (rGO) px polymer-derived ceramics with excellent fracture toughness. *Ceram Int.* 2020;46:27426-27436.

[117] Blum YD, Schwartz KB, Laine RM. Preceramic polymer pyrolysis. *J Mater Sci.* 1989;24:1707-1718.

[118] Segal D. Chemical synthesis of ceramic materials. *J Mater Chem.* 1997;7:1297-1305.

[119] Giannetti E. Thermal stability and bond dissociation energy of fluorinated polymers: A critical evaluation. *J Fluorine Chem.* 2005;126:623-630.

[120] Wolff F, Kugler C, Münstedt H. Viscoelastic properties of a silicone resin during crosslinking. *Rheol Acta.* 2011;50:917-924.

[121] Takahashi T, Colombo P. SiOC ceramic foams through melt foaming of a methylsilicone preceramic polymer. *J Porous Mater.* 2003;10:113-121.

[122] Narisawa M. Silicone resin applications for ceramic precursors and composites. *Materials.* 2010;3:3518-3536.

[123] Greil P. Active-filler-controlled pyrolysis of preceramic polymers. *J Am Ceram Soc.* 1995;78:835-848.

[124] Greil P. Near net shape manufacturing of polymer derived ceramics. *J Eur Ceram Soc.* 1998;18:1905-1914.

[125] Schwab ST, Graef RC, Blanchard CR, Dec SF, Maciel GG. The pyrolytic conversion of perhydropolysilazane into silicon nitride. *Ceram Int.* 1998;24:411-414.

[126] Riedel R, Bill J, Kienzle A. Boron-modified Inorganic Polymers-Precursors for the Synthesis of Multicomponent Ceramics. *Appl Organomet Chem.* 1996;10:241-256.

[127] Ionescu E, Kleebe HJ, Riedel R. Silicon-containing polymer-derived ceramic nanocomposites (PDC-NCs): preparative approaches and properties. *Chem Soc Rev.* 2012;41:5032-5052.

[128] Derby B. Ceramic nanocomposites: mechanical properties. *Curr Opin Solid State Mater Sci.* 1998;3:490-495.

[129] Giannelis EP. A new strategy for synthesizing polymer-ceramic nanocomposites. *JOM.* 1992;44:28-30.

[130] Sawaguchi A, Toda K, Niihara K. Mechanical and electrical properties of silicon nitride–silicon carbide nanocomposite material. *J Am Ceram Soc.* 1991;74:1142-1144.

[131] Feng Y, Yu Z, Riedel R. Enhanced hydrogen evolution reaction catalyzed by carbon-rich $\text{Mo}_{0.8}\text{Si}_3\text{C}_{0.6}/\text{C}/\text{SiC}$ nanocomposites via a PDC approach. *J Am Ceram Soc.* 2019;103:1385-1395.

[132] Boiko O, Koltunowicz TN, Zukowski P, Fedotov AK, Larkin AV. The effect of sputtering atmosphere parameters on dielectric properties of the ferromagnetic alloy–ferroelectric ceramics nanocomposite $(\text{FeCoZr})_x(\text{PbZrTiO}_3)_{(100-x)}$. *Ceram Int.* 2017;43:2511-2516.

[133] Zhang T, Kumari L, Du G, Li W, Wang Q, Balani K, et al. Mechanical properties of carbon nanotube–alumina nanocomposites synthesized by chemical vapor deposition and spark plasma sintering. *Compos A: Appl Sci Manuf.* 2009;40:86-93.

- [134] Chu BT, Tobias G, Salzmann CG, Ballesteros B, Grobert N, Todd RI, et al. Fabrication of carbon-nanotube-reinforced glass-ceramic nanocomposites by ultrasonic in situ sol-gel processing. *J Mater Chem*. 2008;18:5344-5349.
- [135] Giannelis E, Mehrotra V, Tse O, Vaia R, Sung T-C. Intercalated Two-Dimensional Ceramic Nanocomposites. *MRS Online Proceedings Library (OPL)*. 1991;249:547-558.
- [136] Herlin N, Luce M, Musset E, Cauchetier M. Synthesis and characterization of nanocomposite Si/C/N powders by laser spray pyrolysis of hexamethyldisilazane. *J Eur Ceram Soc*. 1994;13:285-291.
- [137] Biamino S, Fino P, Pavese M, Badini C. Alumina–zirconia–yttria nanocomposites prepared by solution combustion synthesis. *Ceram Int*. 2006;32:509-513.
- [138] Jia D, Liang B, Yang Z, Zhou Y. Metastable Si-BCN ceramics and their matrix composites developed by inorganic route based on mechanical alloying: Fabrication, microstructures, properties and their relevant basic scientific issues. *Prog Mater Sci*. 2018;98:1-67.
- [139] Viard A, Fonblanc D, Lopez-Ferber D, Schmidt M, Lale A, Durif C, et al. Polymer Derived Si-B-C-N Ceramics: 30 Years of Research. *Adv Eng Mater*. 2018;20:1800360.
- [140] Wen Q, Yu Z, Liu X, Bruns S, Yin X, Eriksson M, et al. Mechanical properties and electromagnetic shielding performance of single-source-precursor synthesized dense monolithic SiC/HfC_xN_{1-x}/C ceramic nanocomposites. *J Mater Chem C*. 2019;7:10683-10693.
- [141] Wang Y, Liu W, Guo J, Li M, Fan B, Wang H, et al. In situ formation of Si₃N₄-SiC nanocomposites through polymer-derived SiAlCN ceramics and spark plasma sintering. *Ceram Int*. 2021;47:22049-22054.
- [142] Kaspar J, Terzioglu C, Ionescu E, Graczyk-Zajac M, Hapis S, Kleebe HJ, et al. Stable SiOC/Sn nanocomposite anodes for lithium-ion batteries with outstanding cycling stability. *Adv Funct Mater*. 2014;24:4097-4104.
- [143] Feng Y, Yu Z, Schuch J, Tao S, Wiehl L, Fasel C, et al. Nowotny phase Mo_{3+2x}Si₃C_{0.6} dispersed in a porous SiC/C matrix: A novel catalyst for hydrogen evolution reaction. *J Am Ceram Soc*. 2020;103:508-519.
- [144] Chen L, Zhao J, Wang L, Peng F, Liu H, Zhang J, et al. In-situ pyrolyzed polymethylsilsequioxane multi-walled carbon nanotubes derived ceramic nanocomposites for electromagnetic wave absorption. *Ceram Int*. 2019;45:11756-11764.
- [145] Awin EW, Sridar S, Kousaalya AB, Vendra SL, Koroleva E, Filimonov A, et al. Low frequency dielectric behavior and AC conductivity of polymer derived SiC(O)/HfC_xN_{1-x} ceramic nanocomposites. *Mater Chem Phys*. 2021;260:124122-124131.
- [146] Francis A. Progress in polymer-derived functional silicon-based ceramic composites for biomedical and engineering applications. *Mater Res Express*. 2018;5:062003-0620035.
- [147] Silva BA, Ribeiro LFB, González SYG, Hotza D, Moreira RdFPM, Junior ADN. SiOC and SiCN-based ceramic supports for catalysts and photocatalysts. *Microporous Mesoporous Mater*. 2021;327:111435-111452.

- [148] Okoroanyanwu U, Bhardwaj A, Einck V, Ribbe A, Hu W, Rodriguez JM, et al. Rapid preparation and electrochemical energy storage applications of silicon carbide and silicon oxycarbide ceramic/carbon nanocomposites derived via flash photothermal pyrolysis of organosilicon preceramic polymers. *Chem Mater*. 2021;33:678-694.
- [149] Barroso G, Li Q, Bordia RK, Motz G. Polymeric and ceramic silicon-based coatings—a review. *J Mater Chem A*. 2019;7:1936-1963.
- [150] Kaur S, Gallei M, Ionescu E. Polymer–Ceramic Nanohybrid Materials. In: Kalia S, Haldorai Y, editors. *Organic-Inorganic Hybrid Nanomaterials*. Cham: Springer International Publishing; 2015. p. 143-185.
- [151] Riedel R, Kleebe H-J, Schönfelder H, Aldinger F. A covalent micro/nano-composite resistant to high-temperature oxidation. *Nature*. 1995;374:526-528.
- [152] Riedel R, Ruswisch LM, An L, Raj R. Amorphous Silicoboron Carbonitride Ceramic with Very High Viscosity at Temperatures above 1500°C. *J Am Ceram Soc*. 1998;81:3341-3344.
- [153] Bernard S, Miele P. Polymer-Derived Boron Nitride: A Review on the Chemistry, Shaping and Ceramic Conversion of Borazine Derivatives. *Materials*. 2014;7:7436-7459.
- [154] Ionescu E, Bernard S, Lucas R, Kroll P, Ushakov S, Navrotsky A, et al. Polymer-Derived Ultra-High Temperature Ceramics (UHTCs) and Related Materials. *Adv Eng Mater*. 2019;21:1900269-1900293.
- [155] Vakifahmetoglu C, Semerci T, Gurlo A, Soraru GD. Polymer derived ceramic aerogels. *Curr Opin Solid State Mater Sci*. 2021;25:100936-100948.
- [156] Barrios E, Zhai L. A review of the evolution of the nanostructure of SiCN and SiOC polymer derived ceramics and the impact on mechanical properties. *Mol Syst Des Eng*. 2020;5:1606-1641.
- [157] Duan W, Yin X, Li Q, Schlier L, Greil P, Travitzky N. A review of absorption properties in silicon-based polymer derived ceramics. *J Eur Ceram Soc*. 2016;36:3681-3689.
- [158] Lu K. Porous and high surface area silicon oxycarbide-based materials-A review. *Mater Sci Eng R Rep*. 2015;97:23-49.
- [159] Ren Z, Mujib SB, Singh G. High-Temperature Properties and Applications of Si-Based Polymer-Derived Ceramics: A Review. *Materials*. 2021;14.
- [160] Schulz M. Polymer derived ceramics in MEMS/NEMS—a review on production processes and application. *Adv Appl Ceram*. 2013;108:454-460.
- [161] Wynne KJ, Rice RW. Ceramics via polymer pyrolysis. *Annu Rev Mater Sci*. 1984;14:297-334.
- [162] Rice R. Ceramics from polymer pyrolysis, opportunities and needs- a materials perspective. *Am Ceram Soc Bull*. 1983;62:889.
- [163] Kuwabara A, Matsunaga K, Tanaka I. Lattice dynamics and thermodynamical properties of silicon nitride polymorphs. *Phys Rev B*. 2008;78.
- [164] Thompson D, Pratt P. *The Structure of Silicon Nitride in Science of Ceramics*; Stewart, GH, Ed. Academic Press: New York, NY, USA; 1967.

- [165] Jiang J, Kragh F, Frost D, Lindelov H. Hardness and thermal stability of cubic silicon nitride. *J Phys: Condens Matter*. 2001;13: L515-L520.
- [166] Vogelgesang R, Grimsditch M, Wallace JS. The elastic constants of single crystal β -Si₃N₄. *Appl Phys Lett*. 2000;76:982-984.
- [167] Niihara K, Hirai T. Chemical vapour-deposited silicon nitride. *J Mater Sci*. 1977;12:1243-1252.
- [168] Ogata S, Hirotsuki N, Kocer C, Shibutani Y. A comparative ab initio study of the 'ideal' strength of single crystal α - and β -Si₃N₄. *Acta Mater*. 2004;52:233-238.
- [169] Bocanegra-Bernal MH, Matovic B. Mechanical properties of silicon nitride-based ceramics and its use in structural applications at high temperatures. *Mater Sci Eng A*. 2010;527:1314-1338.
- [170] Hector AL. Synthesis and processing of silicon nitride and related materials using preceramic polymer and non-oxide sol-gel approaches. *Coord Chem Rev*. 2016;323:120-137.
- [171] Batha HD, Whitney ED. Kinetics and Mechanism of the Thermal Decomposition of Si₃N₄. *J Am Ceram Soc*. 1973;56:365-369.
- [172] Cao X, Yin X, Fan X, Zhao K, Luo H, Cheng L, et al. High-temperature flexural properties of SiBC modified C/SiC composites. *Ceram Int*. 2014;40:6185-6190.
- [173] Wen GW, Huang XX. Increased high temperature strength and oxidation resistance of Al₄SiC₄ ceramics. *J Eur Ceram Soc*. 2006;26:1281-1286.
- [174] Zou J, Zhang G-J, Hu C-F, Nishimura T, Sakka Y, Tanaka H, et al. High-temperature bending strength, internal friction and stiffness of ZrB₂-20vol% SiC ceramics. *J Eur Ceram Soc*. 2012;32:2519-2527.
- [175] Kingery W. Densification during sintering in the presence of a liquid phase. I. Theory. *J Appl Phys*. 1959;30:301-306.
- [176] Kingery W, Narasimhan M. Densification during sintering in the presence of a liquid phase. II. Experimental. *J Appl Phys*. 1959;30:307-310.
- [177] German RM, Suri P, Park SJ. Liquid phase sintering. *J Mater Sci*. 2009;44:1-39.
- [178] Petzow G, Huppmann W. Liquid phase sintering. *Zeitschrift fuer Metallkunde*. 1976;67:579-590.
- [179] Riley F. *Progress in nitrogen ceramics: Springer Science & Business Media*; 2012.
- [180] Kleebe H-J. Structure and chemistry of interfaces in Si₃N₄ ceramics studied by transmission electron microscopy. *J Ceram Soc Jpn*. 1997;105:453-475.
- [181] Hampshire S, Pomeroy MJ. Grain boundary glasses in silicon nitride: a review of chemistry, properties and crystallisation. *J Eur Ceram Soc*. 2012;32:1925-1932.
- [182] Soignard E, Somayazulu M, Dong J, Sankey OF, McMillan PF. High pressure-high temperature synthesis and elasticity of the cubic nitride spinel γ -Si₃N₄. *J Phys: Condens Matter*. 2001;13:557-563.
- [183] Bridgman PW. *The physics of high pressure*. London: G. Bell; 1949.
- [184] McMillan PF. Pressing on: The legacy of Percy W. Bridgman. *Nat Mater*. 2005;4:715-718.
- [185] Nishiyama N, Langer J, Sakai T, Kojima Y, Holzheid A, Gaida NA, et al. Phase relations in silicon and germanium nitrides up to 98 GPa and 2400 °C. *J Am Ceram Soc*. 2018;102:2195-2202.

- [186] Sekine T, He H, Kobayashi T, Zhang M, Xu F. Shock-induced transformation of β - Si_3N_4 to a high-pressure cubic-spinel phase. *Appl Phys Lett*. 2000;76:3706-3708.
- [187] Schlothauer T, Schwarz M, Ovidiu M, Brendler E, Moeckel R, Kroke E, et al. "Shock Wave" Synthesis of Oxygen-Bearing Spinel-Type Silicon Nitride γ - $\text{Si}_3(\text{O}, \text{N})_4$ in the Pressure Range from 30 to 72 GPa with High Purity. In: Krivovichev SV, editor. *Minerals as advanced materials II*. Berlin, Heidelberg: Springer Berlin Heidelberg; 2012. p. 375-388.
- [188] Sekine T. Shock synthesis of cubic silicon nitride. *J Am Ceram Soc*. 2002;85:113-116.
- [189] Mangels JA, Tennenhouse GJ. Densification of reaction-bonded silicon nitride. *Am Ceram Soc Bull*. 1980;59:1216-1218.
- [190] Kim H, Kim CH. The influence of the various transport properties of the nitriding atmosphere on the formation of reaction-bonded Si_3N_4 . *J Mater Sci*. 1985;20:149-156.
- [191] Deeley G, Herbert J, Moore N. Dense silicon nitride. *Powder Metall*. 1961;4:145-151.
- [192] Wötting G, Ziegler G. Influence of powder properties and processing conditions on microstructure and mechanical properties of sintered Si_3N_4 . *Ceram Int*. 1984;10:18-22.
- [193] Almeida J, Fonseca A, Correia R, Baptista J. Pressureless sintering of silicon nitride with additives of the $\text{Y}_2\text{O}_3/\text{Al}_2\text{O}_3/\text{SiO}_2$ system. *Mater Sci Eng A*. 1989;109:395-400.
- [194] Guo W-M, Wu L-X, Ma T, You Y, Lin H-T. Rapid fabrication of Si_3N_4 ceramics by reaction-bonding and pressureless sintering. *J Eur Ceram Soc*. 2016;36:3919-3924.
- [195] Chawla KK. *Ceramic matrix composites*: Springer Science & Business Media; 2013.
- [196] Ritter J, Nair S, Gennari P, Dunlay W, Haggerty J, Garvey G. High-strength reaction-bonded silicon nitride. *Adv Ceram Mater*. 1988;3:415-417.
- [197] Sillapasal K, Danchaivijit S, Sujirote K. Effects of silicon powder size on the processing of reaction-bonded silicon nitride. *J Met Mater Miner*. 2005;15:97-102.
- [198] Strecker K, Gonzaga R, Ribeiro S, Hoffmann MJ. Substitution of Y_2O_3 by a rare earth oxide mixture as sintering additive of Si_3N_4 ceramics. *Mater Lett*. 2000;45:39-42.
- [199] Liang H, Zeng Y, Zuo K, Xia Y, Yao D, Yin J. Mechanical properties and thermal conductivity of Si_3N_4 ceramics with YF_3 and MgO as sintering additives. *Ceram Int*. 2016;42:15679-15686.
- [200] Tiegs TN, Kiggans JO, Lin H, Willkens CA. Comparison of properties of sintered and sintered reaction-bonded silicon nitride fabricated by microwave and conventional heating. *MRS Online Proceedings Library (OPL)*. 1994;347.
- [201] Kroll P, Eck B, Dronskowski R. First-Principles Studies of Extended Nitride Materials. *Adv Mater*. 2000;12:307-310.
- [202] Mo S-D, Ouyang L, Ching W, Tanaka I, Koyama Y, Riedel R. Interesting physical properties of the new spinel phase of Si_3N_4 and C_3N_4 . *Phys Rev Lett*. 1999;83:5046-5050.
- [203] Boyko T, Hunt A, Zerr A, Moewes A. Electronic structure of spinel-type nitride compounds Si_3N_4 , Ge_3N_4 , and Sn_3N_4 with tunable band gaps: application to light emitting diodes. *Phys Rev Lett*. 2013;111:097402-097407.

- [204] Peng H. Spark plasma sintering of Si₃N₄-based ceramics: sintering mechanism-tailoring microstructure-evaluation properties: Stockholm University; 2004.
- [205] Moshtaghoun BM, Gomez-Garcia D, Dominguez-Rodriguez A, Todd RI. Grain size dependence of hardness and fracture toughness in pure near fully-dense boron carbide ceramics. *J Eur Ceram Soc.* 2016;36:1829-1834.
- [206] Hall EO. Variation of Hardness of Metals with Grain Size. *Nature.* 1954;173:948-949.
- [207] Šajgalik P, Dusza J, Hoffmann M. Relationship between microstructure, toughening mechanisms, and fracture toughness of reinforced silicon nitride ceramics. *J Am Ceram Soc.* 1995;78:2619-2624.
- [208] Peterson IM, Tien TY. Effect of the grain boundary thermal expansion coefficient on the fracture toughness in silicon nitride. *J Am Ceram Soc.* 1995;78:2345-2352.
- [209] Riedel R, Chen I-W. *Ceramics science and technology, volume 2: materials and properties*: John Wiley & Sons; 2011.
- [210] Gogotsi YG. Particulate silicon nitride-based composites. *J Mater Sci.* 1994;29:2541-2556.
- [211] Buljan S, Sarin V. Silicon nitride-based composites. *Composites.* 1987;18:99-106.
- [212] Qi G-j, Zhang C-r, Hu H-f, Zhou C-c. PIP preparation of silica fibre fabric reinforced silicon nitride-based composites using polyhydridomethylsilazane. *Adv Compos Lett.* 2005;14:129-132.
- [213] Peni F, Crampon J, Duclos R, Cales B. Creep and microstructure of TiC particulate Si₃N₄-based composites. *J Eur Ceram Soc.* 1991;8:311-318.
- [214] Zhang R, Veprek S. Phase stabilities of self-organized nc-TiN/a-Si₃N₄ nanocomposites and of Ti_{1-x}Si_xN_y solid solutions studied by ab initio calculation and thermodynamic modeling. *Thin Solid Films.* 2008;516:2264-2275.
- [215] Lee B-T, Yoon Y-J, Lee K-H. Microstructural characterization of electroconductive Si₃N₄-TiN composites. *Mater Lett.* 2001;47:71-76.
- [216] Huang J-L, Chen S-Y, Lee M-T. Microstructure, chemical aspects, and mechanical properties of TiB₂/Si₃N₄ and TiN/Si₃N₄ composites. *J Mater Res.* 1994;9:2349-2354.
- [217] Zgalat-Lozynskyy O, Ieremenko L, Tkachenko I, Grinkevich K, Ivanchenko S, Zelinskiy A, et al. Tribological Properties of ZrN-Si₃N₄-TiN Composites Consolidated by Spark Plasma Sintering. *Powder Metall Met Ceram.* 2022;60:597-607.
- [218] Guo Z, Blugan G, Kirchner R, Reece M, Graule T, Kuebler J. Microstructure and electrical properties of Si₃N₄-TiN composites sintered by hot pressing and spark plasma sintering. *Ceram Int.* 2007;33:1223-1229.
- [219] Birot M, Pillot J-P, Dunogues J. Comprehensive chemistry of polycarbosilanes, polysilazanes, and polycarbosilazanes as precursors of ceramics. *Chem Rev.* 1995;95:1443-1477.
- [220] Krüger CR, Rochow EG. Polyorganosilazanes. *Journal of Polymer Science Part A: General Papers.* 1964;2:3179-3189.
- [221] Zhao Y, Shao C, Ji X, Zhang S. Synthesis and Characterization of Meltable and Soluble Reticulating Polysilazane Modified via Melamine Toward SiCN Ternary Ceramics. *J Inorg Organomet*

- [222] Zhang Q, Yang Z, Jia D, Chen Q, Zhou Y. Synthesis and structural evolution of dual-boron-source-modified polysilazane derived SiBCN ceramics. *New J Chem.* 2016;40:7034-7042.
- [223] Barysheva A, Mochalov G, Suvorov S. Synthesis of Polysilazane by Ammonolysis of Dichlorosilane in a Nucleophilic Solvent. *Russ J Appl Chem.* 2021;94:1226-1231.
- [224] Song Y, Zhao Y, Feng C, Lu Y. Synthesis and pyrolysis of polysilazane as the precursor of Si₃N₄/SiC ceramic. *J Mater Sci.* 1994;29:5745-5756.
- [225] Laine RM. Transition metal catalysed synthesis of oligo-and polysilazanes. *Platinum Met Rev.* 1988;32:64-71.
- [226] Laine RM, Blum YD, Tse D, Glaser R. Synthetic routes to oligosilazanes and polysilazanes (chapter 10). *Inorg Organomet Polym Mater.* 1988:125-144.
- [227] He J, Scarlete M, Harrod JF. Silicon nitride and silicon carbonitride by the pyrolysis of poly(methylsiladiazane). *J Am Ceram Soc.* 1995;78:3009-3017.
- [228] Wannagat U, Liehr W. Hydrazin-Silicium-Verbindungen. I. Mono-und Bis-(triorganosilyl)-hydrazine. *Z Anorg Allg Chem.* 1958;297:129-136.
- [229] Duguet E, Schappacher M, Soum A. High molar mass polysilazane: a new polymer. *Macromolecules.* 1992;25:4835-4839.
- [230] Bouquey M, Brochon C, Bruzaud S, Mingotaud A, Schappacher M, Soum A. Ring-opening polymerization of nitrogen-containing cyclic organosilicon monomers. *J Organomet Chem.* 1996;521:21-27.
- [231] Soum A, Billon L, Bouquey M, Bruzaud S, Duguet E, Schappacher M. Polysilazanes (Through Ring-Opening Polymerization). *Polymeric Materials Encyclopedia, Twelve Volume Set.* 2020:6747-7300.
- [232] Bechelany MC, Proust V, Lale A, Miele P, Malo S, Gervais C, et al. Nanocomposites through the chemistry of single-source precursors: understanding the role of chemistry behind the design of monolith-type nanostructured titanium nitride/silicon nitride. *Chem Eur J.* 2017;23:832-845.
- [233] Lale A, Proust V, Bechelany MC, Viard A, Malo S, Bernard S. A comprehensive study on the influence of the polyorganosilazane chemistry and material shape on the high temperature behavior of titanium nitride/silicon nitride nanocomposites. *J Eur Ceram Soc.* 2017;37:5167-5175.
- [234] Li W, Li F, Yu Z, Wen Q, Fan B, Feng Y, et al. Polymer-derived SiHfN ceramics: From amorphous bulk ceramics with excellent mechanical properties to high temperature resistant ceramic nanocomposites. *J Eur Ceram Soc.* 2022;42:4493-4502.
- [235] Zhou C, Fasel C, Ishikawa R, Gallei M, Ikuhara Y, Lauterbach S, et al. One-pot synthesis of a C/SiFeN (O)-based ceramic paper with in-situ generated hierarchical micro/nano-morphology. *J Eur Ceram Soc.* 2017;37:5193-5203.
- [236] Zhou C, Ott A, Ishikawa R, Ikuhara Y, Riedel R, Ionescu E. Single-source-precursor synthesis and high-temperature evolution of novel mesoporous SiVN(O)-based ceramic nanocomposites. *J Eur Ceram*

- [237] Toby BH, Von Dreele RB. GSAS-II: the genesis of a modern open-source all purpose crystallography software package. *J Appl Crystallogr.* 2013;46:544-549.
- [238] Oliver WC, Pharr GM. An improved technique for determining hardness and elastic modulus using load and displacement sensing indentation experiments. *J Mater Res.* 1992;7:1564-1583.
- [239] Li K, Li S, Li N, Dixon DA, Klein TM. Tetrakis(dimethylamido)hafnium Adsorption and Reaction on Hydrogen Terminated Si(100) Surfaces. *J Phys Chem C.* 2010;114:14061-14075.
- [240] Rodríguez-Reyes JCF, Teplyakov AV. Surface Transamination Reaction for Tetrakis(dimethylamido)titanium with NH_x -Terminated Si(100) Surfaces. *J Phys Chem C.* 2007;111:16498-16505.
- [241] Fang Z, Aspinall HC, Odedra R, Potter RJ. Atomic layer deposition of TaN and Ta_3N_5 using pentakis(dimethylamino)tantalum and either ammonia or monomethylhydrazine. *J Cryst Growth.* 2011;331:33-39.
- [242] Van Dijen FK, Pluijmakers J. The removal of carbon or carbon residues from ceramic powders or greenware with ammonia. *J Eur Ceram Soc.* 1989;5:385-390.
- [243] Katsnel'son L, Kerbel B. Determination of the optimal uniaxial pressing pressure for ceramic powders. *Glass Ceram.* 2014;70:319-323.
- [244] Vlasova MV, Lavrenko VA, Yu Dyubova L, Gonzalez-Rodriguez JG, Kakasey MG. Nitriding of Ferrosilicon Powders. *J Mater Synth Process.* 2001;9:111-117.
- [245] Terwilliger G, Lange F. Pressureless sintering of Si_3N_4 . *J Mater Sci.* 1975;10:1169-1174.
- [246] Xu W, Yin Z, Yuan J, Wang Z, Fang Y. Effects of sintering additives on mechanical properties and microstructure of Si_3N_4 ceramics by microwave sintering. *Mater Sci Eng A.* 2017;684:127-134.
- [247] Loehman RE, Rowcliffe DJ. Sintering of $\text{Si}_3\text{N}_4\text{-Y}_2\text{O}_3\text{-Al}_2\text{O}_3$. *J Am Ceram Soc.* 1980;63:144-148.
- [248] Lee D-D, Kang S-JL, Petzow G, Yoon DN. Effect of α to β (β') Phase Transition on the Sintering of Silicon Nitride Ceramics. *J Am Ceram Soc.* 1990;73:767-769.
- [249] Liu J, Yang J, Zhu S, Cheng J, Yu Y, Qiao Z, et al. Temperature-driven wear behavior of Si_3N_4 -based ceramic reinforced by in situ formed $\text{TiC}_{0.3}\text{N}_{0.7}$ particles. *J Am Ceram Soc.* 2019;102:4333-4343.
- [250] Cross TJ. Mechanical properties of polymer-derived ceramics constituted from silicon-carbon-oxygen-nitrogen and their tribological behavior in dry and humid environments [Ph.D Thesis]: University of Colorado; 2006.
- [251] Lee S-H. Densification, Mass Loss, and Mechanical Properties of Low-Temperature Pressureless-Sintered Si_3N_4 with LiYO_2 Additive: The Effects of Additive Content and Annealing. *Int J Appl Ceram Technol.* 2010;7:881-888.
- [252] Liu X-J, Huang Z-Y, Ge Q-M, Sun X-W, Huang L-P. Microstructure and mechanical properties of silicon nitride ceramics prepared by pressureless sintering with $\text{MgO-Al}_2\text{O}_3\text{-SiO}_2$ as sintering additive. *J Eur Ceram Soc.* 2005;25:3353-3359.
- [253] Das M, Bhimani K, Balla VK. In vitro tribological and biocompatibility evaluation of sintered

silicon nitride. *Mater Lett.* 2018;212:130-133.

[254] Kumar A, Gokhale A, Ghosh S, Aravindan S. Effect of nano-sized sintering additives on microstructure and mechanical properties of Si₃N₄ ceramics. *Mater Sci Eng A.* 2019;750:132-140.

[255] Li Y, Yu YX, San HS, Chen Y, Guo DQ, Wu XY. Full Dense SiCN Ceramics Derived from Polysilazane. *Adv Mat Res.* 2013;631-632:303-305.

[256] Rueschhoff LM, Trice RW, Youngblood JP. Near-net shaping of silicon nitride via aqueous room-temperature injection molding and pressureless sintering. *Ceram Int.* 2017;43:10791-10798.

[257] Wang L, Qi Q, Cai P, Zhang H, Yang X, Liu X, et al. New route to improve the fracture toughness and flexural strength of Si₃N₄ ceramics by adding FeSi₂. *Scr Mater.* 2017;126:11-14.

[258] Wang J, Chen ZQ, Li CM, Wang F, Zhong Y. First-Principles Study on Mechanical Properties of IVB-Group Transition-Metal Nitrides TiN, ZrN, and HfN. *Adv Mat Res.* 2011;415-417:1451-1456.

[259] Farla R, Bhat S, Sonntag S, Chanyshv A, Ma S, Ishii T, et al. Extreme conditions research using the large-volume press at the P61B endstation, PETRA III. *J Synchrotron Radiat.* 2022;29:409-423.

[260] Seto Y. <https://github.com/seto77/PDIndexer/>.

[261] Moradkhani A, Baharvandi H, Naserifar A. Fracture Toughness of 3Y-TZP Dental Ceramics by Using Vickers Indentation Fracture and SELNB Methods. *J Korean Ceram Soc.* 2019;56:37-48.

[262] Mattesini M, Ahuja R, Johansson B. Cubic Hf₃N₄ and Zr₃N₄: A class of hard materials. *Phys Rev B.* 2003;68:184108-184113.

[263] Tanakaa I, Oba F, Sekine T, Ito E, Kubo A, Tatsumi K, et al. Hardness of cubic silicon nitride. *J Mater Res.* 2002;17:731-733.

[264] Stishov SM, Popova SV. New dense polymorphic modification of silica. *Geokhimiya.* 1962;8:649-659.

[265] Léger JM, Haines J, Schmidt M, Petit JP, Pereira AS, da Jornada JAH. Discovery of hardest known oxide. *Nature.* 1996;383:401-401.

[266] Shemkunus MP, Petuskey WT, Chizmeshya AVG, Leinenweber K, Wolf GH. Hardness, elasticity, and fracture toughness of polycrystalline spinel germanium nitride and tin nitride. *J Mater Res.* 2004;19:1392-1399.

[267] Dzivenko D. High-pressure synthesis, structure and properties of cubic zirconium(IV)- and hafnium(IV) nitrides. Darmstadt: Technische Universität Darmstadt; 2009.

[268] Wang S, Antonio D, Yu X, Zhang J, Cornelius AL, He D, et al. The Hardest Superconducting Metal Nitride. *Sci Rep.* 2015;5:13733-13741.

[269] Chen X-J, Struzhkin VV, Wu Z, Somayazulu M, Qian J, Kung S, et al. Hard superconducting nitrides. *Proc Natl Acad Sci U S A.* 2005;102:3198-3201.

[270] Rice R. Ceramic fracture mode-intergranular vs transgranular fracture. American Ceramic Society, Westerville, (United States); 1996.

[271] Zhao J, Ai X, Lü Z. Preparation and characterization of Si₃N₄/TiC nanocomposite ceramics. *Mater Lett.* 2006;60:2810-2813.

- [272] Bouville F, Maire E, Meille S, Van de Moortèle B, Stevenson AJ, Deville S. Strong, tough and stiff bioinspired ceramics from brittle constituents. *Nat Mater.* 2014;13:508-514.
- [273] Solozhenko VL, Kurakevych OO, Le Godec Y. Creation of nanostructures by extreme conditions: high-pressure synthesis of ultrahard nanocrystalline cubic boron nitride. *Adv Mater.* 2012;24:1540-1544.
- [274] He D, Zhao Y, Daemen L, Qian J, Shen TD, Zerda TW. Boron suboxide: As hard as cubic boron nitride. *Appl Phys Lett.* 2002;81:643-645.
- [275] Auerkari P. Mechanical and physical properties of engineering alumina ceramics: Technical Research Centre of Finland Espoo; 1996.
- [276] Qian J, Daemen LL, Zhao Y. Hardness and fracture toughness of moissanite. *Diam Relat Mater.* 2005;14:1669-1672.
- [277] Filgueira M, Nascimento ÁLN, Oliveira MP, Souza D, Guimarães ZAS, dos Santos C. HPHT sintering of binderless Si_3N_4 : structure, microstructure, mechanical properties and machining behavior. *J Braz Soc Mech Sci Eng.* 2018;40:1-9.
- [278] Wang C-C, Song L-L. Nanosheet-structured B_4C with high hardness up to 42 GPa. *Chin Phys B.* 2019;28:066201-066205.
- [279] Qin J, Nishiyama N, Ohfuji H, Shinmei T, Lei L, He D, et al. Polycrystalline γ -boron: As hard as polycrystalline cubic boron nitride. *Scr Mater.* 2012;67:257-260.
- [280] Gui R, Xue Z, Zhou X, Gu C, Ren X, Cheng H, et al. Strain stiffening, high load-invariant hardness, and electronic anomalies of boron phosphide under pressure. *Phys Rev B.* 2020;101:035302-035316.
- [281] Drory MD, Ager JW, Suski T, Grzegory I, Porowski S. Hardness and fracture toughness of bulk single crystal gallium nitride. *Appl Phys Lett.* 1996;69:4044-4046.
- [282] Novikov NV, Dub S. Fracture toughness of diamond single crystals. *J Hard Mater.* 1992;2:3-11.
- [283] Morita K, Kim B-N, Hiraga K, Yoshida H. Fabrication of high-strength transparent MgAl_2O_4 spinel polycrystals by optimizing spark-plasma-sintering conditions. *J Mater Res.* 2009;24:2863-2872.
- [284] Ma D, Kou Z, Liu Y, Wang Y, Gao S, Luo X, et al. Sub-micron binderless tungsten carbide sintering behavior under high pressure and high temperature. *Int J Refract Met Hard Mater.* 2016;54:427-432.
- [285] Dzivenko DA, Zerr A, Mische G, Riedel R. Synthesis and properties of oxygen-bearing $c\text{-Zr}_3\text{N}_4$ and $c\text{-Hf}_3\text{N}_4$. *J Alloys Compd.* 2009;480:46-49.
- [286] Alexandre N, Desmaison-Brut M, Valin F, Boncoeur M. Mechanical properties of hot isostatically pressed zirconium nitride materials. *J Mater Sci.* 1993;28:2385-2390.
- [287] Moriyama M, Aoki H, Kobayashi Y, Kamata K. The mechanical properties of hot-pressed TiN ceramics with various additives. *J Ceram Soc Jpn.* 1993;101:279-284.
- [288] Desmaison-Brut M, Montintin J, Valin F, Boncoeur M. Mechanical properties and oxidation behaviour of HIPed hafnium nitride ceramics. *J Eur Ceram Soc.* 1994;13:379-386.
- [289] Hapke J, Ziegler G. Synthesis and pyrolysis of liquid organometallic precursors for advanced Si-Ti-C-N composites. *Adv Mater.* 1995;7:380-384.

- [290] Rastogi PK, Sahoo KR, Thakur P, Sharma R, Bawari S, Podila R, et al. Graphene–hBN non-van der Waals vertical heterostructures for four-electron oxygen reduction reaction. *Phys Chem Chem Phys*. 2019;21:3942-3953.
- [291] Yuan J, Hapis S, Breitzke H, Xu Y, Fasel C, Kleebe HJ, et al. Single-source-precursor synthesis of hafnium-containing ultrahigh-temperature ceramic nanocomposites (UHTC-NCs). *Inorg Chem*. 2014;53:10443-10455.
- [292] Chang L-C, Liu B-W, Chen Y-I. Mechanical Properties and Oxidation Behavior of Multilayered Hf–Si–N Coatings. *Coatings*. 2018;8:354.
- [293] Lengauer W, Binder S, Aigner K, Ettmayer P, Guillou A, Debuigne J, et al. Solid state properties of group IVb carbonitrides. *J Alloys Compd*. 1995;217:137-147.
- [294] Timofeeva II, Shvedova LK. Microhardness and thermal expansion of transition metal nitrides at 80-300 K. *Izv Akad Nauk SSSR, Neorg Mater*. 1972;8:1169-1170.
- [295] Glaser FW, Moskowitz D, Post B. A study of some binary hafnium compounds. *JOM*. 1953;5:1119-1120.
- [296] Shulishova O, Shcherbak I. Superconductivity of borides of transition and rare earth metals. *Inorg Mater*. 1967;3:1304-1306.
- [297] Jeong JJ, Hwang SK, Lee C. Hardness and adhesion properties of HfN/Si₃N₄ and NbN/Si₃N₄ multilayer coatings. *Mater Chem Phys*. 2003;77:27-33.
- [298] Carney CM, Parthasarathy TA, Cinibulk MK. Oxidation resistance of hafnium diboride ceramics with additions of silicon carbide and tungsten boride or tungsten carbide. *J Am Ceram Soc*. 2011;94:2600-2607.
- [299] Terauds K, Marshall DB, Raj R. Oxidation of Polymer-Derived HfSiCNO up to 1600 °C. *J Am Ceram Soc*. 2013;96:1278-1284.
- [300] Wang S, Zhang Y, Sun Y, Xu Y, Yang M. Synthesis and characteristic of SiBCN/HfN ceramics with high temperature oxidation resistance. *J Alloys Compd*. 2016;685:828-835.
- [301] Rezaie A, Fahrenholtz WG, Hilmas GE. Oxidation of zirconium diboride-silicon carbide at 1500 °C at a low partial pressure of oxygen. *J Am Ceram Soc*. 2006;89:3240-3245.
- [302] Karlsdottir SN, Halloran JW. Oxidation of ZrB₂-SiC: influence of SiC content on solid and liquid oxide phase formation. *J Am Ceram Soc*. 2009;92:481-486.
- [303] Napolitano A, Macedo PB, Hawkins EG. Viscosity and density of boron trioxide. *J Am Ceram Soc*. 1965;48:613-616.
- [304] Urbain G, Bottinga Y, Richet P. Viscosity of liquid silica, silicates and alumino-silicates. *Geochim Cosmochim Acta*. 1982;46:1061-1072.
- [305] Monteverde F, Bellosi A. The resistance to oxidation of an HfB₂-SiC composite. *J Eur Ceram Soc*. 2005;25:1025-1031.
- [306] Wang B, Li D, Yang Z, Jia D, Guan J, Cai D, et al. Study on oxidation resistance and oxidative damage mechanism of SiBCN-Ta₄HfC₅ composite ceramics. *Corros Sci*. 2022;197:110049-110061.

-
- [307] Lyu Y, Tang H, Zhao G. Effect of Hf and B incorporation on the SiOC precursor architecture and high-temperature oxidation behavior of SiHfBOC ceramics. *J Eur Ceram Soc.* 2020;40:324-332.
- [308] Karlsdottir SN, Halloran JW, Henderson CE. Convection patterns in liquid oxide films on ZrB₂-SiC composites oxidized at a high temperature. *J Am Ceram Soc.* 2007;90:2863-2867.

Acknowledgements

Wonderful time at TU Darmstadt flies. At this moment, I feel a lot of emotion in my heart. There are so many people I know and don't know who have helped me in my life at TU Darmstadt. I want to say some words to express my appreciation to the people who supported me during my Ph.D. period despite that it is impossible to completely my gratitude:

First of all, the deepest appreciation and respect to my supervisor, Prof. Dr. Ralf Riedel, who kindly gave me the valuable opportunity to study in his excellent group. He is a very humorous professor and always helps me with great eagerness not only on the research but also on my daily life. I really enjoy everyday working in his group and every time talking with him. Many thanks for his supervision, continuous support, professional suggestions and warm encouragements to my research during my Ph.D. study. His incredible enthusiasm and optimistic dedication to science have impressed me deeply. His rigorous attitude and wisdom in scientific research teach me how to continue my research career in future. In addition, I would like to thank him for his caring, patience and enthusiasm, and for his kind-hearted financial support in my life.

Secondly, many thanks to my co-supervisor, Prof. Dr. Zhaoju Yu, who is one of my most respected and grateful professor. I am especially grateful for her great ability, not only to share her academic knowledge but also to help organize my research, which has contributed to making my thesis and publications comprehensive. Prof. Dr. Yu is a well-read and rigorous professor and always keeps her friendly doors open. I have immeasurably treasured her advice and guidance, both in the scientific field and in daily life. In addition, I also would like to express my heartfelt gratitude for her optimistic advices and encouragements in my difficult time, which give me more power to continue my research. I am lucky to be one of the students she supervised.

Many thanks to Prof. Dr. Qingbo Wen, who provides great support with respect to my experiments from using apparatus to analyzing data. He is one of pioneers who introduced me into the PDC field. I also sincerely acknowledge his valuable comments and careful revision of my manuscript. I thoroughly enjoy the time that he took me to do experiments.

I sincerely thank PD Dr. Leonore Wiehl for her kind help and guidance in my Ph.D work, she has shared her plentiful experience with me on data characterization and analysis, especially high pressure high temperature synthesis and Rietveld Refinement. In addition, I also sincerely acknowledge her valuable comments and careful revision of my manuscript, which makes my manuscript more complete.

I sincerely acknowledge Prof. Dr. Anke Weidenkaff and Dr. Marc Widenmeyer for their help in TGA measurements and analysis as well as for revising my manuscript. Many thanks for Dr. Marc Widenmeyer bringing me to know and familiarize with Rietveld Refinement using the Fullprof software.

Dr. Ying Zhan, you are so sweet and considerate, like a sister to take care of me, also the sister in my heart. Thank you so much for sharing your life experience with me when I arrived in Germany, for your considerateness and help, and of course, for teaching me how to perform single-source-precursor synthesis and characterization, for taking time to correct my papers and my thesis and for our joint publications.

I also sincerely thank Dipl. Claudia Fasel for creating a stimulating and pleasant lab environment, for a lot of TG/MS measurements, and of course for her nice supports on all other daily experiments.

I would like to acknowledge Dr. Yao Feng for kindly supporting my work, for all valuable discussions and help, both in and out of the lab. Special thanks to you for teaching me how to face the challenges and solve problem in a scientific way.

I also would like to thank Dr. Meng Hu, Dr. Magdalena Joanna Graczyk-Zajac, Dr. Fangtong Xie, Dr. Isabel Gonzalo de Juan, Dr. Shrikant Bhat, Dipl. Dario De Carolis, Dr. Jiongjie Liu, Dr. Xingmin Liu, M. Sc. Yongchao Chen, M. Sc. Fangmu Qu, M. Sc. Nan Chai, M. Sc. Honghong Tian, M. Sc. Jan Bernauer, M. Sc. Emmanuel III Ricohermoso, M. Sc. Sefa Akca, M. Sc. Alexander Kempf, M. Sc. Alexander Ott, M. Sc. Marco Melzi d'Eril, M. Sc. Samuel Aeneas Kredel, M. Sc. Laura Feldmann, Mrs. Su-Chen Chang and all other Dispersive Solids group members who kindly supported my work or my life in different ways.

I really appreciate all my friends in Darmstadt and the time we spend together.

Many thanks to the Chinese Scholarship Council (CSC) for 4-year financial support on my Ph.D. study in Germany.

..... to everyone who has contributed to my Ph.D. career in any way, even if you are not mentioned, you are definitely not forgotten!

Particularly, I would like to deeply thank my dear parents, Mr. Xiqing Li and Mrs. Suling Zhang and all other family members who always love me, trust me and encourage me in my life.

Curriculum vitae

Wei Li

Nationality: China

Gender: Male

E-mail: wei.li@stud.tu-darmstadt.de

Address: Otto-Berndt-Straße 3, 64287 Darmstadt, Germany

Education

- **Ph.D. Candidate of Material Science (Oct. 2019 ~ Feb. 2023)**, Department of Materials and Earth Sciences, Technische Universität Darmstadt, Germany.
 - **Master of Material Engineering (Sep. 2016 ~ Jun. 2019)**, School of Material Science and Engineering, Zhengzhou University, China
 - **Bachelor of Material Science and Engineering (Sep. 2012 ~ Jun. 2016)**, School of Material Science and Engineering, Henan University of Technology, China
 - **Bachelor of Business Administration (Double Degree, Sep. 2013 ~ Jun. 2016)**, School of Management, Henan University of Technology, China
-

Research Experience

- **10/2019~ present, Supervisor:** Prof. Dr. Ralf Riedel
 - ✧ **Program:** Single-source-precursor derived additive-free bulk SiHf(B)N ceramics with excellent mechanical properties and oxidation resistance
 - **09/2016 ~ 06/2019, Supervisor:** Prof. Dr. Bingbing Fan
 - ✧ **Program:** Preparation and application of lightly porous gradient structure and highly wave-transparent materials
 - **11/2012 ~ 06/2016, Supervisor:** Prof. Dr. Xinpo Lu
-
-

Conferences

- **Li W**, Zhang F, Li N, et al. Effect of atmosphere on the fabrication of Si₂N₂O matrix composites. *The 20th National High-tech Ceramics Academic Annual Conference (2018), Inner Mongolia, China. (Oral presentation)*
-

Honors and Awards

- Chinese Scholarship for 4-Years study in Germany 2019-2023
 - The First Prize of the 3rd Innovation and Entrepreneurship Competition of Zhengzhou University 2018
 - The 1st Scholarship of Henan Province March 2017 and March 2018
 - Excellent Student Cadre of Henan Province May 2017
 - Outstanding Graduates of Henan Province May 2016
 - National Scholarship for Encouragement September 2014 and September 2015
 - National Scholarship September 2013
-

Research Skills

- Chemical synthesis and characterization: Schlenk technique for oxygen and moisture sensitive materials, TG/MS analysis, FI-TR analysis, NMR analysis, etc.
- Microstructure characterization: XRD, Raman, SEM, TEM, N₂ adsorption BET and Elemental Analysis, etc.

Publications and patents (2016 ~ 2022)

1. **Li, W.**; Li, F.; Yu, Z.; Wen, Q.; Fan, B.; Feng, Y.; Zhao, C.; Ricohermoso, E., III; Widenmeyer, M.; Weidenkaff, A.; Riedel, R., Polymer-derived SiHfN ceramics: From amorphous bulk ceramics with excellent mechanical properties to high temperature resistant ceramic nanocomposites. *Journal of the European Ceramic Society* **2022**, *42* (11), 4493-4502.
2. **Li W**, Yu Z, Wiehl L, et al. Hard and Tough Novel High-Pressure γ -Si₃N₄/Hf₃N₄ Ceramic Nanocomposites [J]. *Journal of Advanced Ceramics*, Available online: 08 May 2023.
3. **Li W**, Du H, Tian C, et al. Single-source-precursor derived bulk Si₃N₄/HfB_xN_{1-x} ceramic nanocomposites with excellent oxidation resistance [J]. *Zeitschrift für anorganische und allgemeine Chemie.*, 2022.
4. Zhan Y, **Li W**, Jiang T, et al. Boron-modified perhydropolysilazane towards facile synthesis of amorphous SiBN ceramic with excellent thermal stability [J]. *Journal of Advanced Ceramics*, 2022: 11(7): 1104-1116.
5. **Li, W.**; Yu, Z.; Wen, Q.; Feng, Y.; Fan, B.; Zhang, R.; Riedel, R., Ceramic-based electromagnetic wave absorbing materials and concepts towards lightweight, flexibility and thermal resistance. *International Materials Reviews* **2022**, 1-34.
6. Zhan, Y.; **Li, W.**; Grottenmüller, R.; Minnert, C.; Krasemann, T.; Wen, Q.; Riedel, R., Rapid curing of polysilazane coatings at room temperature via chloride-catalyzed hydrolysis/condensation reactions. *Progress in Organic Coatings* **2022**, *167*, 106872-106879.
7. Liu, J.; Ricohermoso III, E.; **Li, W.**; Liu, X.; Qiao, Z.; Ionescu, E.; Riedel, R., Phase composition, microstructure, and mechanical properties of polymer-derived SiOC glass-ceramics reinforced by WC particles. *Journal of the European Ceramic Society* **2022**, *42* (5), 1955-1962.
8. Zhan, Y.; Grottenmüller, R.; **Li, W.**; Javaid, F.; Riedel, R., Evaluation of mechanical properties and hydrophobicity of room-temperature, moisture-curable polysilazane coatings. *Journal of Applied Polymer Science* **2021**, *138* (21), 50469-50479.
9. Fan, B.; **Li, W.**; Zhang, F.; Li, H.; Zhang, R.; Liu, G.; Qian, F.; Chen, Y., Fabrication and properties of Si₂N₂O ceramics for microwave sintering furnace. *Processing and Application of Ceramics* **2020**, *14* (1), 32-39.
10. **Li, W.**; Zhang, F.; Li, N.; Su, T.; Fan, B.; Li, H.; Ye, G.; Zhang, R., Effect of atmosphere on the fabrication of Si₂N₂O matrix composites. *Processing and Application of Ceramics* **2018**, *12* (1), 66-71.

-
11. Chen, Y. Q.; Li, S.; **Li, W.**; Su, T. T.; Fan, B. B.; Li, H. X.; Zhang, R., Effect of SiCp Addition on Microstructure and Mechanical Properties of ZTA Ceramics by Microwave Sintering. *Solid State Phenomena* **2018**, *281*, 217-223.
 12. Fan, B.; **Li, W.**; Dai, B.; Guan, K.; Zhang, R.; Li, H., Preparation of mullite whiskers reinforced SiC/Al₂O₃ composites by microwave sintering. *Processing and Application of Ceramics* **2016**, *10* (4), 243-248.
 13. Patents: Bingbing Fan, Hongxia Li, Wei Li, Huayang Feng, et al. China Patent, CN 106747574 A.

Statement of Personal Contribution

The personal contribution of the author himself to the following research articles is listed.

[1] **Li W**, Li F, Yu Z, et al. Polymer-derived SiHfN ceramics: from amorphous bulk ceramics with excellent mechanical properties to high temperature resistant ceramic nanocomposites [J]. *Journal of the European Ceramic Society*, 2022, 42(11): 4493-4502.

The idea of this publication originated in the discussion of Wei Li, Prof. Ralf Riedel and Prof. Zhaoju Yu. The experimental program was designed by Wei Li under the supervision of Prof. Ralf Riedel and Prof. Zhaoju Yu. The preparation and most of the characterization of the samples were done by Wei Li. TEM measurement was performed by Fen Li. TGA/DTA test was performed by Dr. Marc Widenmeyer. Rietveld refinement was performed under the guidance of Dr. Changhao Zhao, Dr. Yao Feng and Prof. Qingbo Wen. Vickers hardness was measured by Prof. Bingbing Fan. All data were analyzed and visualized as Figures or Tables by Wei Li. The manuscript was completed by Wei Li. The rest of the authors revised and approved the manuscript before publication.

[2] **Li W**, Yu Z, Wiehl L, et al. Hard and Tough Novel High-Pressure γ -Si₃N₄/Hf₃N₄ Ceramic Nanocomposites [J]. *Journal of Advanced Ceramics*, Available online: 08 May 2023.

The idea behind this work originated in the discussion of Wei Li, Prof. Ralf Riedel, Prof. Zhaoju Yu, Dr. Shrikant Bhat and Dr. Leonore Wiehl. The methodology was designed by Wei Li under the supervision of Prof. Ralf Riedel, Prof. Zhaoju Yu, Dr. Shrikant Bhat and Dr. Leonore Wiehl. The synthesis of the precursor was performed by Wei Li, and the high pressure high temperature experiments were performed by Dr. Shrikant Bhat with the assistance of Wei Li, Dr. Leonore Wiehl and Christian Lathe. The synchrotron PXRD measurements were performed by Dr. Martin Etter and Dr. Shrikant Bhat. TEM was measured by Tianshu Jiang. Nanoindentation was performed by Dr. Sebastian Bruns. Thermal analysis was performed by Dr. Marc Widenmeyer. SEM and EDX was performed by Dr. Emmanuel III Ricohermoso. Vickers hardness was measured by Dr. Ying Zhan and Dharma Teppala Teja. Rietveld refinement and related analyzes were performed by Dr. Leonore Wiehl, and the rest of the data were

analyzed and visualized as Figures or Tables by Wei Li. The manuscript was written by Wei Li. Dr. Emanuel Ionescu, Dr. Martin Etter, Dr. Christian Lathe, Dr. Robert Farla, Prof. Qingbo Wen, Prof. Leopoldo Molina-Luna and Prof. Anke Weidenkaff revised and approved the manuscript before publication.

[3] **Li W**, Du H, Tian C, et al. Single-source-precursor derived bulk $\text{Si}_3\text{N}_4/\text{HfB}_x\text{N}_{1-x}$ ceramic nanocomposites with excellent oxidation resistance [J]. *Zeitschrift für anorganische und allgemeine Chemie.*, 2022.

The idea behind this publication originated in the discussion of Wei Li, Prof. Ralf Riedel and Prof. Zhaoju Yu. The methodology was designed by Wei Li under the supervision of Prof. Ralf Riedel and Prof. Zhaoju Yu. The preparation and most of the characterization of the samples were done by Wei Li. TEM measurements was performed by Hanzi Du and Tianshu Jiang. TGA/DTA was measured by Dr. Marc Widenmeyer. Rietveld refinement was performed under the guidance of Dr. Leonore Wiehl. XPS measurement was performed by Chuanmu Tian. All data were analyzed and visualized as Figures or Tables by Wei Li. The manuscript was completed by Wei Li. The rest of the authors revised and approved the manuscript before publication.

[4] Zhan Y, **Li W**, Jiang T, et al. Boron-modified perhydropolysilazane towards facile synthesis of amorphous SiBN ceramic with excellent thermal stability [J]. *Journal of Advanced Ceramics*, 2022: 11(7): 1104-1116.

The idea behind this publication originated in the discussion of Wei Li and Ying Zhan, under the supervision of Prof. Zhaoju Yu, Dr. Ralf Grottenmüller, and Prof. Ralf Riedel. The methodology was designed by Wei Li and Ying Zhan. The synthesis of the precursors and FTIR were done by Ying Zhan. The pyrolysis, XRD, SEM, and EDX of the investigated samples were performed by Wei Li. TEM was performed by Tianshu Jiang. TGA was carried out by Claudia Fasel. Molecular dynamic simulation was performed by Dr. Zhenghao Wu. All data were analyzed by Ying Zhan and Wei Li. The manuscript was written by Wei Li, Ying Zhan, and Dr. Zhenghao Wu. The rest of the authors revised and approved the manuscript before publication.

Signatures of Co-Authors

Ralf Riedel		Zhaoju Yu	
Ying Zhan		Shrikant Bhat	
Marc Widenmeyer		Anke Weidenkaff	
Qingbo Wen		Leonore Wiehl	
Bingbing Fan		Emanuel Ionescu	
Tianshu Jiang		Leopoldo Molina-Luna	
Changhao Zhao		Jan Philipp Hofmann	
Emmanuel Ricohermoso		Yao Feng	
Sebastian Bruns		Christian Lathe	
Robert Farla		Chuanmu Tian	
Jan Bernauer		Martin Etter	
Claudia Fasel		Florian Müller-Plathe	
Fen Li		Dharma Teppala Teja	
Zhenghao Wu		Ralf Grottenmüller	
Hanzi Du			